PHYSISORPTION PROCESSES ON GRAPHENE RELATED SURFACES WITH APPLICATIONS TO SOLID STATE HYDROGEN STORAGE

A THESIS SUBMITTED TO THE GRADUATE DIVISION OF THE UNIVERSITY OF HAWAII AT MANOA IN PARTIAL FULFILLMENT OF THE REQUIREMENTS FOR MASTER OF SCIENCE IN CHEMISTRY

by

Christian Squire

THESIS COMMITTEE:

JOHN D HEAD, CHAIRPERSON

THOMAS APPLE

KLAUS SATTLER

August, 2017

Acknowledgments

Above all I would like to thank my advisor, Dr. John D Head for his patience and support during the course of my graduate studies and wish him the best in retirement.

I would like to thank Dr. Thomas Apple and Dr. Klaus Sattler for their patience and support participating on my thesis committee. All previous graduate students that have been in the Head Lab during my time as a graduate student; Keegan Gotto, Jennifer Nagamine, Christopher Tanabe, thank you for helping with minute details and providing countless hours of moral support in the lab. I would like to thank our former undergraduates in our lab, Bryce Enright and Hiromi Kobayashi, for their enthusiasm and starting structures, the University of Hawaii at Manoa Chemistry Department for providing support and the opportunities for Teaching Assistantships, and a huge thanks to the UH ITS high performance computing center for providing countless hours of computer time that made this research possible.

Finally, I would like to thank my friends and family.

Abstract

This thesis investigates physisorption interactions of molecular hydrogen on graphene surfaces. The structure of graphene is outlined, followed by an overview of hydrogen storage materials. Focusing on hydrogen storage in a lightweight solid state material, molecular hydrogen is first adsorbed onto a pure graphene surface and the binding energy of the physically adsorbed molecule is calculated using two different computational methods. In a primary cluster approach, polycyclic aromatic hydrocarbons (PAHs) are used as approximations to graphene. In the SLAB approach, periodic boundary conditions are used to represent an infinite graphene sheet in repeating units.

A series of small molecules, including H_2, are adsorbed on graphene and their corresponding physisorption energies are calculated. The results of the two methods are compared to develop a reliable yet efficient computational approach to lightweight physisorption systems. Then, lightweight alkali metals, halogens, and corresponding alkali halides are adsorbed onto graphene and their physisorption energies are calculated. Molecular hydrogen is then adsorbed to these structures and its physisorbed energy is reevaluated.

LiF is shown to increase the magnitude of the H_2 PSE to -15.3 kJ/mol as a result of 2 adsorbed H_2 molecules, NaF is shown to increase the magnitude of the H_2 PSE to -17.8 kJ/mol as a result of 3 adsorbed H_2 molecules, LiCl is shown to increase the magnitude of the H_2 PSE to -11.7 kJ/mol as a result of 4 adsorbed H_2 molecules, and NaCl is shown to increase the magnitude of the H_2 PSE to -10.3 kJ/mol as a result of 6 adsorbed H_2 molecules. To our knowledge, this series of calculations has not been performed. These results provide potential novel coadsorbants that will increase the binding energy of the intact hydrogen molecule. The results can be used to propose a novel lightweight solid-state hydrogen storage system.

Contents

List of Tables

List of Figures

Chapter 1

Introduction

1.1 Graphene Background

1.1.1 From Graphite to Graphene

It is no surprise that all known life is comprised primarily of carbon given its tetravalent electron configuration and relatively low atomic weight. This gives rise to an innumerable number of possible molecular structures in carbon based systems. The lowest energy configuration of elemental carbon, graphite, has a defined enthalpy of formation of zero; the enthalpy of formation of diamond being 2.4 kJ/mol greater than that of bulk graphite at 298 K and 1 atm. The reason for this can be explained through their structures. In bulk diamond, each carbon atom is making four covalent bonds in a tetrahedral arrangement in a cubic Bravais lattice belonging to the Fd3m space group. The lattice structure consists of two over-lapping face centered cubic lattices, with each sp^3 carbon atom making four covalent bonds. Despite an average C-C bond length of 1.54 Å , diamond structure shows maximum packing fraction and is an insulating compound with a band gap of around 5.5 eV.

Bulk graphite is made of sheets of graphene, the two-dimensional allotrope of carbon, in a honeycomb lattice with with an average bond length of 1.42 Å . The three C-C bonds are about 25% stronger than the four in diamond [34]. In bulk graphite, the two dimensional sheets are separated an average distance of 3.35 Å , stacked in an alternating ABAB pattern and held together by van der Waals forces. Due to the large theoretical surface area of 2630 m^2/g [10], weaker dispersion interactions sum to a strong interaction. Bulk graphite is classified as a semi metallic, layered van der Waals structure with a hexagonal lattice structure belonging to the P63/mmc space group. The band structure of graphite shows overlapping parabolic valence and conduction bands. The hexagonal lattice structure of the graphene layers comes from the two dimensional P6/mm space group. graphene is essentially an extended sheet of connected benzene rings removed of the terminal hydrogens. The electrons in the sp hybridized orbitals form covalent bonds with one another forming the two-dimensional sheet. The p_z orbitals protrude orthogonal to this two dimensional backbone with the resulting conjugated π-electron system extending until to the edge of the graphene sheet. The edge of the sheet could be described by a physical boundary, defect, or chemical substitution that disrupts the conjugated π-network. The low energy excitations of such a large network of conjugated π-electrons results in chiral, massless Dirac fermions [16].

Electronic energy levels in molecules, extrapolated to bulk systems form bands. Equivalent to the HOMO-LUMO gap in molecules is the band gap in bulk materials. Typically, a material is an insulator if the valence band is filled and there is a large gap in energy to the conduction band, as in the diamond structure. A material is classified as metal if the valence band is 10-90% filled, a semimetal if the valence and conduction bands are overlapping and partially filled, and semiconductors when are bands are less than 10% or greater than 90% filled. The conduction band in graphene is formed from the carbon π orbitals. Each carbon contributes one electron, resulting in the π-band being half filled and a half empty π*-band. The energy required to excite electrons in this system is minimal and particles in the delocalized system approach speeds up to 1/300 the speed of light, at which point they behave as massless Dirac fermions. The π*-band in graphene has a linear dispersion relation as it approaches the Dirac point where it meets the half full π-band forming a cone shape about each K-point in the Brillouin zone. This interesting looking

band structure explains graphene's behavior as a zero-band gap semiconductor [30].

Characteristic of Dirac fermions is the anomalous integer quantum hall effect. The Hall effect, which is used to measure the electron density of a sample, in graphene occurs in half integers and can be observed at room temperature due to the large cyclotron energies of the relativistic fermions [16]. The resulting fermion mobility of 120,000 cm^2/Vs is the highest of any known semiconductor [3]. There are many ways to induce a band gap in graphene, giving rise to its theoretical tunable band gap. This can be done as simply as stressing or producing structural defects in the sheet, or from dopants where carbon is replaced by substituted heteroatoms or by heteroatoms adsorbed to the graphene surface. These somewhat unusual electronic properties are obsevered in bulk graphene suggest a promising material for a wide range of industrial applications.

1.2 Hydrogen Storage Background

Graphene's surface area and tunable band gap, have made it a popular topic since it was first experimentally isolated, making previous theoretical publications more applicable to real world issues. The present investigation looks at the fundemental interaction of molecular hydrogen and graphene based systems. It is of interest to increase the energy associated with this interaction to improve storage mechanisms in a solid state hydrogen storage device. In this section, it is first outlined the current state of hydrogen storage materials.

Current dependence on fossil fuels has lead the search for a cleaner, efficient fuel source evermore critical with time. A promising and popular candidate is hydrogen, with an energy density of 143 MJ/kg, three times gasoline [25]. The concept of a fuel cell is not a new one, in fact it was first developed by Sir William Robert Grove in 1839. It was not until the $1960's$ that hydrogen fuel cells were first commercially used and have been used in aerospace applications. Hydrogen fuel cells have also been more recently used in commercial buses and vehicles. Molecular hydrogen is the first, simplest, and most abundant molecule in the universe and its use in fuel cells produces only water and minimal heat compared to

an internal combustion engine. The reason many of these commercial uses are not more widespread is because there are many competing energy sources.

1.2.1 Hydrogen Storage Materials

Despite hydrogen having the highest energy by mass of any other fuel, it also has a very low energy density by volume at 0.0108 MJ/L (3000 times less than gasoline, it's a diffuse gas) making storage and delivery difficult and potentially dangerous [25]. Hydrogen is not an energy source, but an energy carrier. It must be produced with as much energy that will be released. This is similar to electricity, except once the hydrogen is contained, the chemical energy can be transported and stored indefinitely[41]. The difficulty is diverted into developing an efficient reversible storage mechanism for hydrogen gas. In pursuit of an efficient hydrogen storage system, the US Department of Energy (DOE) has set ultimate target values for volumetric capacity of 70 g/L and gravimetric energy capacity of 7.5 wt% (see Figure 1). Also considered is refueling times, costs, cycle life, and of reusable hydrogen [41].

The simplest method of hydrogen storage is mechanically, that is in an unbound, unaltered form. This can be achieved in compression, liquefied through cryogenic cooling, or both in a cryogenic compression. Many fuel cell vehicles have been produced by various major motor companies all of which still use mechanical means of onboard H_2 storage and many have short lived lives as most have been discontinued. The current fuel cell vehicles in production all still rely on a mechanical storage mechanism. For H_2 gas in a compressed tank, the energetics depends on the compression of the gas. For tanks of 345 and 690 atm, typical gravimetric and volumetric energies are 5.5-5.2 wt% and 17.6-27.2 g/L respectively. Neither of these systems was expected to meet the DOE target values. In terms of overall efficiencies (56.5-54.2% respectively) these are within the DOE target of 60% [25]. The largest barrier for production of the compressed H_2 gas system is cost, largely due to the tanks required for storing the gas. These tanks must be able to withstand high pressures, be strong enough to not easily rupture, be lightweight, and have a sufficient thermal conductivity. A simple way to increase volumetric capacity would be to liquefy it. This cryogenic storage is an energy

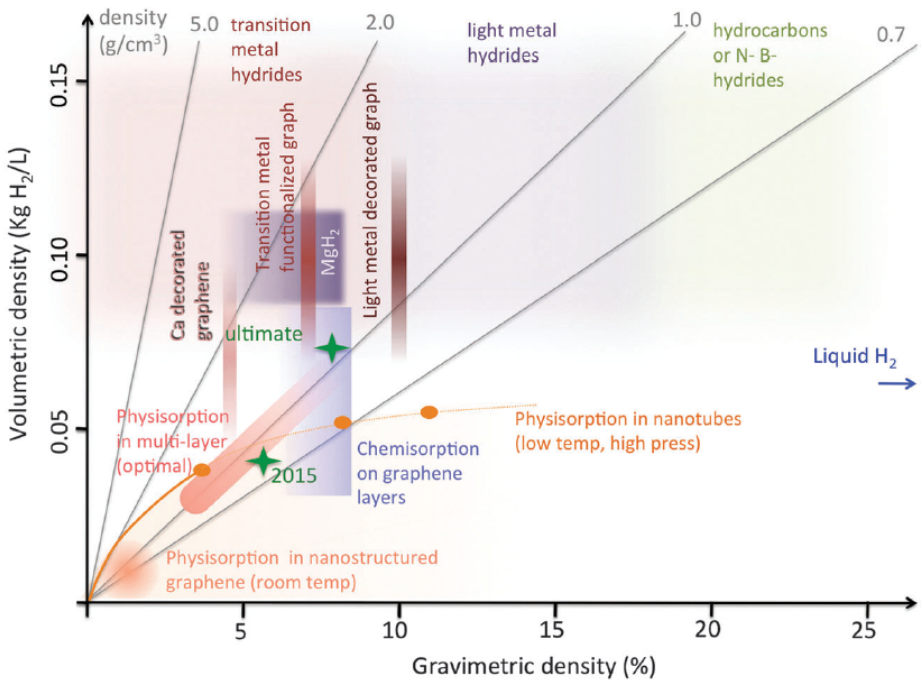

Figure 1.1: Overview of hydrogen Storage Systems [21]
This figure shows the gravimetric capacity wt% vs volumetric capacity (kg/L) for a variety of materials that are considered for hydrogen storage systems. Included on the plot is the Department of Energy's targets for a solid state hydrogen storage system for onboard fuel cell applications.
Source : *Tozzini and Pellegrini Phys. Chem. Chem. Phys.*(2013), 15, 80

intensive process as the H_2 must be cooled to 20 K. This also requires a strong vacuum insulated tank, further increasing the size and weight of the system. An alternative method of mechanically storing H_2 gas is through capillary storage. This method involves filling many smaller vessels that act as individual high-pressure H_2 carriers. The capillaries are filled at a plant and then ultimately stored in larger, lightweight tanks. The gravimetric capacity, weight, and efficiency of this method exceeds DOE standards. However, the volumetric capacity is insufficient, a large amount of energy is required to release H_2 from the capillaries, and they have limited life spans [25].

Mechanically stored H_2 has been used to build functioning fuels cells, but for the concept to be used as a mass produced alternative energy source, a more efficient, safe and reusable storage and delivery process for H_2 gas has been extensively researched. If all of this sounds tiring then it is apparent that a better means of H_2 storage is necessary for the future of

the fuel cell vehicle. The remaining methods of storing H_2 discussed here are categorized into two groups: chemical storage and storage in adsorbent materials, and will be discussed in the proceeding sections.

1.2.2 Chemisorption Based Methods

If storing H_2 gas in an unaltered form is insufficient to meet DOE standards, a logical solution may be to chemically store H_2. Storage in a chemically bound state allows for lower pressures to achieve higher gravimetric and volumetric capacities. In order for H_2 to bind to a substrate, the molecule first dissociates and then each atom forms a covalent bond with the storage material. This process is often exothermic and is referred to as chemisorption [31]. This results in H-substrate bonding energies of about 2-3 eV (200 - 300 kJ/mol). This suggests that storing H_2 in the form of chemical hydrides could potentially reach DOE targets, the downside of this binding energy is then the delivery of H_2 to the fuel cell which often requires high temperatures and catalysis [19]. This means of chemically storing H_2 has been known since Thomas Graham observed hydrogen absorption onto Palladium in 1866 [25] and is still been widely investigated [31].

The most common substrate for H_2 chemisorption is in chemical hydrides. This class includes both metal and non-metal hydrides. Metal hydrides comprise a large class of molecules including simple binary (AlH_3) and two-metal hydrides intermetallic hydrides ($NaAlH_4$), and complex metal hydrides such as amides, imides, and borohydrides[2, 28, 41]. The biggest downside of storing hydrogen in the form of chemical hydrides is that they are not rechargeable on board a fuel cell vehicle[25]. These systems can however hold large quantities of hydrogen due to a large surface area, made accessible in a solid state device. Coupled with a high chemisorption energy, many of these compounds (AlH_3, Li_2NH, $LiBH_4$, NH_3BH_3, N_2H_4) reach DOE targets (see figure 1). The requirement of high temperatures in these systems have lead these catalysts to be extensively studied recently to release H_2 at lower temperatures.

The spillover mechanism involves diffusion of the reactive species from the catalyst, often transition metals such as Platinum, to it's support [19]. Certain intermetallic hydrides such as $NaAlH_4$ can adsorb and desorb under mild conditions. These compounds still have low maximum gravimetric capacities, slow kinetic properties, and a low volumetric capacity due to their large concentrations of metals [25, 41]. The gravimetric capacity for $NaAlH_4$ is just below the 2010 DOE target at 5.5 wt% hydrogen. Of the chemical hydrides however, $LiNi_4H_5$ is currently commercially available as it has ambient operating conditions [25]. The problem with the latter being it's lower gravimetric capacity.

Current research has shifted towards lighter metals for use in solid state storage devices. hydrogen storage in chemical hydrides could be useful in single use applications where on board refueling is not necessary, however part of the DOE targets includes refueling times. Through a weaker interaction with the substrate where H_2 does not dissociate but remains chemically unchanged, reversible H_2 storage and delivery becomes more efficient. The next section will discuss such systems.

1.2.3 Physisorption Processes

Where the chemisorbed energy of an atom ranges from 200-300 kJ/mol as described above, the physisorption (physical adsorption), binding energy is 10-20 kJ/mol [28]. This much weaker interaction leaves the H_2 in molecular form, around 3 Å or greater above the substrate. This much weaker interaction has the advantage of improved desorption kinetics. The main advantage of a physisorbed system over mechanically stored hydrogen, is that the maximum volumetric density of H_2 is not in its liquid state, but can be further compressed in solid state systems [41]. The primary limitation to using a physisorbed H_2 storage mechanism is the low H_2 gravimetric densities due to their low binding energy. Therefore, for adsorption materials to be effective in storing H_2, they must have very large surface areas. The sum of these weakly interacting energies will then contribute to a higher gravimetric capacity in a bulk material. Therefore, adsorbent materials with high theoretical surface areas are investigated as potential solid state hydrogen storage materials. Adsorption materials for H_2 storage include metal organic frameworks, nanostructured materials, and clathrates.

Metal organic frameworks (MOFs) are crystalline solids composed of metal ions or clusters connected through molecular bridges [25]. MOFs are highly porous as they have nanometer cavities between the metal atoms and their molecular bridges and typically have surface areas greater than 3000 m^2/kg. Despite this large surface area, many MOFs have relatively low gravimetric energy densities. Optimizing these structures for H_2 storage involves fine tuning of the pore size to van der Waals radii of the hydrogen atoms in molecular H_2. This can be done by adsorbing additional light elements in the pore, hopefully of a nonvolatile adsorbate, with a low vapor pressure as to not desorb with the H_2. Ideally, a light first row metal would be added to optimize the pore size as well as increase H_2 affinity for the MOF complex. The other way to decrease pore size in MOFs is through catenation with an identical framework. This is done either by interpenetration, where the MOFs are maximally displaced from each other or through interweaving where there is minimal inter-MOF separation [25]. Although the general capacities of MOFs for reversible H_2 storage are generally too low for practical applications, this large class of compounds still provides insight to the design of an efficient physisorbed H_2 system. Many of these complex structures involve many different metal ligands, which limits their maximum gravimetric capacity. Less commonly used, clathrates, where the lattice of one compound can trap a second chemical compound, can be used to reversibly store H_2. In particular, methane hydrate has been shown to hold up to 33.4 wt% of H_2. Despite the need for methane in this process, this system is still not practical as high pressures are needed for synthesis and preparation of the storage material and operation temperatures are below the freezing point of water. Clathrate hydrates are still being studied as they have been shown to have capacities of 5.6 wt% H_2 at 59-118 atm and 263 K with low storage and release energies, which can be obtained from otherwise wasted heat [25].

Hydrogen storage on nanostructured materials is a relatively new field but can hold hydrogen in an intermediate bound state between chemisorption and physisorption [28]. The majority of nanostructured materials are carbon based as they are lightweight, have a high theoretical surface area, and can adsorb molecules to their surface. The first nanostructured cabon materials to be studied began in 1990 with activated carbons and carbon nanotubes, (CNT's). Activated carbons can hold around 3.2-8.0 wt% H_2 depending on the temperature and pressure. These materials increase storage capacities with decreasing temperature

and increasing pressure. These materials cannot hold as much H_2 as other nanostructured materials but have been extensively studied as their chemistry is well understood and they are relatively inexpensive and easy to synthesize. Due to the low operating temperatures, cryogenic storage is necessary, and refueling becomes expensive and these systems are not much more practical than cryogenically cooled H_2 gas.

Carbon nanotubes are porous and have a high surface area allowing for H_2 to adsorb to both the convex and concave surface of the CNTs. It is these reasons that allows CNTs to hold 0.25-11.0 wt% hydrogen depending on conditions. Metal dopants added to this system have been shown to increase this value to 10.8-20.2 wt% hydrogen [25]. This wide range in capacities is due the type and orientation of the CNT used, as well as temperature and pressure conditions. Larger nanotubes produce higher storage capacities, but orientation of the nanotubes can have a larger impact. CNTs still may be a good candidate for hydrogen storage and are research in this field is ongoing.

In 1991 it was discovered that H_2 could be encapsulated in buckminsterfullerene, C_{60} [25]. Experimentally the energy barrier for this to occur can be overcome by high pressure and laser excitation. It is difficult to put multiple H_2 molecules inside C_{60} as the enthalpies are positive for four or more H_2 molecules. These complexes are however local minima on the potential energy surface and are therefore metastable structures. As more H_2 molecules are added, the C-C bond lengths in the C_{60} increase. When less than 10 H_2 molecules are present, the H_2 take on distinct geometric clusters, tetrahedron for four, trigonal bipyramidal for five H_2 molecules, and so on. When 10 or more H_2 are encapsulated, H_3 molecules begin to form due to the high pressure and stabilized by the polarizability of the C_{60}. At a maximum C_{60} distortion of about a 9.3% increase in the C-C bond length before it ruptured, the system contained 29 H_2 molecules and had a gravimetric capacity of 7.5 wt% [25]. This is an interesting result, but many issues remain with using C_{60} for hydrogen storage as the chemistry is energy intensive and not well understood.

It has been shown that addition of metals to the adsorption substrate can increase H_2 binding energy and thus gravimetric storage capacity. Other than the choosing the correct metal adatom, this enhanced storage capacity also depends on the surface area of the

substrate and contact between the adsorbate. In metal decorated carbons, the adsorption process typically involves the dissociative chemisorption of H_2 onto the metal nanoparticles, followed by the migration of the H-atoms on the carbon substrate [25]. Therefore, a close metal substrate distance is desired to minimize the energy barriers of migrating H-atoms. The metals used as dopants in such systems is usually Pt or Pd but other transition metals such as Ru, Ni, Sc, V, Ti, and alkali metals have also been investigated [25, 41]. Of these systems, Ti decorated carbon nanostructures have shown 7-8 wt% H_2 via the spill-over mechanism. Of the most effective metal decorated carbon systems , a C_{60} with 8 incorporated Na atoms held 48 H_2 molecules with a corresponding gravimetric density of 9.5 wt% H_2 [25] and in Li doped graphene, four H_2 molecules adsorbed about the Li atom amounting to 10 wt% H_2 [41]. In both of these systems, the binding energies of H_2 were in between that of physisorption and chemisorption, as the H_2 molecules remain intact and surrounding the metal adatom. The high adsorption energies likely to high ion-molecule electrostatic interactions. This is different than the spillover mechanism that occurs when transition metals are used as the adatoms. Using alkali metals as opposed to transition metals in these systems has the advantage of increasing volumetric and gravimetric capacities due to their light weight but also, with the H_2 remaining intact, lead to lower desorption energies and could be potential candidates for a solid state H_2 storage system.

Nanostructured materials that are not primarily composed of carbon have also been considered, although their structures are analogues of carbon materials. For instance, boron fullerenes doped with calcium have shown capacities of 8.2 wt% H_2 at ambient conditions [25]. Other nanostructures of alternating nitrogen and boron atoms have shown less promising results that are less than that of their carbon analogues. For this reason, we will continue focusing on carbon based adsorbent materials.

1.2.4 Review of Previous Work

The interaction between hydrogen and graphitic surfaces is a fundamental reaction with widespread applications from the recombination of H_2 in the interstellar medium [42, 4] to the reversible storage of hydrogen for delivery to fuel cells [44, 5, 19]. This theoretical investigation was initiated to find an appropriate computational method to describe the interaction of H_2 atop graphene surfaces. As an H_2 molecule approaches a graphene sheet, at 3 Å, the H_2 can be physically adsorbed to the sheet with binding energy of around 5 kJ/mol [9, 42]. This metastable physisorbed state was first described by Jeloaica et al 1999 [31] and is primarily a London dispersion interaction where a weak dipole moment is induced in the H_2 molecule and results in the overlapping of H_2 σ orbitals with the π states in graphene forming bonding and antibonding orbitals [44]. Calculation of the H_2 graphene physisorption energies can produce a range of binding energies depending on the computational method used [9]. This is due to the relatively weakly interaction energy between an individual H_2 and relatively large size of the carbon framework needed to sufficiently represent a graphene sheet. In these systems, it is well known that van der Waals dispersion corrections (see Section 1.3.6) are often required to get theoretical results to match experimental data [27, 33].

Under conditions where H_2 is less than 3 Å from graphene, the electron density is further distorted from the induced dipole moment, antibonding σ^* orbital gets filled and a large activation barrier is produced for adsorption [44]. If this is overcome, dissociative chemisorption occurs resulting in covalently bound H atoms directly atop the now sp^3 hybridized carbon atoms at a height of about 1.5 Å [31]. The rehybridization of the carbon substrate framework distorts the once planar sheet contributing to a large energy barrier for this reaction. During the process the bonding carbon atom relaxes up to 0.4 Å from its original position. As this occurs, each subsequent H adsorption becomes more favorable. At high enough temperatures and pressures, if this process were to continue, H_2 would reduce graphene to graphane[44].

The large activation energies and binding energies associated with chemisorption based processes result in spill over. It is known a single H atom can also be physisorbed to graphene

with similar binding energies and distances to H_2. In a combined experimental and theoretical study, Cheng et al investigated hydrogen storage on graphene based nanostructures providing a detailed spillover mechanism using Pt nanoclusters as catalysts. The results indicated that hydrogen storage in solid state carbon nanostructures via a chemisorbed state is energetically difficult. For the system to work it was concluded that hydrogen spillover in carbon based materials is only possible via a physisorbed state of the H atom [5]. There are many ways to easily alter the electronic structure of pure graphene, hence its popularity as a finely tunable semiconductor. It is difficult experimentally to synthesize pure graphene, and defects open a small band gap changing its physical properties as well. For instance, a carbon vacancy would leave a dangling bond and preferentially adsorb hydrogen to that location. One of the interesting properties of graphene being its ability to fix holes in its structure do to the large stability of the π-system. Chemically doping the graphene (usually with Boron or Nitrogen), or decorating it by adsorbing metals or other atoms to the surface has been shown to increase hydrogen binding. Curvature also plays a role in both the chemisorption and physisorption of atomic and molecular hydrogen. On convex graphene surfaces, such as fullerenes and nanotubes, it has been shown that the chemisorbed energy of the atomic hydrogen is enhanced by about 100-200 kJ/mol as a result of each adsorbed H_2 molecules[41]. The effect on physisorbed hydrogen is the opposite. Both atomic and molecular hydrogen preferably physisorb to concave graphene like surfaces as van der Waals interactions are stronger in concavities. This latter effect is much smaller and only observed at low temperatures. An interesting application of the former presents opportunities to have a hydrogen storage system that functions via corrugated graphene. On the convex surfaces, chemisorbed H atoms could be transported with minimal diffusion. This system has the advantage of chemisorptive storage of atomic hydrogen at fixed temperature and pressure, and can desorb by mechanical catalysis by inverting the concavity of the corrugated graphene [41]. Although this system would be able to efficiently and reversibly store hydrogen reaching estimated 8 wt% gravimetric density, it is difficult to do experimentally.

To increase H_2 physisorption energies on graphene, the decorative approach seems like a promising candidate for a practical solid state storage device as it can enhance the physisorption interaction of H_2. This method involves adsorbing an atom, usually a metal, to the

surface of the graphene, called an adatom. Similar to the activation energy for subsequent hydrogen adsorption, physisorption of H_2 after adatom addition can be more energetically favorable than before. The storage capacity of a metal decorated carbon material depends on the identity of the metal (Pt or Pd usually), the surface area of the carbon substrate, and the distance between the metal and the substrate. In contrast to the spillover mechanism which typically uses transition metals, alkali metals have been shown to increase H_2 physisorption on graphene. These systems are advantageous over transition metals simply because they are lighter, and consequently can have higher gravimetric and volumetric capacities. A recent ab initio calculation produced structures that contained 48 H_2 molecules were adsorbed about eight sodium adatoms atop a graphene surface. In these structures the H_2 molecules were oriented around the metal ions, suggesting the storage capacities of up to 9.5 wt% H_2 are due to ion-molecular electrostatic interactions [25]. More recently, Ma et al looked at the effect of Pd decorated graphene with vacancies and boron dopants and resulting in binding energies of 19-87 kJ/mol that could hold up to three H_2 molecules per Pd atom [12]. A similar ab initio calculations by Kim et al showed Li decorated, defected graphene could hold up to four H_2 molecules with binding energies of 19-34 kJ/mol [11]. Pantha et al also studied Na decorated graphene and adsorbed five H_2 molecules around each Na atom and increase the binding energy from 6.6 kJ/mol on pure graphene to 18.5 kJ/mol corresponding to a gravimetric capacity of 4.02 wt% [36] . Although this number remains significantly less than the ultimate DOE goal of 7.5 wt%, these systems are still of interest due to their lightweight, simplicity, and low desorption energy barriers. The main issue with alkali metal decorated carbons is that these predicted structures are experimentally difficult to reproduce [25]. Also to consider is the mild desorption energies associated with the Na graphene system could still reach DOE targets if the system is able to be produced experimentally and tested. The "holy grail" adsorption enthalpy change is only 15.1 kJ/mol for storage and delivery of H_2 at 1.5-30.0 bar pressure and room temperature [20].

Focusing on physisorbed based storage mechanisms, it is important to have reliable experimental results to compare to calculated values before investigating potential candidates for novel systems. Given the extensive amount of calculations that have been done using polycyclic aromatic hydrocarbons (PAHs) as approximations to graphene to calculate

H_2 binding energies, there is good agreement on these results. Recently, in an ab inito density functional theory (DFT) investigation which included Grimme's empirical dispersion term, Ganji et al produced results in good agreement with current experimental results. These B3LYP-D3/TZVPP calculations produced an optimized H_2-$C_{24}H_{12}$ (coronene) structure with a physisorbed H_2 with a bond length of 0.743 Å at a height of 3.289 Å above the coronene substrate with a binding energy of -5.0 kJ/mol [13]. In 2003, Heine et al produced a variety of H_2-PAH structures using second order Møller-Plesset perturbation theory (MP2). The resulting binding energies range from -3.5 to -7.2 kJ/mol [9]. These two references provide the expected range for physically measurable physisorbed H_2 binding energies.

1.3 Computational Methods

The underlying physical laws necessary for the mathematical theory of a large part of physics and the whole of chemistry are thus completely known, and the difficulty is only that the exact application of these laws leads to equations much too complicated to be soluble.
-Paul Adrian Maurice Dirac, 1929 [26]

Although this statement was certainly true in 1929, with highly developed methods thanks to great computational chemists as Walter Kohn and Sir John Anthony Pople who in 1998 won the Nobel Prize in Chemistry for developements in computational chemistry[38], along with the modern computing power, accurate approximations to these equations can now be obtained in a reasonable amount of time. To begin a discussion of computational chemistry, one always starts with the Schrödinger equation

$$\hat{H}\Psi = E\Psi \tag{1.1}$$

Where E is the total energy and Ψ is the wavefunction of the system. Ψ is a function of the spatial and spin coordinates of the particles in the system. The time dependent Schrödinger equation is also a function of time and describes all possible information about the system[32]. Ψ itself has no physical interpretation but its magnitude $|\Psi|^2$ gives a

probability density, that is the probability of finding a particle in a particular region of space. This was first postulated by Max Born and it can be shown that

$$|\Psi(x,t)|^2 = |\Psi(x)|^2 \tag{1.2}$$

For most computational purposes, we wish to use the Schrödinger equation to calculate the total energy of the system. A full solution to Equation 1.1 is the eigenfunction Ψ and eigenvalue E, the total energy. From Equation 1.2, The probability density $|\Psi|^2$ does not change with time. To calculate the total energy of the system, the time independent Schrödinger equation is therefore usually sufficient. It is important to note that our stationary state wavefunction describes a probability density that does not change with time, but the particles themselves are not stationary [32].

The Hamiltonian operator, $\hat{H}$ is the sum of a kinetic energy operator $\hat{T}$ and a potential energy operator $\hat{V}$

$$\hat{H} = \hat{T} + \hat{V} \tag{1.3}$$

In the classical Hamiltonian, the total energy H, can be expressed as a function of the cartesian spatial coordinates and their conjugate momenta p=mv. T is the kinetic energy $\frac{p^2}{2m}$ and the potential energy V is a function of the spatial coordinates only.

The corresponding quantum mechanical operator to the classical hamiltonian is given by the time-independent Schrödinger equation where the molecular Hamiltonian is given by

$$\hat{H} = -\sum_{\alpha} \frac{\hbar^2}{2m_\alpha}\nabla_\alpha^2 - \frac{\hbar^2}{2m_e}\sum_i \nabla_i^2 + \sum_\alpha \sum_{\beta>\alpha} \frac{Z_\alpha Z_\beta e'^2}{r_{\alpha\beta}} - \sum_\alpha \sum_i \frac{Z_\alpha e'^2}{r_{i\alpha}} + \sum_j \sum_{i>j} \frac{e'^2}{r_{ij}} \tag{1.4}$$

where Z_α is the atomic number for the α nucleus, e' is the elementary charge in statcoulombs (e'=$\frac{e}{4\varepsilon_0}$), α, β refer to nuclei and i, j refer to electrons. The first two terms in Equation 1.4 are the kinetic energy for the nuclei and electrons respectively. The third term represents the potential energy of the repulsions between nuclei α and β The fourth term is the attractions of electrons i with nuclei β. The last term is the potential energy due to the repulsions between electrons i and j. While writing $\hat{H}$ is easy to do, finding an exact solution for all but the most trivial of systems is impossible. We can however make a series

of assumptions and approximations that make solving the molecular Hamiltonian for the groundstate wavefunction and corresponding energy to a sufficient accuracy for molecular systems of interest. The first approximation takes into account the fact that the nuclear mass m_α is much greater than the electron mass m_e and considers the nuclei as fixed when the electrons carry out their motions [24]. Under this Born-Oppenheimer approximation, the electrons are viewed as moving in a sea of fixed nuclei and the first term in Equation 1.4 can be left out. The resulting solution under this approximation is the electronic wavefunction $\phi_{elec}(r_i; R_A)$. This depends explicitly on the electronic coordinates, r_i, and parametrically on the nuclear coordinates, R_A. That is in different arrangements of the nuclei, ϕ_{elec} is a different function of electronic coordinates. This can be thought of as the electrons instantly adapting to different nuclear arrangements.

It is convenient at this point to introduce atomic units. Atomic units are designed to simplify the equations by setting several of the small value constants equal to one. In atomic units m_e=e=$\hbar$=a_0=$4\pi\varepsilon_0$=1 Hartree [10]. The unit for energy is Hatrees, E_h, where

$$1E_h = \frac{m_e e^4}{(4\pi\epsilon_0\hbar)^2} = 2625.5\frac{kJ}{mol} = 27.211eV \tag{1.5}$$

The molecular Hamiltonian can then be written under the Born-Oppenheimer approximation in atomic units

$$\hat{H} = -\frac{1}{2}\sum_i \nabla_i^2 + \sum_\alpha \sum_{\beta>\alpha} \frac{Z_\alpha Z_\beta}{r_{\alpha\beta}} - \sum_\alpha \sum_i \frac{Z_\alpha}{r_{i\alpha}} + \sum_j \sum_{i>j} \frac{1}{r_{ij}} \tag{1.6}$$

If the second term is dropped, this is the purely electronic molecular Hamiltonian $\hat{H}_{elec}$ under the Born-Oppenheimer approximation. Solving the electronic problem involves replacing electronic coordinates by their average values then generating a nuclear Hamiltonian in a average field of electrons. Nuclei under the Born Oppenheimer approximation then move on a potential energy surface obtained by solving $\hat{H}_{elec}\phi_{elec} = \varepsilon_{elec}\phi_{elec}$. Where the electronic wavefunction ϕ_{elec} describes the motion of the electrons and $\varepsilon_{elec}(R_\alpha)$ and ϕ_{elec} both depend parametrically on the nuclear coordinates. Solutions to $\hat{H}_{nuc}\phi_{nuc} = \varepsilon_{nuc}\phi_{nuc}$ describe

translation, vibrations, and rotations of the molecule where

$$\hat{H}_{nuc} = -\frac{1}{2}\sum_{i}\nabla_i^2 + \varepsilon_{elec}(R_\alpha, R_\beta, ...) + \sum_{\alpha}\sum_{\beta>\alpha}\frac{Z_\alpha Z_\beta}{r_{\alpha\beta}} \tag{1.7}$$

This is the nulear Hamiltonian describing the motion of the nuclei in an average field of electrons[40].

1.3.1 Hartree Fock Theory

In 1928, two years after the Schrödinger equation was published, Douglas Hartree proposed a method for obtaining approximate solutions to many electron systems. In this independent electron approximation, Hartree assumed each electron moves in the average potential generated by the other electrons. The problem with the Hartree method is the wavefunction is represented as a product of single particle electronic wavefunctions. An issue already known in 1926 to both Werner Heisenberg and John Slater who both independently proposed that, "the wavefunction of electronic motions must be antisymmetric with respect to the exchange of electrons to satisfy the Pauli exclusion principle naturally and therefore should be represented as a determinant" [32]. In 1930 both John Slater and Vladimir Fock applied the Slater determinant to the Hartree method, giving rise to the Hartree Fock method which is fundamental to quantum chemistry.

Before we can calculate the energy of a molecule, the first thing to do is decide how to represent the wavefunction. A good starting point is to take a linear combination of atomic wavefunctions. To do this we choose to use a predefined set of one electron functions we will call basis functions. Primitive Gaussian type basis functions are often used that follow the form

$$g(\alpha, \vec{r}) = cx^n y^m z^l e^{-\alpha r^2} \tag{1.8}$$

where c is the normalization constant, α determines the radial extent of the function and n,l, and m are normalization parameters. The actual molecular basis functions ϕ_i are then taken as linear combinations of Equation 1.8 to form contracted gaussian functions that

can be expanded to form the spatial molecular orbitals

$$\phi_i = \sum_\mu C_{\mu i} \sum_\nu d_{\mu\nu} g_\nu = \sum_\mu C_{\mu i} \sum_\nu \Theta_\nu \tag{1.9}$$

where the $d_{\mu p}$'s are fixed constants selected for a given basis set and $c_{\mu i}$ are the orbital expansion coefficients [10]. The spatial orbitals ϕ_i are functions of the position vectors r and describe the spatial distribution of an electron such that $|\phi_i|^2$ is the probability density. To completely describe an electron, it is also necessary to specify its spin. To do this we introduce an orthonormal pair of functions $\alpha(\omega)$ and $\beta(\omega)$ corresponding to spins up and spin down electrons[40]. Multiplying our spatial orbitals by these spin functions produces spin orbitals. With a defined basis set we are now ready to construct the closed shell wavefunction in terms of spin orbitals. As mentioned above, this will be a single Slater determinant

$$\psi(\vec{r_i}) = \frac{1}{\sqrt{n!}} \begin{vmatrix} \phi_1(\vec{r_1})\alpha(\omega_1) & \phi_1(\vec{r_1})\beta(\omega_1) & \phi_2(\vec{r_1})\alpha(\omega_1) & \phi_2(\vec{r_1})\beta(\omega_1) & \cdots \\ \phi_1(\vec{r_2})\alpha(\omega_2) & \phi_1(\vec{r_2})\beta(\omega_2) & \phi_2(\vec{r_2})\alpha(\omega_2) & \phi_2(\vec{r_2})\beta(\omega_2) & \cdots \\ \phi_1(\vec{r_3})\alpha(\omega_3) & \phi_1(\vec{r_3})\beta(\omega_3) & \phi_2(\vec{r_3})\alpha(\omega_3) & \phi_2(\vec{r_3})\beta(\omega_3) & \cdots \\ \phi_1(\vec{r_4})\alpha(\omega_4) & \phi_1(\vec{r_4})\beta(\omega_4) & \phi_2(\vec{r_4})\alpha(\omega_4) & \phi_2(\vec{r_4})\beta(\omega_4) & \cdots \\ \vdots & \vdots & \vdots & \vdots & \ddots \end{vmatrix} \equiv |\Psi_0\rangle \tag{1.10}$$

where the spin functions $\alpha(\omega_m)$ and $\beta(\omega_m)$ are the spin functions for electron m. For n electrons, if there are n/2 spatial orbitals, then there are n spin orbitals (elements of the above matrix). We can rewrite these single electron spin orbitals

$$\left.\begin{aligned} \chi_{2i-1}(r,\omega) &= \phi_i(\vec{r_i})\alpha(\omega) \\ \chi_{2i}(r,\omega) &= \phi_i(\vec{r_i})\beta(\omega) \end{aligned}\right\} i = 1, 2, ..., K \tag{1.11}$$

where K is the number of spatial orbitals. Now that the wavefunction is constructed, we can return to the molecular Hamiltonian Equation 1.4. To begin the Hartree Fock self consistent field method, we first take an initial guess at our trial wavefunction, ϕ_i, and solve for the energy. Thanks to the variational theorem, the problem becomes finding the set of orthonormal basis functions that minimizes the energy $E_{variational}$

$$\frac{\int \psi^* \hat{H} \psi}{\int \psi^* \psi} = E_{variational} \geq E_{exact} \tag{1.12}$$

With the constraint that the spin orbitals of the trial wavefunction are orthonormal, we now minimize $E_{variational}$ to get E_0. One can show using Lagrange's undetermined multipliers [40], that the spin orbitals that minimize the energy are given by

$$\varepsilon_a\chi_a(1) = h(1)\chi_a(1) + \sum_{b\neq a}^{occ}[\int |\chi_b(2)|^2 r_{12}^{-1} dx_2]\chi_a(1) - \sum_{b\neq a}^{occ}[\int \chi_b^*(2)\chi_a(2) r_{12}^{-1} dx_2]\chi_b(1) \quad (1.13)$$

Which can be rewritten as

$$\varepsilon_a\chi_a(1) = [h(1) + \sum_{b\neq a}^{occ} \mathscr{J}_b(1) - \sum_{b\neq a}^{occ} \mathscr{K}_b(1)]\chi_a(1) = f_a(1)\chi_a(1) \quad (1.14)$$

Where h(1) is the core hamiltonian for a single electron, $\mathscr{J}_b$ is the local coulomb operator, and $\mathscr{K}_b$ is the non-local exchange operator. The operator $f_a(1)$ in Equation 1.14 is different for every spin orbital χ_a due to the restricted summation. However, it can be shown from Equation 1.13 that $[\mathscr{J}_a(1) - \mathscr{K}_a(1)]\chi_a(1) = 0$. We can therefore drop the restricted summation and define a one electron Fock Operator

$$f(1) = h(1) + \sum_b \mathscr{J}_b(1) - \mathscr{K}_b(1) \quad (1.15)$$

The coulomb term $\mathscr{J}_b(1)$ is represented by the two-electron operator, r_{12}^{-1}, which represents the electron potential felt by electron 1 with respect to the average position of electron 2. By summing over all unique spin orbital combinations, the result is the average total coulombic potential acting on the electron in χ_a by the remaining N-1 electrons defined at x_1. The exchange operator $\mathscr{K}_b$ involves changing the indices on electrons 1 and 2 on right side of the coulomb operator. This is a direct result of the antisymmetry requirement of the single determinant wavefunction. This exchange operator is said to be non-local, as there does not exist a simple potential $\mathscr{K}(x_1)$ uniquely defined at the point x_1. Therefore, one cannot simply draw contour plots of the exchange potential as can be done for the colombic potential [40]. The Hartree Fock equation can now be written

$$f|\chi_a\rangle = \varepsilon_a|\chi_a\rangle \quad (1.16)$$

The solutions given by Equation 1.16 are the canonical spin orbitals χ_a. These are delocalized over the molecule and form a basis for an irreducible representation of the point

group of the molecule. Due to the functional dependence of f(1), Equation 1.16 is a non-linear equation that needs to be solved itteratively. Canonical spin orbitals are de-localized meaning they are not fixed to a particular region of space [32]. Noncanonical spin orbitals are concentrated in certain regions of space and are conveinient for visual representations of bonding and other occupied orbitals. Localized orbitals are no more accurate depiction of the physical system as nonlocalized orbitals [40]. If this is disturbing to your intuition of chemical bonds see England, Salmon, and Ruedenberg (1978) for specific criteria and physical interpretations of such transformations [8] . Furthermore, because f(1) is invariant to a unitary transformation among the occupied orbitals, the resulting Hartree Fock total energy (see Equation 1.21) is the same for the canonical and non-canonical orbitals.

For an N-electron system, once the spin orbitals χ_a are known, the Fock Operator becomes a well defined Hermitian Operator with a complete set of orthonormal eigenfunctions $|\chi_j\rangle$ with corresponding orbital energies ε_j. The N lowest orbital energies are occupied in the ground state wave function $|\Psi_0\rangle$ and given the indexed beginning at a,b,.... The remaining unoccupied virtual orbitals are indexed r,s,.... In a basis of a complete set of orthonormal spin orbital eigenfunctions, the Fock operator in matrix form is diagonal with those elements equal to ε_j. This can be seen by examining the expectation value given by

$$\int \chi_i f \chi_j d\tau = \varepsilon_j \int \chi_i \chi_j = \varepsilon_j \delta_{ij} \tag{1.17}$$

Which is equivalent to

$$\langle \chi_i | f | \chi_j \rangle = \varepsilon_j \langle \chi_i | \chi_j \rangle = \varepsilon_j \delta_{ij} \tag{1.18}$$

Using Equation 1.14 and our definitions for $\mathscr{J}$ and $\mathscr{K}$ we then arrive at the following expressions for the occupied and virtual orbital energies

$$\varepsilon_a = \langle a|h|a\rangle + \sum_{b \neq a} \langle a| \mathscr{J}_b |a\rangle - \langle a| \mathscr{K}_b |a\rangle \tag{1.19}$$

$$\varepsilon_r = \langle r|h|r\rangle + \sum_{b} \langle r| \mathscr{J}_b |r\rangle - \langle r| \mathscr{K}_b |r\rangle \tag{1.20}$$

The exchange integral involving $\mathscr{K}$ is zero if the spins of the electrons in a and b are

antiparallel. The total energy of the ground state wavefunction is given by

$$E_0 = \langle \Psi_0 | \mathscr{H} | \Psi_0 \rangle = \sum_a^N \langle a|h|a\rangle + \frac{1}{2}\sum_a [\sum_b \langle a| \mathscr{J}_b |a\rangle - \langle a|\mathscr{K}_b|a\rangle] \tag{1.21}$$

Note that simply summing over all of the occupied orbital energies ε_a does not give E_0. A factor of $\frac{1}{2}$ is added in the coulomb and exchange integrals. This is necessary as the interactions felt by the electron in χ_a on all the other electrons, including χ_b are accounted for in ε_a. Likewise, all interactions felt by the electron in χ_b including χ_a are contained in ε_b. Thus the coulomb and exchange interactions are all counted twice and a correction for this is needed for the correct total energy expression [40].

Using Equations 1.19 and 1.20 for our orbital energies leads to Koopman's theorem which states that the under Hartree Fock theory, the ionization energy to produce an (N-1)-electron single determinant with identical spin orbitals is equal to $-\epsilon_a$. Likewise the electron affinity to produce an (N+1)-electron single determinant with the same orbitals is $-\varepsilon_r$ [40]. This is also referred to as the frozen orbital approximation as it neglects the relaxation of the spin orbital energies as more or less variational freedom is introduced when an electron is removed or added to the system. For this reason calculations performed under Koopman's approximation tend to overestimate ionization potentials and underestimate electron affinities.

The Hartree Fock approximation to the ground state wavefunction $|\Psi_0\rangle$ is the N χ_a that give the lowest orbital energies. Clearly, there are many other determinants that could be formed from the complete set of χ_i. The subset of singly excited $|\Psi_a^r\rangle$ and doubly excited $|\Psi_{ab}^{rs}\rangle$ and higher order determinants are also expected to contribute to the true ground state wavefunction. In solving for the orbital energies, the off diagonal matrix elements given by $\langle \Psi_0|\mathscr{H}|\Psi_a^r\rangle$ are all equal to zero. This is stated explicitly in Brillouin's theorem. Singly excited determinants can however mix with $|\Psi_0\rangle$ indirectly through $\langle \Psi_a^r|\mathscr{H}|\Psi_{ab}^{rs}\rangle$ and $\langle \Psi_{ab}^{rs}|\mathscr{H}|\Psi_0\rangle$.

From Equation 1.9 we have a set of restricted spin orbitals, requiring the same spatial function $\phi(r)$ for both α and β spin functions with corresponding closed-shell ground state Ψ_0. Operating on $\chi_i(1)$ with f(1) and integrating over the spin coordinate ω_1 and ω_2 results

in the closed-shell Fock operator which has the form

$$f(r_1)\phi_i(r_1) = \varepsilon_i \phi_i(r_1) \tag{1.22}$$

Which is simplified due to the equivalence of the two coulombic terms and spin orthogonality, because there is no exchange interaction between electrons of antiparallel spin. Now that spin has been eliminated, we now are ready to introduce a basis set and solve for the spatial molecular orbitals.

Introducing a set of K basis functions in accordance with Equation 1.8

$$\phi_i = \sum_{\mu=1}^{K} C_{\mu i}\Theta_\mu \qquad i = 1, 2, ..., K \tag{1.23}$$

Solving for the orbital expansion coefficients $C_{\mu i}$ can be obtained by multiplying Equation 1.22 by $\phi_n u^*(r_1)$ on the left and integrating over all space to produce the matrix equation

$$\sum_{\nu} C_{\nu i} F_{\mu\nu} = \varepsilon_i \sum_{\nu} S_{\mu\nu} C_{\nu i} \tag{1.24}$$

The Fock matrix $\mathbf{F}$ has elements $F_{\mu\nu}$ given by

$$\begin{aligned} F_{\mu\nu} &= \int dr_1 \phi_\mu^*(r_1) f(r_1) \phi_\nu(r_1) \\ &= \int dr_1 \phi_\mu^*(r_1) h(r_1) \phi_\nu(r_1) + \sum_{a}^{N/2} \int dr_1 \phi_\mu^*(r_1)[2J_a(r_1) - K_a(r_1)]\phi_\nu(r_1) \\ &= H_{\mu\nu}^{core} + G_{\mu\nu} \end{aligned} \tag{1.25}$$

Where $F_{\mu\nu}$ is the K x K matrix representation for the one electron Fock operators $f(r_1)$ in the basis $\phi_m u$. In Equations 1.24 and 1.25 we have also defined an overlap matrix, $\mathbf{S}$ with elements

$$S_{\mu\nu} = \int dr_1 \phi_\mu^*(r_1)\phi_\nu(r_1) \tag{1.26}$$

The overlap matrix would be a unit matrix if all of the basis functions were mutually orthogonal. Although the introduced ϕ_μ is normalized and linearly independent it is not orthogonal and the overlap matrix elements have magnitude $0 \leq |S_{(\mu\nu)}| \leq 1$. An overlap of one indicates complete overlap of the basis functions, hence the diagonal elements of $S_{\mu\nu}$

are unity. If any of the off diagonal elements approach unity then the basis set approaches a linear dependency. Linear dependencies from nonorthogonality of the basis set causes SCF convergence issues and gives energy eigenvalues of zero. These can be resolved by removing a small part of the basis set, typically associated with eigenvalues of the overlap matrix which are less than 10^{-4} Hatrees[40].

The closed shell Hartree Fock equations in matrix form as we have just described are known as the Roothaan equations which are typically written

$$\mathbf{FC} = \mathbf{SC}\varepsilon \tag{1.27}$$

Where $\mathbf{C}$ is a K x K matrix of the orbital expansion coefficients and ε is diagonal matrix of the corresponding orbital energies. The a-th column corresponds to the orbital expansion coefficient for χ_a.

As we have mentioned, our introduced set of basis functions ϕ_i are not mutually orthogonal which leads to a non-zero overlap matrix. For this reason we first need to orthogonalize the basis set before $\mathbf{F}$ can be diagonalized to obtain the eigenvectors $\mathbf{C}$ and corresponding eigenvalues ε. Removing the overlap matrix by orthogonalizing the basis can be done by introducing a non-unitary transformation matrix $\mathbf{X}$ defined in the following

$$\mathbf{C}' = \mathbf{X}^{-1}\mathbf{C} \tag{1.28}$$

$$\mathbf{C} = \mathbf{X}\mathbf{C}' \tag{1.29}$$

$$\mathbf{F}' = \mathbf{X}^{\dagger}\mathbf{F}\mathbf{X} \tag{1.30}$$

$$\mathbf{X}^{\dagger}\mathbf{X} \neq \mathbf{X}\mathbf{X}^{\dagger} \neq \mathbf{I} \tag{1.31}$$

Where $\mathbf{I}$ is the identity matrix and $\mathbf{X}^{\dagger}$ is the complex transpose of $\mathbf{X}$. The assumption that $\mathbf{X}$ has an inverse $\mathbf{X}^{-1}$ is only true if there are no linear dependencies in the basis set. Linear dependency problems can be removed by canonical orthogonalization.

The transformed Roothaan equations can be written

$$\mathbf{F}'\mathbf{C}' = \mathbf{C}'\varepsilon \tag{1.32}$$

Diagonalization of $\mathbf{F}'$ gives the expansion coefficients in transformed basis $\mathbf{C}'$. Using Equations 1.28-1.30 the Roothaan Equations 1.27 can be solved for $\mathbf{C}$ and ε. The basis set of one electron spatial wavefunctions $\phi_i(r)$ have probability distribution function $|\phi_i(r)|^2$. Summing this probability over all of the occupied orbitals we can write the total charge density as

$$\rho(r) = 2\sum_{a}^{N/2} |\phi_a(r)|^2 \tag{1.33}$$

The probability of finding an electron at location r is given by $\rho(r)$ and the integral of this probability over dr to N, the total number of electrons. Using Equation 1.21 we can expand this expression in terms of molecular orbital expansion coefficients and form a density matrix $\mathbf{P}$ containing elements defined by

$$P_{\mu\nu} = 2\sum_{a}^{N/2} C_{\mu a}C_{\nu a}^{*} \tag{1.34}$$

This charge-density bond order matrix as it is often called is thus completely specified by the molecular orbital expansion coefficients. We can therefore summarize the results of closed shell Hartree Fock calculations by using either $\mathbf{C}$ or $\mathbf{P}$.

In practice, to solve for $|\Psi_0\rangle$ a basis set is introduced so that a trial function in the form of $\mathbf{C}$ is generated. The variational principle is then used to minimize the energy and acquire a new $\mathbf{C}$. This process is repeated until the same final energy is attained, at which point the calculation has converged and we have the best estimate for the ground state wavefunction and corresponding energy for the given basis set size. This is the self consistent field or SCF procedure which is outlined in detail below.

HartreeFock/SCF Instructions :

1. Specify nuclear coordinates R_A, atomic numbers Z_A, number of electrons N, and basis set ϕ_μ.
2. Calculate $S_{\mu\nu}$, $H_{\mu\nu}^{core}$, and $\int dr_1 dr_2 \phi_\mu^*(r_1)\phi_\nu(r_1)r_{12}^{-1}\phi_\lambda^*(r_2)\phi_\sigma(r_2)$
3. Diagonalize $\mathbf{S}$ and obtain $\mathbf{X}$
4. Guess $\mathbf{P}$
5. Calculate $\mathbf{G}$ from $\mathbf{P}$.
6. Add $\mathbf{G}$ to $\mathbf{H^{core}}$ to get $\mathbf{F}$
7. Calculate the transformed Fock matrix $\mathbf{F'} = \mathbf{X}^\dagger\mathbf{F}\mathbf{X}$
8. Diagonalize $\mathbf{F'}$ to get $\mathbf{C'}$ and ε
9. Calculate $\mathbf{C} = \mathbf{X}\mathbf{C'}$
10. Form a new $\mathbf{P}$ from $\mathbf{C}$ using Equation 1.34
11. Is $\mathbf{P}$ unchanged? If no, return to step 5. If yes continue to step 12.
12. Use $\mathbf{C}, \mathbf{P}, \mathbf{F}$,etc. to calculate expectation values.

A converged SCF procedure is one in which the final density matrix remains unchanged after subsequent SCF iterations. The result is the ground state wave function $|\Psi_0\rangle$ and corresponding electronic energy E_0 for a set of N electrons in a field of M point charges from the M nuclei with charges Z_A. The nuclear-nuclear repulsion term added to the electronic energy ε_{elec} gives a total energy as a function of nuclear coordinates $E_0(R_A)$. The converged energy E_0 is the exact solution of the Hartree Fock Hamiltonian which is most readily calculated by Equation 1.21. This is obtained from the Hartree Fock Hamiltonian written as a sum of one-electron Fock operators given by

$$\mathscr{H} = \sum_{i=1}^{N} f(i) \tag{1.35}$$

which provides a complete set of eigenfunctions with coresponding eigenvalues

$$E_0^{(exact)} = E_0^{(0)} + E_0^{(1)} + E_0^{(2)} + ... \tag{1.36}$$

Where the zero order energy

$$E_0^{(0)} = \sum_a \varepsilon_a \tag{1.37}$$

Is from

$$\mathscr{H}_0|\Psi_0\rangle = E_0^{(0)}|\Psi_0\rangle \tag{1.38}$$

Solving the Hartree Fock Hamiltonian is not a solution to the exact Schrödinger equation. It turns out though this is a decent approximation with a large enough basis set. Hartree Fock theory provides not only an intuitive picture for chemists of electrons populating orbitals in a fixed field of nuclei, but it also provides a complete set of eigenfunctions as a basis which can be used in a perturbation expansion of the exact energy.

It turns out that the energy given by our ground state Hartree Fock wavefunction $E_0 = E_0^{(0)} + E_0^{(1)}$ and Hartree Fock theory is equivalent to first order perturbation treatment theory. Hartree Fock energies typically contain about 0.5-1.0% error relative to the exact energy[32, 40]. This error may not sound significant but for H_2O, the total energy is on the order of -100 Hartrees, 1 % of that is 2625.5 kJ/mol, so for accurate computational results, post Hartree Fock electron correlation methods should be addressed.

Open Shell Systems

The preceeding discussion was for closed shell systems with no unpaired electrons. For open shell systems, one common approach is to use an unrestriced form of the spin orbitals. Analogous to Equation 1.11 we write these as

$$\left.\begin{aligned}\chi_{2i-1}(r,\omega) &= \phi_i^{\alpha}(\vec{r_i})\alpha(\omega)\\ \chi_{2i}(r,\omega) &= \phi_i^{\beta}(\vec{r_i})\beta(\omega)\end{aligned}\right\} i = 1,2,...,K \tag{1.39}$$

In this unrestricted approach, the electrons that have α spin are now described by a different set of spatial functions than those with β spin. Similar to the closed shell one electron Fock Equation 1.22 the unrestricted procedure yields two Fock equations

$$f(r_1)^{\alpha}\phi_i^{\alpha}(r_1) = \varepsilon_i^{\alpha}\phi_i^{\alpha}(r_1) \tag{1.40}$$

$$f(r_1)^{\beta}\phi_i^{\beta}(r_1) = \varepsilon_i^{\beta}\phi_i^{\beta}(r_1) \tag{1.41}$$

To solve these unrestricted Hartree Fock equations a set of basis functions is introduced which give a set of mutually orthogonal α and β molecular orbitals ϕ_i^{α} andϕ_i^{β} guaranteed by Equations 1.40 and 1.41. The symmetry of the alpha and beta treatment here naturally

gives two Roothaan-like matrix equations which can be conveniently written

$$\mathbf{F}^{\alpha}\mathbf{C}^{\alpha} = \mathbf{S}^{\alpha}\mathbf{C}^{\alpha}\varepsilon^{\alpha} \tag{1.42}$$

$$\mathbf{F}^{\beta}\mathbf{C}^{\beta} = \mathbf{S}^{\beta}\mathbf{C}^{\beta}\varepsilon^{\beta} \tag{1.43}$$

These are the Pople-Nesbit equations and have corresponding unrestricted density matrices [40]

$$P^{\alpha}_{\mu\nu} = \sum_{a}^{N_{\alpha}} C^{\alpha}_{\mu a} C^{\alpha *}_{\nu a} \tag{1.44}$$

$$P^{\beta}_{\mu\nu} = \sum_{a}^{N_{\beta}} C^{\beta}_{\mu a} C^{\beta *}_{\nu a} \tag{1.45}$$

The total charge density is then simply the sum of the alpha and beta contributions. At this point, to begin an unrestricted Hartree Fock calculation (UHF), an initial guess is first taken at ρ^{α} and ρ^{β} and then one can enter the SCF procedure outlined above. As the Pople Nesbit equations mirror the Roothaan equations, it is no surprise that when N^{α}=N^{β} (as in a closed shell) a solution to the Pople Nesbit equations also converges to the closed shell Roothan equations. This result also necessarily results if an initial guess where $\rho^{\alpha} = \rho^{\beta}$ is used. There also may exist however, a second unrestricted solution to this scenario of a lower energy. This special case is usually only of importance for dissociation problems.

Expectation Values and Population Analysis

The result of our ab initio SCF procedure is a converged electron charge density as given by Equation 1.31. As this gives the probability of finding an electron in some localized region of space, many find this comforting and then go on to plot things like total charge density contours to as a visual interpretation. For others, that seek a more analytical analysis, we can calculate charge moments (dipole, quadrupole, etc.). As we already have addressed localization and issues in interpretation, it is known that it is not detrimental to the data and there really is no rigorous way of doing so. What can still be done are Mulliken and Löwdin population analysis to get a general idea of where some of these charges are located. General trends can can be observed in such analysis but the magnitudes of these charges

are not accurate. As with most computational recipies, comparing results among different basis sets or methods does not give comparable results.

1.3.2 Post Hartree Fock Methods

The electron-electron repulsion, final term in the molecular Hamiltonian given by Equation 1.4 gives rise to electron correlation. The r_{ij} vector results in the motions of electrons i and j being dependent upon each other. In general, the electrons try to avoid each other. Hartree Fock theory naturally includes some of the correlation between electrons of the same spin due to the anti-symmetry of the wavefunction. This satisfies the antisymmetry of the wavefunction with respect to the exchange of any two electrons and is referred to as *Pauli exchange*. The correlation between electrons of opposite spin however is much larger and is not accounted for in a single Slater determinant [26].The Hartree Fock equations essentially average over the positions of the electrons, ignoring their instantaneous correlation. In other words, in the Hartree Fock approximation, electrons of opposing spin do not avoid one another as they are all restricted to the ground state determinant by definition. Computational methods that go beyond the Hartree Fock approximation are often referred to as electron correlation methods even though Hartree Fock theory does actually include some correlation energy. Conceptually, Configuration Interaction theory is the simplest post Hartree Fock method in which the electronic wavefunction is written as a linear combination of several Slater determinants to give an estimate for the correlation energy. Many of these post Hartree Fock methods involve mixing multiple determinants to represent the wavefunction. Configuration interaction is a variational method but is only size consistent when all possible configurations are included in the trial function. Performing full configuration interaction is very computationally expensive and is not further discussed here. More computationally efficient methods include Møller-Plesset perturbation theory and Coupled-Cluster theory which are discussed in the following sections.

1.3.3 Møller-Plesset perturbation theory

Møller-Plesset perturbation theory (MPPT) partitions the full molecular Hamiltonian $\hat{H}$ in Equation 1.4 into a zero order Hamiltonian $\mathscr{H}_0$ given by Equation 1.38.

$$\hat{H}_{MP} = \mathscr{H}_0 + \hat{V} \tag{1.46}$$

First developed in the 1930s, Møller-Plesset perturbation theory is an application of Rayleigh-Schrödinger perturbation theory to the Hartree Fock Hamiltonian. MPPT comes in a series of orders and is noted MPn, where n indicates the order of incorporated excitations. As mentioned above, zeroth order is just the sum of orbital energies and first order Møller-Plesset perturbation theory yields the Hartree Fock energy. MP2, MP3, and MP4 involve wavefunctions with excited determinants and can be represented

$$E^{(2)} = E^{HF} - \sum_{s\neq 0} \frac{|\langle\psi_0|\hat{V}|\psi_s\rangle^2}{E_s - E_0} = E^{HF} - \frac{1}{4}\sum_{abrs} \frac{|\langle ab||rs\rangle|^2}{\varepsilon_r + \varepsilon_s - \varepsilon_a - \varepsilon_b} \tag{1.47}$$

$$E^{(3)} = E^{(2)} - \sum_{st} \frac{|\langle\psi_0|\hat{V}|\psi_s\rangle\langle\psi_s|\hat{V}|\psi_t\rangle\langle\psi_t|\hat{V}\psi_0\rangle}{(E_s - E_0)(E_t - E_0)} \tag{1.48}$$

$$E^{(4)} = E^{(3)} - \sum_{stu} \frac{|\langle\psi_0|\hat{V}|\psi_s\rangle\langle\psi_s|\hat{V}|\psi_t\rangle\langle\psi_t|\hat{V}\psi_u\rangle\langle\psi_u|\hat{V}\psi_0\rangle}{(E_s - E_0)(E_t - E_0)(E_u - E_0)} \tag{1.49}$$

These orders of MPPT are truncated expressions for the total energy which contain an infinite number of terms of increasing complexity. This can make higher order MPPT computationally expensive but if $\mathscr{H}$ is partitioned wisely, the calculation can still converge rather quickly. For most cases MP2 gives energies of reasonable approximation, yet MPPT is not variational so the solution is not always an upper bound to the exact energy. MPPT is also size extensive at every level, so we do not run into additive separability issues which occur in CI calculations when the excitation levels are truncated.

1.3.4 Coupled Cluster Theory

Another multi-determinantal approach that goes beyond Hartree Fock theory introduces an excitation operator $\mathscr{T}$ to make an exponential expansion of the Hartree Fock wavefunction $|\Psi_0\rangle$

$$|\Psi_{CCA}\rangle = exp(\mathscr{T})|\Psi_0\rangle \tag{1.50}$$

With

$$\mathscr{T} = \mathscr{T}_1 + \mathscr{T}_2 + ... \tag{1.51}$$

$$\mathscr{T}_1 = \sum_{ra} c_a^r a_r^\dagger a_a \tag{1.52}$$

$$\mathscr{T}_2 = \sum_{abrs} c_{ab}^{rs} a_r^\dagger a_s^\dagger a_b a_a \tag{1.53}$$

Where the subscripts indicate single, double, triple, etc. excitations produced by the creation $a_r^\dagger$ and annihilation a_a operators. The operators a_a, a_b remove occupied spin orbitals from $|\Psi_0\rangle$ and $a_r^\dagger$,$a_s^\dagger$ replace these with unnocupied spin orbitals. After expanding Equation 1.50 in a Taylor series, the wavefunction under the Coupled-Cluster approximation can be written after some manipulation [40]

$$|\Psi_{CCA}\rangle = \Psi_0 + \sum_{\substack{a<b \\ r<s}} c_{ab}^{rs} |\Psi_{ab}^{rs}\rangle + \sum_{\substack{a<b<c<d \\ r<s<t<u}} c_{abcd}^{rstu} |\Psi_{abcd}^{rstu}\rangle + ... \tag{1.54}$$

Where the coefficients of the single and doubly excited determinants are c_a^r and c_{ab}^{rs} respectively. Coupled cluster theory using only double excitations ($\mathscr{T}_2$) is commonly called CCD, with doubles and singles ($\mathscr{T}_1 + \mathscr{T}_2$) are CCSD. The energy at this extent , E_{CCSD}, is solved iteratively using a non-linear set of equations resulting from the projection of $|\Psi_{CCSD}\rangle$ onto $|\Psi_0\rangle$ [26]. The CCSD method can be used to then be used as a starting point to account for most of the contributing triply excited determinants to give $E_{CCSD(T)}$. The expression for this energy follows the form

$$E_{CCSD(T)} = E_{CCSD} - \frac{1}{36} \sum \frac{|u_{abc}^{rst}|^2}{\varepsilon_r + \varepsilon_s + \varepsilon_t - \varepsilon_a - \varepsilon_b - \varepsilon_c} \tag{1.55}$$

Where u_{abs}^{rst} are the matrix elements of the Hamiltonian between the CCSD single and double excitation amplitudes and the triply excited determinant, accounting for most of the triple

excitations but not all of them. This is a much more practical method than the full CCSDT treatment in terms of computational costs and is often referred to as the gold standard for electron correlations methods if a large enough basis set is used.

1.3.5 Density Functional Theory

Post Hartree Fock calculations give accurate correlation energies but come at a high computational cost. Modeling larger systems therefore becomes increasingly difficult to do using a practical amount of computer time. Thanks to Pierre Hohenberg and Walter Kohn who stated and proved in their 1964 paper *Inhomogeneous Electron Gas* the Hohenberg Kohn postulates which state:

1. The ground-energy from Schödinger's equation is a unique functional of the electron density.
2. The electron density that minimizes the energy of the overall functional is the true electron density corresponding to the full solution of the Schrödinger equation [39].

A functional is essentially a function of a function. That is if you have a function, say $\rho = \rho(r) = 2\sum_i \phi(r)_i^* \phi(r)_i$ where i sums over the occupied orbitals, then you could have a functional of that function $E(\rho)$ that when evaluated can produce the energy and the wavefunction of the ground state. This powerful theorem reduces the problem of solving the molecular Schrödinger equation with 3N spatial coordinates to a problem with only three spatial variables that describe the overall electron density. This is the foundation of Density Functional Theory, DFT. With the first theorem we can effectively "solve" the Schrödinger equation with this clever trick, but still gives no insight as to what the actual wave functional and wave function are. Theorem two confirms that we have the true electron density corresponding to the true functional, yet we still do not have the true form of that functional. Recall that collapsing the wave function gives an electron probability density $\rho(r)$ as in Equation 1.33. Although DFT is not wavefunction based, its general procedure parallels that of the Hartree Fock/SCF which also contributes to its overall efficiency. From

Equation 1.6 we write the electronic Hamiltonian for n electrons and N nuclei

$$\hat{H} = -\frac{1}{2}\sum_{i}^{n}\nabla_i^2 + \sum_{i=1}^{n} v(r_i) + \sum_{j}\sum_{i>j}\frac{1}{r_{ij}} \tag{1.56}$$

Where

$$v(r_i) = -\sum_{\alpha}^{N}\sum_{i}^{n}\frac{Z_\alpha}{r_{i\alpha}} \tag{1.57}$$

is the external potential acting on electron i produced by the fixed field of nuclei. By theorem one, for systems with a non-degenerate ground state, there exists a ground stat electron density $\rho_0(r)$ that determines the number of electrons, $v(r_i)$,and therefore the ground state wavefunction Ψ_0 and ground state energy E_0[32]. The second theorem is the Hohenberg-Kohn variational theorem and just as the ground state wavefunction minimized the variational energy as in Equation 1.12 we can write

$$E_{DFT}[\rho(r)] \geq E_0 = E(\rho_0) \tag{1.58}$$

We can now minimize the energy given by

$$E_{DFT}[\rho(r)] = T[\rho(r)] + V_{Ne} + V_{ee}[\rho(r)] \tag{1.59}$$

This expression should look somewhat familiar. The first term represents the kinetic energy of the electrons, the second is the coulombic attraction between the electrons and nuclei and the last term is the electron-electron repulsion term. Just as a trial wavefunction was introduced in the Hartree Fock/SCF procedure, we now introduce a trial electron density $\rho_{tr}(r)$ as in

$$[T[\rho_{tr}(r)] + V_{ee}[\rho_{tr}(r)] + \int \rho_{tr}(r)v(r)dr] \geq E[\rho_0] \tag{1.60}$$

Where we have explicitly stated the form of the external potential, the form of the functionals $T[\rho_{tr}(r)]$ and $V_{ee}[\rho_{tr}(r)]$ are still unknown. One year after the Hohenberg Kohn postulates were published, Walter Kohn and Lu Jeu Sham published the Kohn-Sham equations which provide a practical way to find ρ_0 to then calculate E_0. To do this, Kohn and Sham considered a fictitious reference system, denoted by s, of n noninteracting electrons. Because these electons do not interact with one another, the Hamiltonian of this ficticious

system is

$$\hat{H}_s = \sum_{i=1}^{n}[-\frac{1}{2}\nabla_i^2 + v_s(r_i)] = \sum_{i=1}^{n}\hat{h}_i^{KS} \tag{1.61}$$

The ground state wavefunction of such a system of noninteracting particles would be a Slater determinant of the lowest energy Kohn-Sham spin orbitals whose spatial components are eigenfunctions of the one electron Kohn-Sham Hamiltonian

$$\hat{h}_i^{KS}\phi_i^{KS} = \varepsilon_i^{KS}\phi_i^{KS} \tag{1.62}$$

We now make two definitions

$$\Delta T[\rho(r)] = T[\rho(r)] - T_s[\rho(r)] \tag{1.63}$$

$$\Delta V_{ee}[\rho(r)] = V_{ee}[\rho(r)] - \frac{1}{2}\int\int\frac{\rho(r_1)\rho(r_2)}{r_{12}}dr_1dr_2 \tag{1.64}$$

Now we can rewrite (1.59) as

$$E[\rho_0] = \int\rho(r)v(r)dr + T_s[\rho_0] + \frac{1}{2}\int\int\frac{\rho(r_1)\rho(r_2)}{r_{12}}dr_1dr_2 + E_{xc}[\rho_0] \tag{1.65}$$

The first three terms on the right of Equation 1.65 are fairly easy to evaluate once ρ is obtained. The final term $E_{xc}[\rho_0]$ is usually small in comparrison to the overall energy but is not easy to evaluate accurately. For this reason $E_{xc}[\rho_0]$ is the limiting factor to accurate DFT calculations. The kinetic energy of the system of noninteracting electrons represented by a Slater determinant of orthonormal Kohn-Sham spin-orbitals. Integrating over the spin coordinates then gives $T_s[\rho_0] = -\frac{1}{2}\sum_{i=1}^{n}\langle\phi_i^{KS}(r_1)|\nabla_{r_1}^2|\phi_i^{KS}(r_1)\rangle$ which substituted into Equation 1.65 gives E_0. To get the Kohn-Sham orbitals

$$E_0 = -\sum_\alpha Z_\alpha\int\frac{\rho(r_1)}{r_{1\alpha}}dr_1 - \frac{1}{2}\sum_{i=1}^{n}\langle\phi_i^{KS}(r_1)|\nabla_{r_1}^2|\phi_i^{KS}(r_1)\rangle + \frac{1}{2}\int\int\frac{\rho(r_1)\rho(r_2)}{r_{12}}dr_1dr_2 + E_{XC}[\rho_0] \tag{1.66}$$

It can be shown[1] that the orbitals that minimize the energy given by Equation 1.66 also satisfy Equation 1.62 with the one electron Kohn-Sham Hamiltonian written as

$$\hat{h}_i^{KS} = [-\frac{1}{2}\nabla_1^2 - \sum_\alpha\frac{Z_\alpha}{r_{1\alpha}} + \int\frac{\rho(r_2)}{r_{12}}]dr_2 + v_{xc}(r_1) \tag{1.67}$$

[1]The proof of this is shown in *ParrandYang* which also contains a proof of the Hohenberg-Kohn postulates [32]

Where the exchange-correlation potential v_{XC} is defined by the functional derivative [32]

$$v_{XC}(r) \equiv \frac{\delta E_{XC}[\rho(r)]}{\delta \rho(r)} \tag{1.68}$$

Note the similarities between Equation 1.68 and the one electron Fock operator 1.15. Both can be broken up into a known portion (the core hamiltonian $h(1)$ in Equation 1.15 or the first three terms in Equation 1.67), and an unknown portion. The main difference is the Kohn-Sham orbitals do not contain any bit of Hartree Fock exchange K. Pure DFT functionals eliminate this term entirely [26] whereas some hybrid functionals include a form of Hartree Fock exchange which will be discussed momentarily. In any DFT functional however, the $E_{xc}[\rho(r)]$ term includes exchange and correlation energies, parts of which are neglected by Hartree Fock theory [26].

We are now in a position to discuss the infamous exchange correlation term in DFT calculations. There are two main flavors that E_{xc} comes in, the local density approximation (LDA) and the generalized gradient approximation (GGA). In both cases the exchange-correlation energy can be represented as a simple sum of the two components

$$E_{xc} = E_x + E_c \tag{1.69}$$

If the electron density varies extremely slowly with respect to position, then E_{xc}^{LDA} is a good approximation and can be written in a general form as

$$E_{xc}^{LDA} = \int \rho(r)\hat{V}_x^{LDA}(\rho(r))dr + \int \rho(r)\hat{V}_c^{LDA}(\rho(r))dr \tag{1.70}$$

$$E_{xc}^{GGA} = \int \rho(r)\hat{V}_x^{GGA}(\rho(r), \nabla\rho(r))dr + \int \rho(r)\hat{V}_c^{GGA}(\rho(r), \nabla\rho(r))dr \tag{1.71}$$

Once an approximate form for E_{xc} is obtained, E_0 and $\rho(r)$ and ϕ_i^{KS} can all be obtained. This is done by constrained optimization of Equation 1.67. One can either minimize E_0 with respect to $\rho(r)$ with the condition that $\int \rho(r)dr = N$, the number of electrons. Alternatively, one can optimize ϕ_i^{ks} to get $\rho(r)$ with the constraint of orthonormality as necessary for $T_s[\rho(r)]$. This process is indeed cyclic and to break this cycle we will use an iterative approach as in the SCF method. The DFT-SCF procedure follows[39]:

1. Define an initial, trial electron density, $\rho(r)$. This is usually a superposition of atomic electron densities calculated from the nuclear coordinates.

$$\rho(r) = 2\sum_{i}^{occ} \phi(r)_i^* \phi(r)_i \tag{1.72}$$

2. Solve the Kohn-Sham equations using this trial electron density to find the single-particle wave functions. This is done by first calculating v_{xc} using Equation 1.66 and your exchange-correlation functional of your choice. This is then used in Equation 1.65 to get an initial estimate of the Kohn-Sham orbitals ϕ_i^{KS}. In this step, the ϕ_i^{KS}'s are are expanded as sets of basis functions and yield equations similar to the Roothaan Equations 1.27. The result is an altered Fock matrix

$$F_{\mu\nu}^{DFT} = H_{\mu\nu}^{core} + J_{\mu\nu}(P_{\lambda\sigma}) + \sum_{g} w_g F_{\mu\nu}^{xc}[\rho(r)] \tag{1.73}$$

   Where the second term involves the coulombic matrix elements previously seen in the Fock matrix defined by Equation 1.25.
3. The initially calculated ϕ_i^{KS}'s are then used to obtain a new electron density using Equation 1.33.
4. If $\rho(r)$ has changed, it must be varied and the process is repeated from step 2. If $\rho(r)$ is unchanged, the calculation has converged. This is the best estimate of to ρ_0 within the method used and the total energy is then computed.

Although v_{xc} is dependent on the functional used, it is a very complicated function of the coordinates. This accounts for the biggest difference between the Hartree Fock and DFT SCF procedures. In DFT $\langle\chi_r|v_{xc}|\chi_s\rangle$ must be solved numerically by evaluation of the integrand along a grid of points. The DFT SCF procedure gives an estimate for electron correlation energies whereas the Hartree Fock SCF procedure does not. DFT SCF results can therefore be used directly in energetic calculations.

Periodic Boundary Conditions

A benefit of DFT to post Hartree Fock electron correlation methods aside from computational efficiency is the ability to model periodic systems. Recall the classic particle in a box problem with the following Hamiltonian and solution

$$\frac{-\hbar^2}{2m}\nabla^2\Psi(x,y,z) = E\Psi(x,y,z) \tag{1.74}$$

$$\Psi(x,y,z) = Csin\frac{\pi n_x x}{L}sin\frac{\pi n_y y}{L}sin\frac{\pi n_z z}{L} \tag{1.75}$$

$$E = \frac{h^2(n_x^2+n_y^2+n_z^2)}{8mL^2} \qquad n_{x,y,z} = 1,2,... \tag{1.76}$$

where C is a normalization constant, m is the mass of the particle, and L is the length of the box. Introducing periodic boundary conditions simply imposed the requirement

$$\Psi(x,y,z) = \Psi(x+L,y,z) = \Psi(x,y+L,z) = \Psi(x,y,z+L) \tag{1.77}$$

A solution to this problem is now a set of traveling plane waves in reciprocal space

$$\Psi(\vec{k},\vec{r}) = exp(i\vec{k}\vec{r}) \tag{1.78}$$

$$E = \frac{\hbar^2}{2m}\vec{k}^2 \tag{1.79}$$

Where $\vec{k}$ is a wave vector with momentum $\vec{p} = \hbar\vec{k}$ and allowed values determined by the lattice. If we have a cubic lattice with side lengths L then

$$k_x = k_y = k_z = 0, \frac{2\pi}{L}, \frac{4\pi}{L}, ... \tag{1.80}$$

Note that the allowed values of the wavevector $\vec{k}$ depend on the reciprocal of L in the above expression. The terms K-space and reciprocal space are often used interchangeably and is a related through a Fourier transform of the real space lattice vectors. Periodic systems in three-space provide an ideal situation for a Fourier analysis and it turns out that the most interesting properties of crystals are directly related to the Fourier components of the electron density $n(\vec{r})$[30]. Given a primitive unit cell in real space, called a Wigner-Seitz cell, an equivalent primitive unit cell can be defined in reciprocal space. At the boundaries of

this Brillouin zone, the group velocity of the plane waves defined by $\vec{k}$ become zero resulting in Bragg reflection yielding quantization in K-space as shown in Equation 1.70.

Returning to the our discussion of DFT on periodic boundary conditions, we can begin the DFT-SCF procedure by first defining a trial electron density given by

$$\rho(\vec{r}) = \sum_i \int_{BZ} n(\vec{k}) |\Psi_i(\vec{k})|^2 d\vec{k} \tag{1.81}$$

As shown by Felix Bloch, the solutions to the Schrödinger equation for periodic potential follows the form

$$\Psi(\vec{k}, \vec{r}) = u(\vec{k}, \vec{r}) exp(i\vec{k} \cdot \vec{r}) \tag{1.82}$$

The above expression represents the Block Theorem. The first term contains the periodicity of the crystal lattice and the second is the plane wave of an individual electron. Using Equations 1.72 in 1.71, the Bloch functions are integrated over the space defined by the Brillouin zone, referred to as k-sampling, and gives a corresponding effective potential. This effective potential is used to solve the Kohn-Sham equations in step 2 of the DFT-SCF procedure. At this point, the the DFT-SCF procedure is the same as described in the above section. The most important result again being the total energy of the system.

Pseudopotentials

There is one remaining issue with DFT calculations in systems with periodic boundary conditions. The plane wave solution to the electronic Hamiltonian represents well the electrons in the conduction orbitals. Outside the core region the potential energy due to the positively charged nuclei is only slightly screened by the neighboring electrons and the wavefunction is well approximated by plane waves. This is not the case for the core electrons and therefore they must be treated differently. What goes on in the core region is mostly independent of $E(\vec{k})$. The nodal structure of these core regions are often complex, for instance in Sodium, the 3s orbital must have two nodes to be orthogonal to both the 2s core orbital with one node and the 1s orbital with no nodes. These orthogonality constraints between the valence and core orbitals often lead to convergence issues when running plane wave calculations.

Given that these core electrons are mostly chemically inert, we therefore use Pseudopotentials to represent the core regions. This means to replace the potential energy and filled electrons in the core region by an effective potential energy, or Pseudopotential, that yields the same wavefunction outside the core region [30].

The pseudopotential approximation views the system as a sea of valence electrons moving in a background of fixed, positively charged ions. To do this, one first plots the L=0 wavefunction of the atom of interest. At a radius just beyond the outermost node of this wavefunction, a cutoff radius, r_c, is chosen. Inside r_c a smooth curve is drawn from the $\Psi(r_c)$ through the origin. This removes the nodes from the core region of the wavefunction and leaves it untouched for $r > r_c$. If the chosen r_c is too small, the pseudopotential is too hard and convergence and computational efficiency are compromised. If the chosen r_c is too large, the corresponding pseudowaveunction will have poor transferability. That is, for a given electronic configuration, the energy calculated with the pseudowavefunction and true wavefunction should be the same. For good plane wave DFT calculations then, a good pseudopotential is required and should be tested for transferability before it is used.

1.3.6 Dispersion

One strength of second order perturbation theory is that it inherently includes dispersion interactions between two closed shell molecules whereas Hartree Fock and DFT theories do not. In most GGA DFT calculations, it is well known that for weakly interacting systems, long range electron correlations that describe dispersion van der Waals forces are not accounted for [27]. Van der Waals forces are often seen as the attractive portion of the Lennard-Jones potential

$$u(R) = 4\epsilon[(\frac{\sigma}{R})^{12} - (\frac{\sigma}{R})^{6}] \tag{1.83}$$

Also known as the induced dipole moment, the Lennard-Jones potential gives a binding energy between two inert closed shell atoms of around $0.2eV$ [30]. Including a corrective van der Waals disspersion energy of the form of $C_6 \cdot R^{-6}$ to DFT calculations, known as DFT-D3, has been shown to give results that agree well with experimental values for weakly interacting systems [9, 36, 27, 13, 33].

The total energy of a DFT-D3 calculation is given by

$$E_{DFT-D3} = E_{KS-DFT} + E_{disp} \tag{1.84}$$

With

$$E_{disp} = -s_6 \sum_{i=1}^{N-1} \sum_{j=i+1}^{N} \frac{C_6^{ij}}{R_{ij}^6} f_{dmp}(R_{ij}) \tag{1.85}$$

Where the atoms are indexed $i, j, ..., N$, and R_{ij}^6 is the interatomic distance for a given atom pair. The global scaling factor, s_6, depends on the functional used. The dispersion coefficient for each unique atom pair is given by

$$C_6^{ij} = \sqrt{C_6^i C_6^j} \tag{1.86}$$

Where the individual C_6 and R_0 parameters can be found in the literature [27]. In order to avoid near-singularities at small radii, a damping function is introduced

$$f_{dmp}(R_{ij}) = \frac{1}{1 + e^{-d(R_{ij}/R_r - 1)}} \tag{1.87}$$

Where R_r is the sum of atomic van der Waals radii [27]. Although E_{disp} is simply added on to the KS-DFT energy, the functional dependence of the global scaling term S_6 requires the same functional be used in both calculations for Equation 1.74 to be valid.

1.3.7 Geometry Optimization Methods

The total energy discussed up to this point corresponds to a single molecular geometry. Setting derivatives of the total energy with respect to the nuclear coordinates to zero locates a stationary point on the molecules potential energy surface (PES). Second derivatives of the energy with respect to the nuclear coordinates enable the classification of the located stationary points. In other words, minimizing the molecular energy with respect to the nuclear coordinates leads to equilibrium molecular structures, second derivatives of which will classify these. Optimized structures are classified by stationary points on the potential energy surface (PES) defined by the molecule. A PES is a graphical representation of the system's energy with respect to the orientation in space of the individual atoms in the

structure. For a structure with N atoms, the corresponding PES has 3N+1 dimensions.

To simplify the PES to a plottable form, the coordinates are reduced to simple reaction coordinates (when taken together together still describe a specific molecular structure) and the molecular energy on the PES is plotted in the Z-direction. The PES contains maxima, minima, and saddle points. The minima correspond to stabile equlibrium structures of the system, and the maxima are transition states connecting equilibrium stuctures. A saddle point is one in which moving along one of the structural variables is a maxima, while along the other is a minima. Saddle points also indicate transition state structures. To optimize structures, we therefore minimize the energy with respect to the PES coordinates. During such a geometry optimization, the energy and gradient of the energy is first calculated from the starting structure. As the gradient points in the direction of quickest descent, this helps the algorithm update the geometry equivalent to moving along the PES. Most optimization algorithms also include second derivatives of the coordinates to get information about the curvature, updating the Hessian matrix of force constants and dictating the next step size and direction to move along the PES.

When the sum of the forces acting on the atoms in the structure, the root mean square of these forces, the calculated displacement of the next step to take, and the root mean square of this displacement all approach predefined values close to zero, a stationary point on the PES is located. This procedure does not always locate a minima, but sometimes converges to another extremum on the PES. For this reason, geometry optimizations are usually followed by frequency calculations (Hessian) that calculate vibrational normal modes and corresponding frequencies that can be used to classify the nature of the located extrema [26].

1.3.8 Vibrational Frequency Calculations

Second derivatives of molecular energy with respect to the obtained nuclear coordinates during geometry optimizations are used to classify stationary points as a true minimum or saddle point with one or more maxima, and to predict vibrational frequencies and intensities of raman and IR spectra [26]. Approximate matrices of these second derivatives, Hessian matricies, are already calculated in geometry optimizations to determine the direction and size of the next step on the PES to take so frequency calculations are often included to follow geometry optimizations, but can also be computed more accurately, using a set of previously optimized coordinates. It is important however, that the same theoretical model and basis set be used in a frequency calculation that was used in the geometry optimization. From the resulting vibrational frequencies, one can also correct final energies by adding the zero point energy to the total energy although this contribution is often small.

1.3.9 Basis Sets

As discussed briefly in section 1.3.1 we will be using linear combinations of predefined primitive gaussian type basis functions as our basis set given by Equation 1.9. It may be important to note that the molecular orbitals, ϕ_i, we have constructed are purely out of mathematical convenience and cannot be physically observed. As discussed previously, there are ways to perform unitary transformation on the canonical orbitals to make them more localized and perhaps provide a more intuitive chemical bonding picture. One can also use different sets of orbitals and coefficients that equivalently give Löwdin orbitals that are eigenvectors of the reduced one-particle density matrix or even natural bond orbitals that have been constrained to find molecular orbitals that resemble those in a Lewis structure [26].

Specifying a basis set can be thought of as restricting the electrons in the system to a particular region of space. A larger basis set poses fewer constraints and can therefore produce more accurate wavefunctions, but at a higher computational cost. It is therefore often desirable to chose the biggest possible basis set that is still computationally practical.

There are also computational methods that allow one to use larger and larger basis sets until the energy is converged to a value at an infinite number of basis functions known as the basis set limit [26].

A minimal basis has the fewest number of functions required to describe each atom. This often includes the lowest unoccupied orbital. The STO-3G basis set is a minimal basis set that represents each orbital in the atom as a Slater type orbital composed of three primitive gaussian functions per basis function. Using minimal basis sets is not sufficient in most cases as the atoms in the molecular structure would have their electron probability distributions significantly different than what they would be in the isolated atoms. By introducing multiple functions with different exponential, or zeta values, is the first way to improve the results.

A simple split valence basis set, 3-21G, is a double zeta basis set that represents each core orbital with a basis function composed of three primitive gaussians. This is a double zeta basis set as each valence orbital is represented by two basis functions composed of two and one primitive gaussians respectively. A more common double zeta basis set 6-31G, has six primitive gaussians per core orbital basis function, and two basis functions per valence orbital composed of three and one primitive gaussians respectively. A triple zeta basis set then, 6-311G, also has six primitive gaussians per core orbital basis function, but three basis functions per valence orbital composed of three, one, and one primitive gaussians respectively.

In addition to split valence basis functions, polarization and diffuse functions are often included to improve results. Split valence basis sets allow orbitals to change size, but not shape. Polarization functions are then added to accomplish this. Taking our 6-31G basis set and adding d functions to the heavy atoms gives the 6-31G(d)/6-31G* basis set or adding a second polarization function, a p function to the hydrogen atoms, is represented 6-31G(d,p)/6-31G**. Diffuse functions are larger-scaled versions of s- and p-type functions allowing the the oribitals to occupy a larger region of space. Basis sets with diffuse functions are important in systems where electrons are relatively far from the nucleus. A 6-31+G* is then the 6-31G* bass set with diffuse functions added to the heavy atoms. Going a

step further, 6-31++G* adds diffuse functions to the hydrogen atoms as well, but does not usually produce results significantly different from those at the 6-31+G* level. This way of defining basis sets can be continued to include quadruple zeta, etc. basis sets. Typically the 6-311+G** basis set is a sufficient compromise between accuracy and efficiency. It is convenient to represent the relationship of computational method and basis set size in terms of overall accuracy in a Pople diagram (see Figure 1.2).

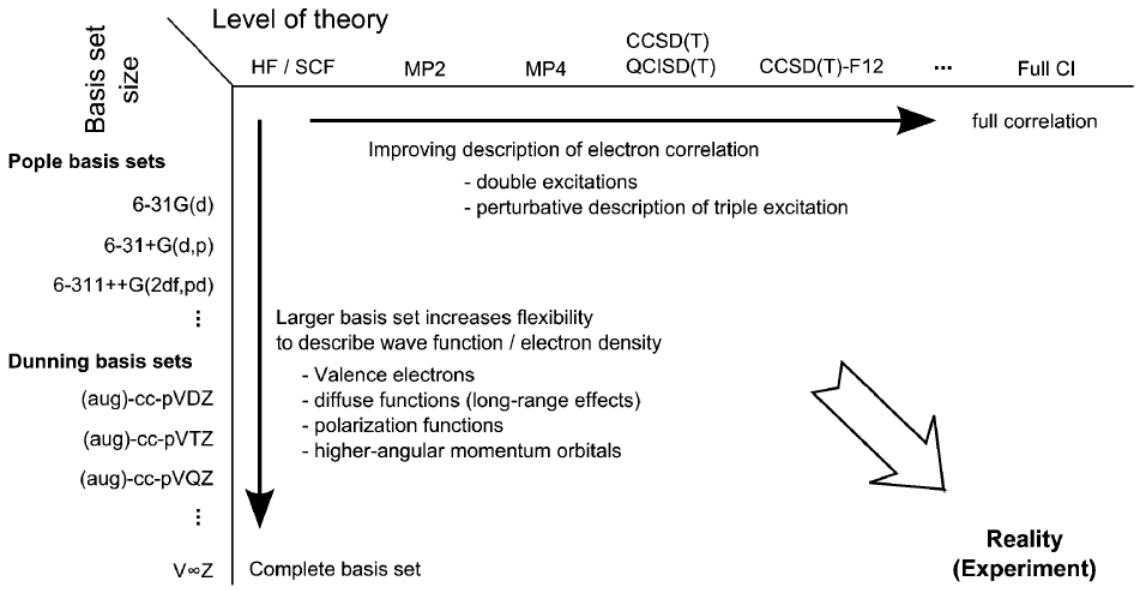

Figure 1.2: Pople Diagram showing the relationship between basis set size and level of post Hartree Fock theory. Approaching the limit of true ground state wavefunction corresponding to the exact energy comes increases required computing power.[47]
Source : *Vereecken and Francisco Chem. Soc. Rev.*(2012), 41, 6259 − 6293

Figure 1.2 provides a visual representation of the overall accuracy of post Hartree Fock correlation methods and basis set size with respect to computing cost. A similar way of organizing DFT functionals in terms of deviations from an exact exchange correlation functional can be visualized in a Jacob's ladder diagram[43].

The use of linear combinations of primitive contracted gaussian functions as a basis of slater type atomic orbitals provide an analytical solution to the Kohn Sham equations. This method works well for small clusters but becomes computationally expensive in linear-scaling DFT programs such as SIESTA and can lack systematic convergence when higher order split valence basis sets are used. To speed things up and improve scalability, SIESTA

uses numerical atomic orbitals that are optimized variationally, using a single variational parameter [7].

In this method, numerical solutions to the Kohn-Sham Hamiltonian for the isolated pseudoatoms defined by the same pseudopotentials as for the entire system as a whole. This is done on a logarithmic grid using the Numerov method, which is a differential technique for equations of second order where the first-order term is not known. To generate split-valence basis sets under this method, once the single zeta wavefunction is calculated, a cutoff radius is chosen, outside of which the double and single-zeta functions are identical. The double zeta function is then continued as $r^l(a_l - b_l r^2)$ towards the origin before its difference with the original function is taken. The resulting cutoff radius is then smaller (more efficient) and the new split-valence function is then normalized and is also orthogonal to the lower order orbital [6]. Polarization functions can then be added by perturbative polarization with the use of a small electric field, or by solving the Schrödinger equation for higher angular momentum in the unbound free atom. Single valence basis sets in this method are much more efficient than the higher order split-valence sets, but the cutoff radius cn be specified to improve efficiency.

1.4 Software Packages

1.4.1 GAMESS

The majority of the calculations for this thesis were executed with GAMESS (general atomic and molecular electronic structure system) and all graphics from GAMESS calculations prepared with MacMolPlot[14, 21].

1.4.2 SIESTA

For all SLAB calculations, the ab initio DFT package SIESTA (Spanish initiative for electronic simulations with thousands of atoms) was used and all corresponding figures prepared with XCrySDen (X-window crystalline structures and densities)[7, 6].

1.5 Outline of Thesis

This project began as a simple DFT investigation of atomic adsorption using an assortment of different functionals and basis sets to see which best describe both the chemically adsorbed and physisorbed states atop a carbon atom of a various sizes of PAHs. It was discovered that many of these DFT functionals, especially when dispersion corrections were included, overestimated the physisorption interaction. The results of these preliminary calculations allowed the development of a suitable DFT functional, basis set, and PAH combination that would produce results comparable to literature values.

Once a reliable computational method was developed for H_2, in chapter 2 of this thesis, a series of small molecules N_2, CO, NO, CN, CH_4, NH_3, and H_2O are chosen to be adsorbates and their geometries are first optimized in GAMESS. In this cluster approach, the structure of coronene, $C_{24}H_{12}$ is optimized using the same computational method as the above small molecule adsorbates. Using coronene as the substrate, the adsorption energies of the small molecules are calculated and reported. To represent graphene in the slab approach using SIESTA, a triangular unit cell containing 32 carbon atoms was then prepared and optimized using similar functionals and basis set size as used in the GAMESS cluster calculations. The physisorption energies of these small molecules using the SLAB approach using SIESTA are reported alongside those calculated with GAMESS in the cluster approach. The two computational methods are compared using the literature H_2 binding energies as our known value.

In the final section of this thesis, a series of light alkali adatoms including Li, Na and halogens F, Cl in all diatomic and alkyl halide configurations are first adsorbed to graphene. Molecular H_2 is then adsorbed to the system and its physisorption energy was calculated and compared to that before the adition of the adatom/adsorbed alkyl halide. The final results are analyzed and tabulated. The results of this section are prepared to compare the differences in H_2 binding energy before and after the addition of a small atom or molecule to the system. The overall goal is to increase the physisorption energy of H_2 on graphene. Such results in a lightweight carbon system could provide insight into new mehodologies of storing H_2 in the solid state for potential fuel cell storage systems.

Chapter 2

Adsorption of small molecules on graphene

2.1 Introduction

The current investigation is motivated by hydrogen storage applications, but the interaction of hydrogen and graphitic surfaces is of a fundamental nature with widespread applications from the recombination of H_2 from atomic hydrogen in the interstellar medium [42, 4] to the reversible storage of hydrogen for delivery to fuel cells [44, 5, 19]. The simple interaction of a hydrogen atom or molecule on a graphitic surface can be difficult to model accurately due to the weakly bound physisorbed state described by van der Waals forces[33]. In this section small molecules are adsorbed onto graphitic surfaces and their corresponding binding energies, or adsorption enthalpies are calculated.

It is convenient to start with the simplest of molecules, H_2, as we are primarily concerned with the binding energy of molecular hydrogen on graphitic surfaces in this thesis. It has been shown that atomic hydrogen can also physisorb to graphitic surfaces in addition to its ability to chemically bind to one of the constituent carbon atoms. The C-H bond characteristic of this chemisorbed state has a much higher activation energy barrier, corresponding

to binding energies of 200-300 kJ/mol [31, 28]. This is due to the necessary relaxation in the carbon framework as the specific carbon atom binding with hydrogen is rehybridized from sp^2 to sp^3 so that it can then form a covalent bond with the hydrogen atom. Once this exothermic process begins, each subsequent chemisorption reaction becomes more favorable as the conjugated π-system is broken and often results in a fully reduced substrate, which often requires catalysis to release the hydrogen to be used as a fuel source, as in the spillover mechanism as outlined in section 1.2.2 [19].

2.1.1 H atom adsorption on Graphene

Although we are not presently concerned with atomic hydrogen or chemisorption, preliminary calculations were performed on atomic hydrogen atop a central carbon atom, which we will call C1, in Pyrene, $C_{16}H_{10}$ (see Figures 2.1, and 2.2). In a cluster approach using DFT with GAMESS, an initial guess at the pyrene structure was fully optimized an unrestricted SCF procedure with as a doublet. This corresponds to a spin multiplicity of 2 from 2S+1 where S is the spin associated with unpaired electrons. The hybrid B3LYP functional and a 6-31G* basis set were used for the optimization and vibrational frequencies were calculated to verify that the optimized structure was a local minimum as well as to get more accurate total energy corrected by the zero-point energy, ZPE. Once the planar starting structure was located, a hydrogen atom was placed at 0.7 Å above the C1 carbon of pyrene and its energy was calculated to give the bound complex energy E_B. The difference from the bound energy and the individual unbound energies, E_U, which in this case would be the sum of the mutually isolated pyrene and hydrogen atom energies, gives the binding energy B_E

$$B_E = E_B - E_U \tag{2.1}$$

The hydrogen atom was then raised in the Z-direction 0.1 Å , keeping pyrene planar, and the energy calculated again. These sequential single point energy calculations were performed until a near zero or positive binding energy was calculated, or at around 5 Å (see Figure 2.1). The physisorption energies, or PSEs, are equivalent to B_E obtained via Equation 2.1 in our calculations.

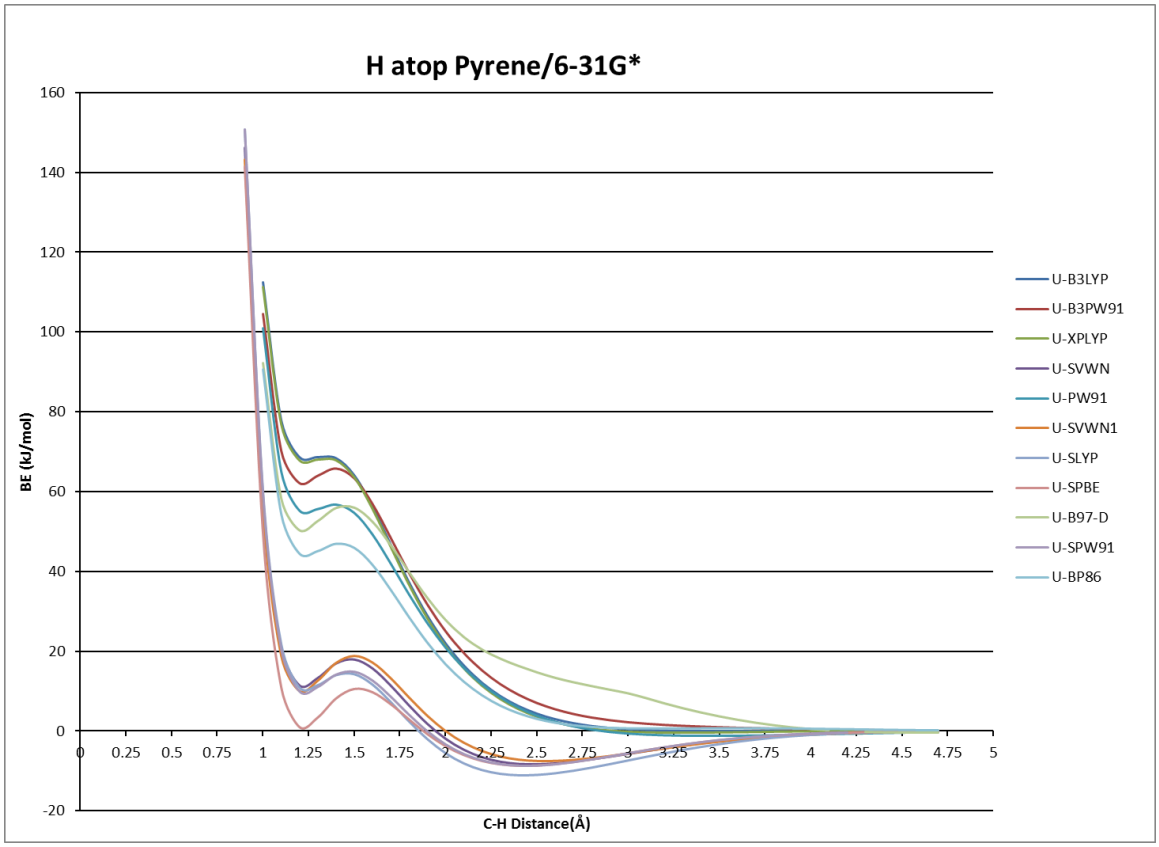

Figure 2.1: Atomic hydrogen adsorption on pyrene:
This figure shows binding energy curves of a single hydrogen atom atop a central carbon atom C1 in planar pyrene. Prepared via a series of single point energy calculations, 11 DFT functionals are compared at the 6-31G* basis set level.

Figure 2.1 explores the H-pyrene cluster with a 6-31G* basis set using a variety of different DFT functionals. Two minima can be seen in roughly half of the functionals used. The closer of these two minima, occurring at a hydrogen height of about 1.25 Å , is a chemisorption interaction represented by a tranfer of charge between the hydrogen atom and carbon substrate. The outer minima occuring at roughly 2.5 Å is the physisorption well and unlike the chemisorption well is not site specific and there is no clear charge transfer. The broad shallow shape of the physisorption region of the binding energy curve results in the non site specific interaction observed. It is this type of interaction that we are interested in as it does not alter the carbon framework of the substrate. This figure was inspired by L. Jeloaica and V. Sidis who in their 1999 publication in Chemical Physics Letters [31] who used a similar DFT approach to first show the existence of this outer physisorption well for atomic hydrogen. These preliminary calculations were used to determine which DFT functionals

can accurately describe the physisorption interaction. From Figure 2.1, we see that only the functionals that include a slater exchange component, show the broad outer minima associated with physisorption. Of the DFT methods investigated, three seem to give the best representation of the PSE region: SPBE, SVWN1, and SPW91. The combination of a Slater exchange and Perdew/Wang 1991 pure GGA functional, SPW91, was initially chosen to give a good visual representation of the physisorption interaction using a series of single point energies atop a rigid planar PAH substrate. Although we are not largely concerned with the inner chemisorption well, a few results are noted. The interesting inner minimum corresponds to a positive binding energy. This suggests a metastable chemisorbed state. This is because of the planar PAH substrate. If the hydrogen atom is placed at a height near this minimum of 1.25 Å followed by a full geometry optimization, the PAH would no longer remain planar and the carbon directly beneath the hydrogen atom would relax as it went from sp^2 to sp^3 configuration. The corresponding binding curve would indeed show a more pronounced minimum with a negative binding energy on the order of 200-300 kJ/mol as would be associated with a typical chemisorption interaction. This was done using the SPW91 functional and can be seen in Figure 2.2

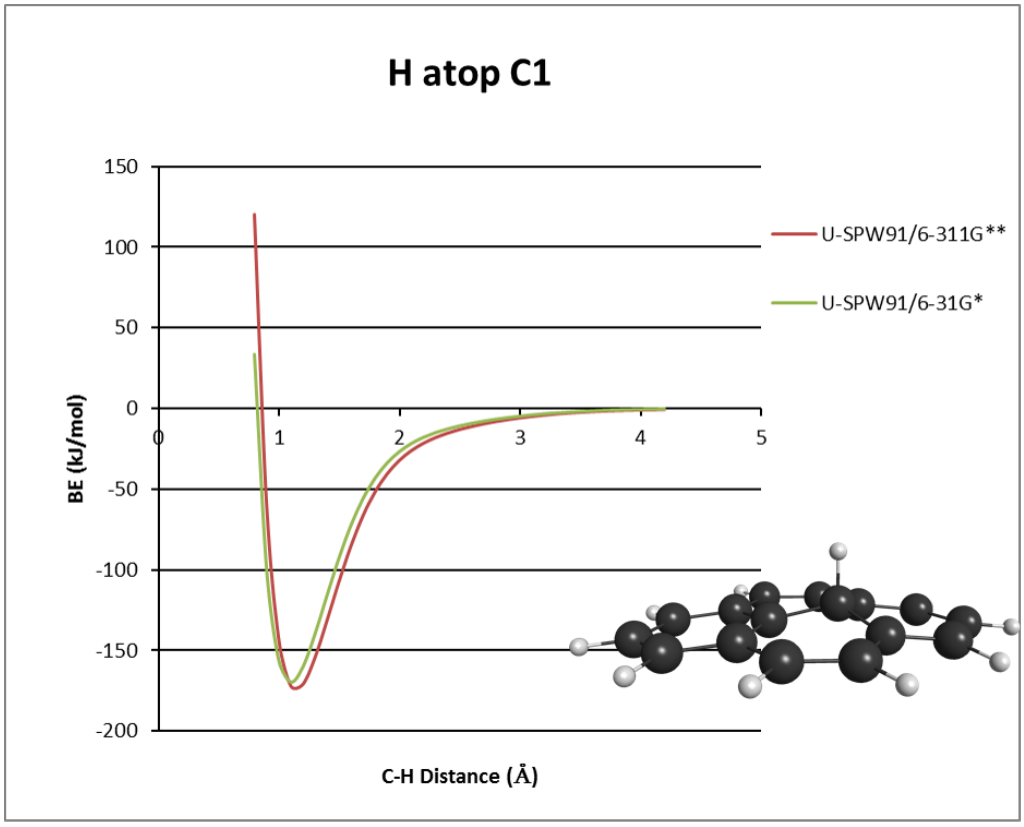

Figure 2.2: Chemisorption of Atomic hydrogen on Pyrene:
This figure shows the adsorption energy of a hydrogen atom atop a central carbon atom in Pyrene using 6-31G* and 6-311G** basis sets.

Figure 2.2 was prepared with the same 6-31G* planar pyrene structure as in Section 2.1.1 and a hydrogen atom was again placed at 0.7 Å . The resulting cluster underwent a full geometry optimization using the same method and basis set. The initial planar Pyrene structure had an average C-C bond length of 1.406 Å . After the geometry optimization the average C-C distance did not change, but C1 relaxed to a height of 0.46 Å above the plane of the original pyrene. This can be seen in the structure within Figure 2.2 as the C1 is seen as the maxima of a slightly convex pyrene structure forming a 1.1Å bond with the hydrogen atom. From the relaxed structure, a series of single point energy calculations were performed, starting at 0.7 Å in increments of 0.1 Å until the binding energy converged to zero around 4.5 Å . The binding energy was calculated using Equation 2.1 at each step and plotted against the distance between the relaxed pyrene molecule and hydrogen atom. Figure 2.2 shows minima at 1.1 Å with corresponding binding energy of -172 kJ/mol with

the 6-311G** basis set. This is within the range of a chemisorbed interaction. Relaxations of the substrate during all adsorption processes are relevant and so we include these results here for comparison. Typical C-H bond dissociation energies range from 300-400 kJ/mol, so this interaction is weaker than a typical covalent C-H bond. The optimal range of binding energies for hydrogen storage are between that of physisorption and chemisorption at 7 to 77 kJ/mol [28].

2.1.2 H_2 Adsorption on Graphene

We now move onto a purely physisorption investigation where H_2 is adsorbed onto PAHs in our cluster approximation to a full graphene sheet. It is well documented that PAHs are reasonable limits to their infinite counterparts [9, 42, 13]. There is still some variation in the results with respect to PAH size. We should expect, that with a larger PAH comes more accuracy, but at a higher computational cost. To convince ourselves we are using a sufficiently large PAH, we explore a few different options. The polycyclic aromatic hydrocarbons (PAHs) $C_{16}H_{10}$ (pyrene), $C_{24}H_{12}$ (coronene), and $C_{54}H_{18}$ (circumcoronene) are used as model systems for graphene and their B3LYP/6-311G** optimized structures and average C-C bond lengths are

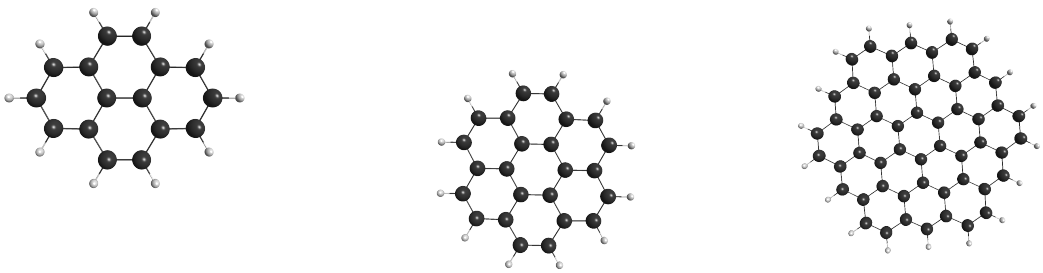

Pyrene $C_{16}H_{10}$ (a) 1.407±0.025 Å

coronene $C_{24}H_{12}$ (b) 1.410±0.022 Å

Circumcoronene $C_{24}H_{18}$ (c) 1.414±0.022 Å

Figure 2.3: Fully Optimized PAH Substrates:
The structures shown above have been optimized using DFT at the B3LYP/6-311G** level. Coordinates of final structures calculated with GAMESS can be found in Appendix A.

The expected C-C bond length in Benzene is 1.40 Å and in bulk graphite and graphene is slightly larger than 1.42 Å . In coronene the outer C-C distances are larger than these in the

central ring, resulting in an expected average bond length of 1.42 Å [42]. B3LYP/6-311G** calculations give average C-C bond length of benzene (not shown) to be 1.394 Å , in pyrene to be 1.407 Å , in coronene to be 1.410 Å , and in circumcoronene to be 1.414 Å . This is consistent with the expected values. It can be observed that the more outer rings the PAH has, the larger the average C-C bond length, approaching the expected 1.42 Å for a full graphene sheet. At the MP2/6-311G** level the average bond length in coronene is 1.411 Å . Both of these methods give reasonable bond lengths in our PAH substrates. Standard deviations are included in the above structures as a measurement of relaxation during optimizations. For instance, during the geometry of the H-pyrene cluster, the average C-C distance did not significantly change, but the standard deviation increased from 0.022 Å to 0.038 Å in the relaxed pyrene structure.

As we wish to test our PAH's for accuracy in representing a full graphene sheet, we choose one functional, SPW91 for visual clarity or the binding curves, and test each of the PAH's in Figure 2.3 at two different basis set sizes, 6-31G* and 6-311G**. Physisorption energies are calculated using DFT with the SPW91 functional, holding the PAH substrate planar, and performing a series of single-point energy calculations, and taking the difference in energy from the sum of the free constituents, as was done to prepare Figure 2.1.

Figure 2.4 was prepared with planar optimized PAHs, with an H_2 molecule positioned 1.0 Å atop the center of the PAH. A single point energy calculation to give E_B in Equation 2.1 was performed sequentially as the H_2 molecule was raised in 0.1 Å steps. This process produces one binding curve. For each curve, the same basis set and functional was used for all corresponding calculations. The legend in the lower right shows the adsorbing height and binding energy minima of the 6-311G** curves in the figure. These binding energies are reported as they are slightly bigger in magnitude than the 6-31G* binding energies, as we expect as the size of the basis set is increased. Figure 2.4 immediately shows that there is a larger dependence of the physisorbed binding energy on the basis set than on the substrate size. This is especially true when comparing the binding curves for the coronene and circumcoronene PAHs. For pyrene, both basis sets used show a larger corresponding H_2 adsorbing height and more deviation in the binding energies. For both the adsorbate height and corresponding binding energy, these results confirm that coronene is a reasonable

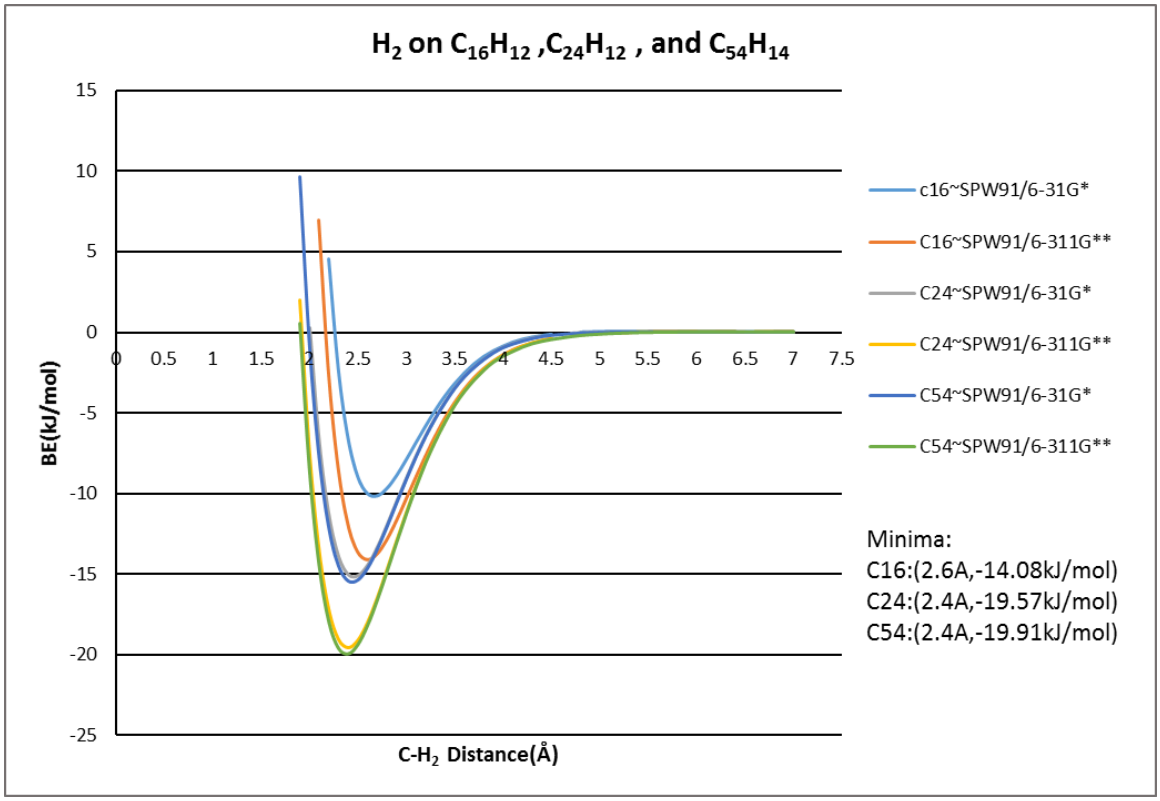

Figure 2.4: Physisorption Energies for H_2 on different sized PAHs:
This figure shows the physisorption binding curve of molecular hydrogen atop three different planar PAH substrates using 6-31G* and 6-311G** basis sets for each PAH. Distances are to the center of mass of the H_2 molecule.

approximation for a full graphene sheet. Coronene and circumcoronene at the 6-311G** basis set both give similar results. This is great news in terms of computational efficiency as increasing our basis set from the double zeta 6-31G* to the triple zeta 6-311G** is much less expensive than adding an additional 206 electrons to the system when comparing coronene to circumcoronene. The above preliminary results are used to further develop the computational procedure needed to accurately model new graphene based systems and physisorption of molecular hydrogen.

2.2 Molecular hydrogen and Graphene

In this section we examine in more detail H_2 adsorption on the graphene surface. To do this, two approaches are used: (i) the cluster model where graphene is approximated with coronene and adsorption energies are calculated using GAMESS; and (ii) the periodic SLAB model using a hexagonal unit cell with $\alpha = \beta = 90°\gamma = 120°$ and 32 carbon atoms is constructed and adsorption energies calculatedusing SIESTA. Resulting H_2 physisorption energies PSEs are tabulated and compared to literature values.

2.2.1 GAMESS: A Cluster Approach

In this section, coronene is used as our model system to represent graphene. We first ran a full geometry optimization on this substrate using DFT and B3LYP/6-311G** holding all atoms at a fixed height in the same plane. Vibrational frequencies were then calculated to verify that the optimized structure was a local minimum as well as correct total energy by the ZPE. Then an individual hydrogen molecule was fully optimized using the same procedure. The two optimized structures were then placed together at a distance of 2.0 Å followed by a full geometry optimization of the resulting cluster.

From the optimized cluster, the structure is broken back up into the adsorbate and substrate, and single point energies of each are calculated. The binding energy is then calculated by the simple difference given by equation 2.1. As it has been mentioned, to accurately represent physisorption interactions in DFT calculations, inclusion of Grimme's empirical dispersion correction involving scaled R^{-6} terms is needed [35, 27, 13]. Inclusion of this contribution to the total energy is indicated by the "-D" suffix on the corresponding functional. Second-order Möller-Plesset Perturbation theory, MP2 inherently includes dispersion terms, and the additive Grimme emperical dispersion term is not needed when performing MP2 calculations. It has been shown that MP2 and coupled-cluster calculations give accurate physisortion energies [9] but are more computationally expensive than DFT calculations.

A comparison of MP2 and DFT results

To begin we present the following H_2 physisorption energies

Table 2.1: Physisorption Energies of H_2

GAMESS Results				
Substrate	Functional	Basis Set	Height Å	PSE kJ/mol
coronene	B3LYP	6-31G*	10.00	0.01
coronene	PBE	6-31G*	3.39	-1.0
coronene	PBE-D	6-31G*	3.02	-6.4
coronene	B3LYP-D	6-31G*	2.91	-5.8
coronene	B3LYP-D	6-311G**	3.02	-6.2
coronene	B3LYP-D	6-311G(2d,p)+	3.02	-6.1
coronene	PBE	6-311G(2d,p)+	3.38	-1.5
coronene	PBE-D	6-311G(2d,p)+	3.00	-6.9
Pyrene	SPW91	6-311G**	2.61	-14.1
coronene	SPW91	6-311G**	2.44	-19.6
Circumcoronene	SPW91	6-311G**	2.53	-20.0
$N - C_{23}H_{12}$	U-SPW91	6-311G**	2.40	-20.0
$B - C_{23}H_{12}$	U-SPW91	6-311G**	2.40	-18.3
coronene	MP2	6-31G*	3.18	-1.3
coronene	MP2	6-311G**	3.04	-3.7
coronene	MP2	6-311G(2d,p)+	3.21	-6.1

Table 2.1 shows the binding energies of H_2 physisorbed onto coronene and other PAHs along with the height or the adsorbate in the optimized cluster. Various methods and basis sets are compared. The 6-311G(2d,p)+ basis set is defined here as the standard Pople 6-311G basis set with 2 d type polarization functions added on the heavy atoms and 1 p type polarization function and a diffuse s orbital added to the hydrogen atoms. Typically, diffuse shells are added to heavier atoms first and then to the hydrogen atoms. However diffuse orbitals on the heavy atoms caused linear dependencies, but we did find adding diffuse shells to hydrogen and on heavy atoms improves the accuracy of calculated H_2 PSEs. From combined theoretical and experimental results, the accepted value for H_2 adsorbed on coronene is -5.0 kJ/mol at a height of 3.29 Å above the carbon framework. [9, 42, 13]. Inspection of these results immediately bring concern to the SPW91 functional used in the preliminary calculations. It is found that the PW91 functional, overestimates

the physisorption energy of this system, even without dispersion. Other functionals, such as B3LYP, do not give H_2 binding unless dispersion corrections are included in the calculations. Dispersion corrections were not included in any of the calculations listed in Figure 2.1. The series of single point energy calculations used to prepare that curve are useful to prepare the visual potential wells, which is why the SPW91 was then chosen to prepare Figure 2.2. Still, despite SPW91 overshooting the actual energy of this system, we can still use it to address general trends. We have seen this in Figure's 2.1 and 2.3. When preparing binding curves from a series of single point energies, such functionals provide a nice visual representation of the physisorption interaction, and allow for quick comparisons between different systems. For instance, as seen from Table 2.1, heteroatom substitution in the coronene substrate to include a Nitrogen or Boron atom did increase slightly the resulting H_2 physisorption energy. This increase was not significant enough to further pursue investigation of such systems.

Comparing our H_2 adsorption energy results to the accepted value of -5.0 kJ/mol, we see that the state of the art, well tested B3LYP-D functional gives the best estimate to the H_2-coronene binding energy using both the double and triple zeta basis sets. The MP2 results are also in agreement with -6.1 kJ/mol at the triple zeta level, but the MP2 results at the double zeta level are drastically different. The reason for this is in the orientation of the adsorbate. As shown by Heine et al in 2004, the optimal orientation of H_2 atop coronene is perpendicular to the plane of the PAH, and such orientation gives MP2 binding energies at the limit of an infinitely large basis set to be around -7.2 kJ/mol. Similar calculations with H_2 oriented parallel gave binding energies of about -1.3 kJ/mol, which is exactly what happened in the above MP2 results. As full geometry optimizations are being conducted, the final geometry is determined by the potential energy surface of the cluster, and the minimum we have found may not be the global minimum, even if it is not a transition state or saddle point. When looking at the corresponding geometries to the MP2 results above, it can be seen that at the 6-31G* level, the H_2 is closer to 45°, whereas at the 6-311G(2d,p)+, it is perpendicular with respect to the plane of the substrate.

Note the differences in energy and geometry can arise when just one more polarization and diffuse function are added. In the above MP2 calculations, increasing the basis set from

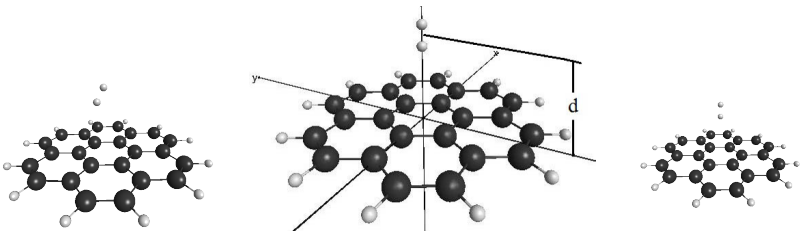

(a) B3LYP-D: B_E=−6.2kJ/mol, d=3.02$\mathring{A}$

(b) optimal H_2 orientation on coronene

(c) MP2: B_E=−3.7kJ/mol, d=3.21$\mathring{A}$

Figure 2.5: H_2 physisorbed atop the center cite of coronene at the 6-311G** level: Figure a and c shown above have been fully optimized using 6-311G** basis set. Figure b is used as a visual for the height and orientation at which H_2 physisorbs. The distance, d, is measured from coronene to the H_2 center of mass.

6-31G* to 6-311G** increased the binding energy from -1.3 to -3.7 kJ/mol. This may seem like a surprisingly large change in the binding energy and it is. The reason for this is due to a rotation of almost 90° of the adsorbed H_2 molecule. The optimal positioning as shown in Figure 2.5b is well documented [31, 9, 42, 13], but the interesting thing is how sensitive these MP2 results are to the size of the basis set used. Adding to the standard triple-zeta 6-311G** a second d-type polarization function and a diffuse S-shell to the hydrogen atoms in this system to 6-311G(2d,p)+ increases the binding energy again from -3.7 to -6.1 kJ/mol, without a drastic change in geometry.

The above MP2 results in Table 2.1 are in excellent agreement with literature values. Heine et al. reports MP2 physisorption energies of H_2 on coronene to range from -3.5 to -7.2 kJ/mol. [9] We observe similar trends in the present MP2 results. It is apparent the fickle behavior of these types of dispersion based interactions, in both the orientation of the H_2 and the sensitivity of the MP2 results on the size of the basis set.

Perhaps due to the at times large empirical correction for dispersion energies in the DFT-D_3 results, the B3LYP-D results do not appear to be as sensitive to the size of the basis set used, further supporting the use of the B3LYP functional in a variety of different chemical scenarios. When increasing the size of our basis set from 6-31G* to 6-311G** the corresponding B3LYP-D physisorption energies increased from -5.8 to -6.2 kJ/mol, as one may expect. When the basis was further increased to 6-311G(2d,p)+ however, the physisorption energy did not increase this time, but decreased slightly from -6.2 to -6.1 kJ/mol. Although

this is surprising, it is comforting for the results to not drastically change upon addition of more functions to the basis set as it suggests that the basis set used is a reasonable approximation to the true wavefunction of the system, and we need not waste any more computer time with arbitrarily large basis sets.

The results of adsorbing molecular hydrogen onto coronene in this section, albeit not profound, have allowed us to say with confidence that the B3LYP-D/6-311G** and MP2/6-311G(2d,p)+ computational methods will suit our needs to use to calculate physisorption energies of molecular hydrogen on PAH substrates.

2.2.2 SIESTA: A SLAB Model

The primitive unit cell for graphene, and graphite, contains only two atoms. To build a c8 unit cell containing 8 carbon atoms, the unit cell consisted of 2x2 primitive lattice vectors, with the carbon atoms in the corresponding Wykoff positions before the structure was optimized. The same procedure was followed to generate the c18 unit cell from 3x3 primitive lattice vectors and c32 from 4x4 primitive lattice vectors, as seen in Figure 2.6.

All periodic calculations were carried out using the ab initio DFT based package, SIESTA. Substrates were all based around graphene modeled with a single layer of 32 carbon atoms in a hexagonal unit cell. Molecular adsorbents were placed in the center of the unit cell approximately 1.5 Å above the carbon substrate. Similar to the symmetries in the coronene molecule the 32-carbon unit cell allows for adsorbates to be placed in the middle of the central ring of the molecule/unit cell. Many preliminary calculations were done to first build these unit cells.

To optimize the geometry the structures in Figure 2.6, a three step process is followed. During a full geometry optimization in SIESTA, one first allows the atomic coordinates to relax to the specified convergence criteria. Next the atomic coordinates are held fixed and the unit cell vectors are allowed to relax to the same set of convergence criteria. In the final step of the full geometry optimization, both the unit cell and the atomic coordinates are

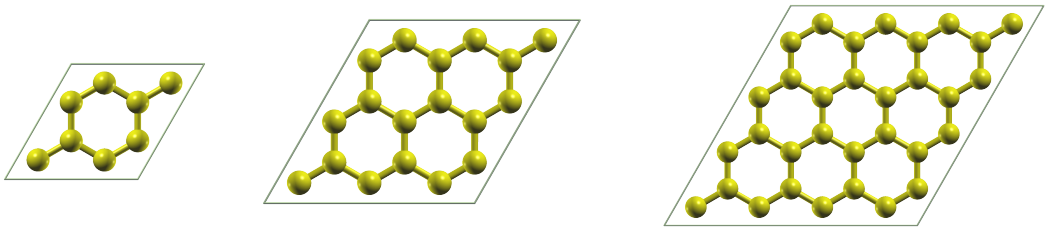

(a) -1233 (b) -2774 (c) -4931

Figure 2.6: Unit cells used in SLAB calculations containing 8,18, and 32 carbon atoms from the top view. The height of these unit cells is set arbitrarily high in the Z-direction at roughly 23 Å causing the carbon sheets to be separated by that distance and therefore not interact with each other. The total energy listed below each structure is in kJ/mol.

optimized again to the same thresholds as the previous two steps.

To calculate the energy at each step in the optimization procedure, integration over the Brillouin zone was performed over (10x10x5) k-points with a mesh cutoff of 210 Ry and a k-grid cut-off of 45 Bohr. The system was then allowed to relax until the energy was consistent within 10^{-4} eV and the force on each ion was at least less than .04 eV/Å [12]. The PBE and LYP functionals are the two most common GGA functionals used in the SIESTA code. PBE includes the standard Perdew-Burke-Ernzerhof GGA exchange-correlation funcional also available in the GAMESS package [37]. The LYP functional includes Becke's gradient exchange functional [1] along with the Lee, Yang, Par correlation functional[22]. Grimme's atomic pairwise dispersion correction term based on $C_6 \cdot R^{-6}$ is included in some calculations [27] and is indicated with a "-D" suffix on the corresponding functional. The binding energy, B_E, was then calculated using $B_E = E_B - E_U$ where E_U is the combined energies of the separate optimized carbon framework and molecular adsorbent and E_B is the final energy of the fully optimized structure including both the adsorbate and the carbon substrate.

SLAB Results

Preliminary results from SLAB calculations involved running the same calculations on different sized unit cells from Figure 2.6 to test the system for size extensivity. That is, we wanted to see if the resulting binding energies changed significantly due to the size of the

unit cell. This is similar to the preliminary cluster calculations discussed in Section 2.1. The changes in binding energies with respect to size of the unit cell in our slab calculations changed minimally. On the c8 unit cell, LYP-D/TZ2P H_2 PSE was calculated to be -36.3 kJ/mol , and on both c18 and c32 was -36.5 kJ/mol. These results make sense due to the periodicity of the model and the small size of the H_2 molecule, it only interacts with the carbon sheet and not other H_2 molecules in neighboring unit cells. In the cluster calculations, differences in substrate energies might be attributed to the number of hydrogen atoms required to terminate the carbon framework of the PAH. Because in the periodic scenario there are no terminal hydrogens, the change in energy of the substrate remains near zero as the size of unit cell increases. The observed difference in the H_2 PSEs as the unit cell was increased to contain 32 atoms from 8, is due to the H_2 molecule interacting with an H_2 in a neighboring unit cell as the system is repeated. Therefore, a sufficiently large unit cell is needed to eliminate this. For the case of H_2, c18 would suffice, as would c8. We do not plan on studying H_2 on graphene exclusively and intend to move on to more complicated systems. For this reason, as well as its similar symmetry to coronene, we will be using the c32 unit cell as shown in Figure 2.6 for the remainder of our SLAB calculations unless otherwise specified. The following H_2 physisorption energies are obtained:

Table 2.2: Physisorption energies of H_2 in a Periodic System: The calculated H_2 PSEs calulated using different functionals and two different basis sets are shown. The results of the SLAB calculations all appear to give overestimates to the accepted H_2 PSEs. Similar SLAB calulations have recently been performed by Pantha and Belbase using an 18-carbon unit cell the same as Figure 2.6b using the quantum ESPRESSO package. Binding energies of H_2 perpendicular to a hollow site of the graphene sheet to be -6.6 kJ/mol [36] which is consistent with our cluster calculations, but not the results in Table 2.2.

SIESTA Results				
Substrate	Functional	Basis Set	Height Å	PS Energy kJ/mol
c32	LYP	DZP	2.68	-15.7
c32	LYP-D	DZP	2.41	-35.8
c32	PBE	DZP	2.76	-18.4
c32	PBE-D	DZP	2.41	-40.3
c32	LYP	TZ2P	2.89	-17.7
c32	LYP-D	TZ2P	2.79	-36.5
c32	PBE	TZ2P	2.78	-20.3
c32	PBE-D	TZ2P	2.43	-40.8

2.3 Discussion: A Comparison of Cluster and SLAB calculations

The reason for discrepancy between cluster and SLAB calculations at this stage is uncertain but there are a few possibilities. The comparison of PBE-D and B3LYP-D DFT functionals in GAMESS calculations in Table 2.1 gave similar binding energies suggesting PBE-D in SIESTA would be comparable but that is not observed here. It is known that overestimated binding energies in similar systems stem from basis set superposition error (BSSE) [9, 17, 13]. BSSE is an incorrect lowering of a systems total energy resulting from the overlapping of constituent basis functions. In our present case, if basis functions from the hydrogen molecule overlap with those in the graphene sheet or coronene molecule, the basis set of the entire cluster's then larger than the sum of the basis functions in the isolated counterparts. This in turn would lower the total energy providing an artificial stabilization of the resulting dimer.

Depending on the computational method used, BSSE can be negligible [13] where as in other cases it can cause binding energies to double [9]. Typically, in the case of standard sized basis sets such as 6-311G(2d,p)+, usually results in minimal BSSE [26]. In the present case, BSSE is not likely the main cause of the overestimates in Table 2.2, or we wouldn't expect to see such a large increase in the estimated PSE as the basis set is increased from DZP to TZ2P. Applying a formal BSSE correction to these results would likely decrease the binding energies in magnitude slightly, but not to the extent to match those from the cluster calculations and excepted values[9, 42].

In our cluster calculations, BSSE was breifly addressed and minimally changed the resulting PSEs. To further investigate the presented SLAB calculations, with the intentions these results can still provide insight to this chemical system and to observe general trends we now move on to adsorb a series of selected small molecules on to graphene.

2.4 Small Molecules Adsorbed on Graphene

In order to fully address the accuracies, or lack there of, in one's computational method, it often advised to chose a standard set of molecules, and run the same calculations with multiple basis sets [40]. Up to this point DFT methods for H_2 on coronene give reasonable PSEs. Despite over-estimated binding energies in the previous section, we evaluate if the SLAB calculations give the same general trends as obtained from the cluster calculations can still be observed. As always, to our aid we will keep the trusty and efficient B3LYP-D DFT cluster method to compare results.

A standard hierarchy of basis sets typically consists of STO-3G, 6-31G*, and 6-31G** is fairly primitive, STO-3G being minimal and the others are not much larger. With available computational power, the largest basis set possible is often used. For our purposes, as we have found in our investigation of H_2 adsorption on graphene, the 6-31G*, 6-311G**, and 6-311G(2d,p)+ (similar to DZP, TZP, TZ2P in SIESTA) basis sets to suit our computational needs, and we continue to use these as our standard basis sets in the following sections.

2.4.1 A Selection of Small Molecules

In this section, adsorption energies of N_2, HF, NO, NH_3, H_2O, CH_4, CO, and H_2 are calculated. This is a standard set of small molecules [40] to which we will also include CN for the following reason: The overall goal of this thesis is to find a way to increase H_2 PSE on graphene without provoking a chemically bound state for H_2 as that observed in chemisorptive storage. Increasing H_2 PSE to a range up to -100 kJ/mol is desired for applications to a solid state hydrogen storage device. We are currently interested in light metals and/or halogen compounds to add to our system and observe their effect on H_2 PSE. As CN compounds are known to behave similarly to Halogens in certain cases due to it's high polarity and electronegativity, we include it in our standard set of molecules:

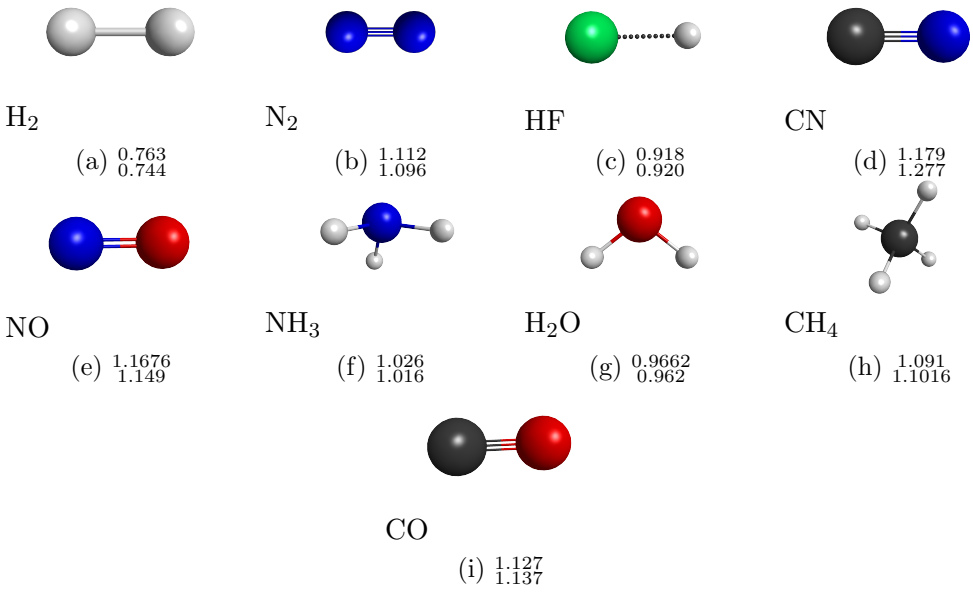

Figure 2.7: The selection of small molecules and their equilibrium bond lengths in units of Angstroms calculated using both SIESTA (upper value) and GAMESS (lower value).

The nine small molecules in Figure 2.7 were optimized in SIESTA using the 32-carbon atom unit cell with the carbon atoms removed calculatd with the LYP functional and TZ2P basis set. In GAMESS the nine small molecules were optimized using the B3LYP functional and 6-311G** basis set. Here, we see the cluster and SLAB results give comparable bond lengths. In the next section, we now adsorb this selection of molecules to graphene.

2.4.2 Small Molecule Adsorption with SLAB Calculations

We begin our exploration of small molecule physisorption in SLAB calculations with functionals PBE and LYP, both with and without dispersion, and with DZP and TZ2P basis sets. To calculate the PSEs below, the optimized 32-carbon hexagonal unit cell was used. To optimize each small molecule separately, starting coordinates were placed in the center of the unit cell and the carbon atoms removed. Then the small molecules' geometries were fully optimized in the three step SLAB optimization procedure described in section 2.2.2. The optimized 32-carbon atoms were then put back into the unit cell and the small

molecule translated to a height where the lowest atom was about 2 Å above the center of unit cell. It is important in calculations such as these to have a sufficiently large unit cell for a few reasons. The first is, in the Z-direction, this distance must be arbitrarily large so that the graphene sheet is not interacting with an identical neighbor above and below upon repetition of the unit cell. The height in the Z-direction of all unit cells used in our SLAB calculations is at least 20 Å. Similarly, to adsorb a small molecule to the surface of the graphene sheet, the distance in the X,Y directions must be large enough to where the molecule does not feel it's neighbor upon translation of the unit cell into all space. Bulk calculations of solids in periodic systems are very efficient because the primitive unit cell only requires a few atoms to fill all space due to the periodicity. SLAB calculations become increasingly computationally expensive with the size of the unit cell, as cell must be filled with more plane-wave Bloch functions or pseudo atomic orbitals, which then must be all be integrated. Therefore, even when there are no atoms present, SLAB calculations are intrinsically time consuming, especially when using larger basis sets, such as the triple-zeta TZ2P basis set.

The remainder of this chapter is summarized: Tables 2.3 and 2.4 show small molecule adsorption energies and optimized heights above graphene obtained using DZP, and TZ2P basis sets and PBE, PBE-D, LYP, LYP-D functionals in SIESTA. Tables 2.5 and 2.6 shows similar data as 2.3 and 2.4, using 6-31G*, and 6-31G(2d,p)* basis sets with PBE, PBE-D, B3LYP, and B3LYP-D functionals. The bar charts in Figures 2.8-2.11 follow each table and were prepared from the same data to give a graphical representation of the PSE variation for the different functionals.

Table 2.3: Small molecule adsorption energies and optimized height above graphene sheet calculated using SIESTA and a DZP basis set.

DZP SIESTA Results			
Adsorbate	Functional	Height Å	PSE kJ/mol
H_2	PBE	2.76	-18.4
H_2	PBE-D	2.41	-40.3
H_2	LYP	2.68	-15.7
H_2	LYP-D	2.41	-35.8
N_2	PBE	2.83	-33.1
N_2	PBE-D	2.71	-74.7
N_2	LYP	2.85	-27.0
N_2	LYP-D	2.74	-66.4
HF	PBE	2.50	-33.9
HF	PBE-D	2.48	-68.2
HF	LYP	2.54	-30.3
HF	LYP-D	2.49	-63.8
CN	PBE	2.76	-65.0
CN	PBE-D	2.82	-92.0
CN	LYP	2.85	-68.9
CN	LYP-D	2.84	-96.9
NO	PBE	2.40	-45.9
NO	PBE-D	2.35	-93.5
NO	LYP	2.59	-33.3
NO	LYP-D	2.53	-76.0
NH_3	PBE	3.08	-34.6
NH_3	PBE-D	2.82	-72.2
NH_3	LYP	3.13	-27.8
NH_3	B3LYP-D	2.84	-64.9
H_2O	PBE	2.96	-30.9
H_2O	PBE-D	3.10	-62.4
H_2O	LYP	3.05	-27.5
H_2O	LYP-D	3.14	-57.1
CH_4	PBE	3.43	-23.1
CH_4	PBE-D	3.28	-25.2
CH_4	LYP	3.83	-19.0
CH_4	LYP-D	3.44	-24.3
CO	PBE	3.06	-46.5
CO	PBE-D	2.72	-68.7
CO	LYP	3.08	-31.6
CO	LYP-D	3.03	-48.2

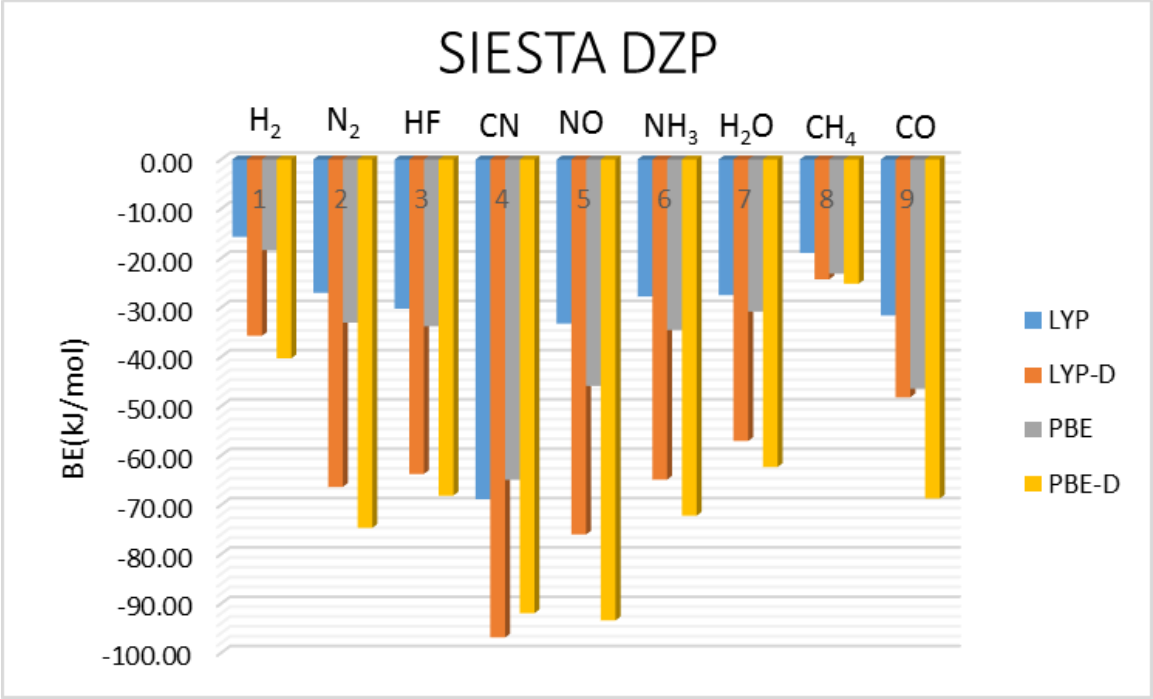

Figure 2.8: Small molecule adsorption energies with respect to SIESTA functional at the DZP basis set level.

Figure 2.8, as with Table 2.3, shows the Physisorption Energies of our selection of small molecules on the 32-carbon unit cell at the DZP level of basis set. The functionals PBE and LYP are compared, both with and without dispersion.

The process of small molecule adsorption in our SLAB model is anticipated to parallel that of the cluster approach and that of calculating the H_2 PSEs in chapter 1. Open shell molecules, CN and NO, were spin polarized with a fixed spin of $\frac{1}{2}$. This may be part of the reason these two molecules are shown here to have a large PSE when compared to the other molecules. A few trends are noticed initially, but we must also observe the TZ2P results to see how they compare. Based on the overestimate of H_2 PSEs in Table 2.3 Figure 2.8, we do not expect the true binding energies of these molecules to be so large, yet observe general trends among a constant computational method and basis set. We expect that the magnitude of each PSE above to increase slightly as we move from the DZP to the TZ2P basis set.

Table 2.4: Small molecule adsorption energies and optimized height above graphene sheet calculated using SIESTA and a TZ2P basis set.

TZ2P SIESTA Results			
Adsorbate	Functional	Height Å	PSE kJ/mol
H_2	PBE	2.78	-20.3
H_2	PBE-D	2.43	-40.8
H_2	LYP	2.89	-17.7
H_2	LYP-D	2.79	-36.5
N_2	PBE	2.82	-43.6
N_2	PBE-D	2.72	-86.0
N_2	LYP	2.88	-36.8
N_2	LYP-D	2.75	-77.3
HF	PBE	2.58	-36.1
HF	PBE-D	2.52	-70.4
HF	LYP	2.63	-32.9
HF	LYP-D	2.53	-65.9
CN	PBE	2.91	-81.1
CN	PBE-D	2.93	-105.8
CN	LYP	2.89	-85.9
CN	LYP-D	2.87	-109.1
NO	PBE	2.54	-56.1
NO	PBE-D	2.47	-99.0
NO	LYP	2.67	-48.2
NO	LYP-D	2.60	-88.4
NH_3	PBE	3.3	-41.0
NH_3	PBE-D	2.82	-78.0
NH_3	LYP	3.28	-34.8
NH_3	B3LYP-D	2.88	-69.7
H_2O	PBE	3.04	-38.7
H_2O	PBE-D	2.85	-68.1
H_2O	LYP	3.04	-35.4
H_2O	LYP-D	2.85	-63.4
CH_4	PBE	3.38	-26.9
CH_4	PBE-D	3.20	-52.0
CH_4	LYP	4.36	-28.0
CH_4	LYP-D	3.12	-48.6
CO	PBE	2.78	-45.5
CO	PBE-D	2.72	-62.6
CO	LYP	2.88	-39.3
CO	LYP-D	2.82	-55.5

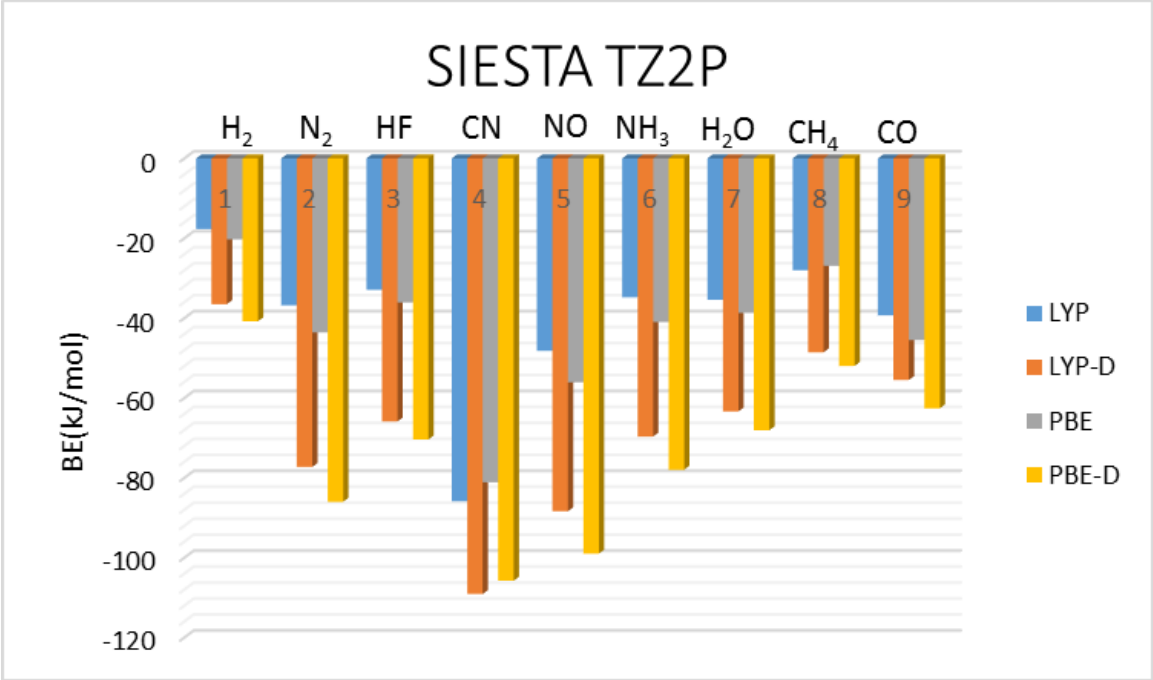

Figure 2.9: Small molecule adsorption energies with respect to SIESTA functional at the TZZP basis set level

Figure 2.9, and Table 2.4 show the physisorption energies of our selection of small molecules on the 32-carbon unit cell at the TZ2P level of basis set. The functionals PBE and LYP are compared, both with and without dispersion. The same general trends are observed as with Figure 2.8, with a slight increase in magnitude of all of the PSEs as the basis set size was increased from DZP to TZ2P. At the TZ2P basis set, our H_2 PSEs are overestimated in the SLAB results. The LYP/TZ2P method will be the method of choice for the present investigation as it gives the closest estimate to the accepted H_2 PSE. Ongoing research with these SIESTA results now focuses on general trends between molecules as we now compare the calculations listed in this section from SIESTA to similar calculations performed with GAMESS. The general trend in the LYP/TZ2P SIESTA calculations is this: The small molecules PSEs on graphene ordered strongest to weakest are CN, NO, CO, N_2, H_2O, NH_3, HF, CH_4, and H_2. The same trend is expectd to be seen in the GAMESS results that are presented in the next section.

2.4.3 Small Molecules Adsorption with Cluster Calculations

A conclusion from a Section 2.2.1 is that B3LYP-D/6-311G(2d,p)+ calculations in GAMESS give reasonable H_2 PSEs. For DFT calculations, we know that B3LYP is a reliable functional, it unfortunately is not available in the SIESTA package. The reason is B3LYP is a hybrid DFT functional that includes a portion of Hartree Fock exchange. SIESTA, and most other similar codes, are purely DFT programs and do not do Hartree Fock calculations as it is known they do not accurately depict the density of states at the fermi level for metals. SIESTA and other periodic DFT programs are often used for bulk systems where this shortcoming of Hartree Fock is also prevalent. The commonly used in solid state calculations PBE functional[17, 36, 11] is available in both GAMESS and SIESTA. By comparing the results side by side, cluster versus SLAB, we can get a better understanding of our system and perhaps even fine tune the SLAB results to better match expected values.

To obtain the following adsorption energies, first the small molecules and coronene were optimized in their isolated states with the corresponding basis set and functional. Then, the small molecule was placed atop the center site of coronene and the entire cluster was then fully optimized and its vibrational frequencies were determined. The resulting ZPE corrected energy was then used along with equation 2.1 to calculate the PSEs that are reported below. For open-shell molecules, CN and NO, were both run as doublets, with multiplicity 2S+1 with S being the total spin of the unpaired electrons. UHF was used unless spin contamination became prevalent or convergence issues arose. In either of these cases ROHF was used and is noted accordingly in the corresponding data.

Table 2.5: Small molecule adsorption energies and optimized height above coronene substrate calculated using GAMESS and a 6-31G* basis set.

6-31G* GAMESS Results			
Adsorbate	Functional	Height Å	PSE kJ/mol
H_2	PBE	3.38	-1.1
H_2	PBE-D	3.02	-6.4
H_2	B3LYP	10.0	0.0(1)
H_2	B3LYP-D	2.91	-5.82
N_2	PBE	3.51	-2.80
N_2	PBE-D	3.22	-13.41
N_2	B3LYP	3.79	-0.26
N_2	B3LYP-D	3.15	-14.65
HF	PBE	2.55	-16.33
HF	PBE-D	2.50	-25.58
HF	B3LYP	2.63	-12.37
HF	B3LYP-D	2.51	-26.20
CN	PBE	DNC	DNC
CN	PBE-D	DNC	DNC
CN	B3LYP	2.71	-236.38
CN	B3LYP-D	2.70	-252.47
NO	PBE	DNC	DNC
NO	PBE-D	DNC	DNC
NO	B3LYP	3.48	-1.14
NO	B3LYP-D	2.99	-16.94
NH_3	PBE	3.27	-8.89
NH_3	PBE-D	3.07	-22.21
NH_3	B3LYP	3.77	1.72
NH_3	B3LYP-D	3.01	-23.00
H_2O	PBE	2.90	-12.19
H_2O	PBE-D	2.77	-24.36
H_2O	B3LYP	3.00	-8.52
H_2O	B3LYP-D	2.74	-26.01
CH_4	PBE	3.90	-2.63
CH_4	PBE-D	3.52	-13.37
CH_4	B3LYP	4.20	-0.26
CH_4	B3LYP-D	3.43	-14.21
CO	PBE	3.48	-3.58
CO	PBE-D	3.18	-14.42
CO	B3LYP	3.64	-0.88
CO	B3LYP-D	3.16	-15.92

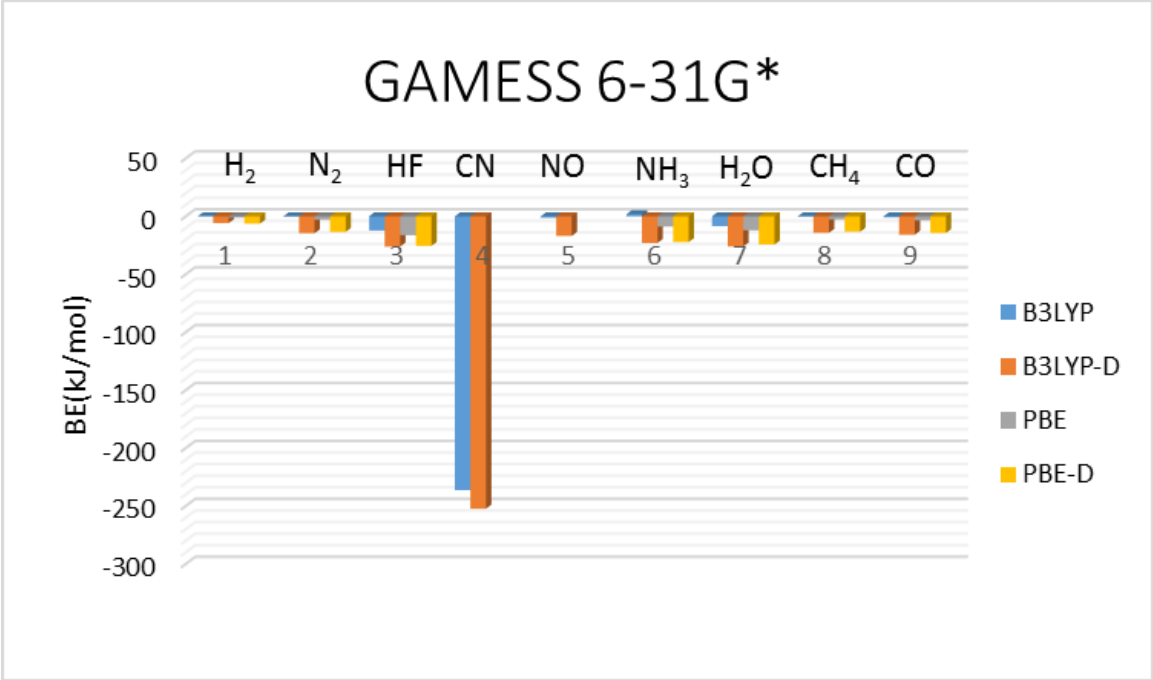

Figure 2.10: Small molecule adsorption energies on coronene with respect to GAMESS functional with the 6-31G* basis set level

Figure 2.10, as with Table 2.5, shows the physisorption energies of our selection of small molecules on the center site of coronene using 6-31G* as a basis set. The functionals PBE and B3LYP are compared, both with and without dispersion. All structures were optimized in their separated components with the labeled functional and basis set. After this the Small molecule was placed atop the center-cite of the coronene substrate followed by a full geometry optimization. PSEs were calculated using equation 2.1 as before. All open-shell molecules were run as Unrestricted Hartree Fock (UHF). The entry of "DNC" indicates the SCF procedure did not converge. There are an innumerable number of ways to have convergence issues in computational chemistry. The easiest of these is to have a bad starting geometry. There are also many tricks that can be done, by altering the Fock matrix, switching from second order SCF (SOSCF)to Pulay's direct iteration of the iterative subspace (DIIS), depending on the method used. For DFT, DIIS is the default, so switching to SOSCF may help convergence. Also in DFT, we can alter convergence criteria in the integration grids, by choosing what thresholds to turn off DFT and do pure SCF iterations, and what to threshold to switch to the more precise integration grid. After

much deliberation attempting to get the above calculations to converge, it was determined satisfactory to just rely on our B3LYP results for those compounds. If all of the open shell calculations did not converge this would be more of an issue, luckily we retain the B3LYP and B3LYP-D results for NO and CN PSEs. To check that the convergence issues were not from inaccurate starting geometries, the final B3LYP structures were then ran as PBE, and still no convergence. We will conclude for the purposes of this section, that the PBE functional does not do well at representing open shell systems using an unrestricted or restricted open-shell formalism. However, for the closed shell systems, the PBE-D functional agrees quite well with our B3LYP-D calculations.

Table 2.6 shows just what Table 2.5 did but at the 6-311G(2d,p)+ basis set size. The functionals PBE and B3LYP are compared, both with and without dispersion. In addition, MP2/6-311G(2d,p)+ results are also included for final comparison. Figure 2.11, also shows the physisorption energies of our selection of small molecules on the center site of coronene using the and 6-311G(2d,p)+ basis sets.

Table 2.6: Small molecule adsorption energies and optimized height above coronene substrate calculated using 6-311G*(2d,p)+ basis set.

6-311G(2d,p)+ GAMESS Results			
Adsorbate	Functional	Height Å	PSE kJ/mol
H_2	PBE	3.38	-1.5
H_2	PBE-D	3.0	-6.9
H_2	B3LYP	10.0	0.0(1)
H_2	B3LYP-D	2.52	-6.1
H_2	MP2	3.04	-6.1
N_2	PBE	3.53	-3.5
N_2	PBE-D	3.24	-14.0
N_2	B3LYP	3.82	-0.6
N_2	B3LYP-D	3.15	-14.3
N_2	MP2	3.03	-15.4
HF	PBE	2.53	-22.5
HF	PBE-D	2.51	-30.2
HF	B3LYP	2.65	-15.5
HF	B3LYP-D	257	-26.2
HF	MP2	2.58	-26.2
CN	PBE	DNC	DNC
CN	PBE-D	DNC	DNC
CN	B3LYP	2.72	-234.0
CN	B3LYP-D	2.70	-251.7
CN	RO-MP2	2.69	-249
NO	PBE	DNC	DNC
NO	PBE-D	DNC	DNC
NO	B3LYP	3.51	-1.4
NO	B3LYP-D	2.94	-16.7
NO	RO-MP2	2.94	10.0
NH_3	PBE	3.22	-12.3
NH_3	PBE-D	3.04	-26.1
NH_3	B3LYP	3.70	-0.5
NH_3	B3LYP-D	2.86	-21.7
NH_3	MP2	3.08	-17.8
H_2O	PBE	2.83	-16.9
H_2O	PBE-D	2.73	-29.5
H_2O	B3LYP	2.94	-11.6
H_2O	B3LYP-D	2.75	-29.7
H_2O	MP2	2.71	-28.5
CH_4	PBE	3.93	-2.8
CH_4	PBE-D	3.52	-13.5
CH_4	B3LYP	4.31	-0.2
CH_4	B3LYP-D	3.40	-14.6
CH_4	MP2	3.22	-20.6
CO	PBE	3.48	-3.6
CO	PBE-D	3.18	-14.0
CO	B3LYP	3.93	-0.7
CO	B3LYP-D	3.18	-14.5
CO	MP2	3.08	-18.8

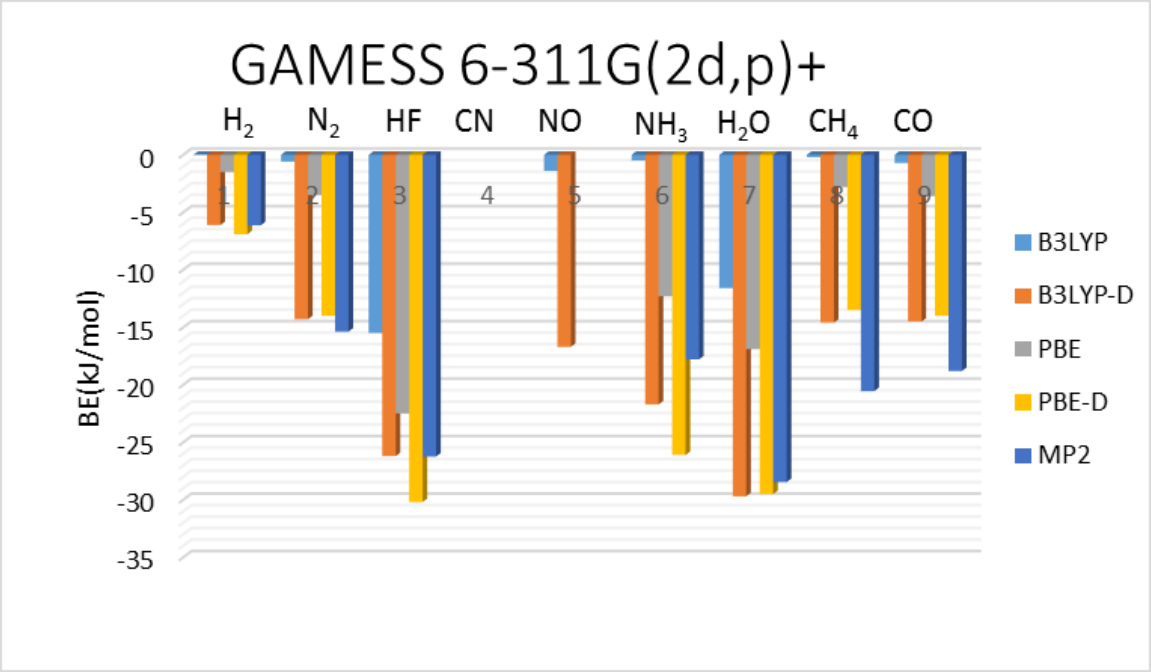

Figure 2.11: Small molecule adsorption energies on coronene substrate with respect to GAMESS functional with the 6-311G(2d,p)+ basis set level

The PSEs of CN on coronene have been intentionally left out of Figure 2.11 and can be referenced in the table. The reason is so that trends can be seen among the other adsorbants, as they are all significantly smaller in magnitude. We are interested in relatively small physisorption binding energies, and even in the MP2 results, the CN PSEs dominate the scale of Figure 2.10 and would do the same for Figure 2.11 so they have been intentionally left out. Additionally, the three top adsorbate's with the highest PSEs are shown below with the bond lengths of the adsorbate labeled in Angstroms. The general trend in the B3LYP-D/6-311G(2d,p)+ GAMESS calculations is this: The small molecules PSEs on coronene ordered strongest to weakest are CN, H_2O, HF, NH_3, NO, CH_4, CO, N_2 and H_2; and the same rank for the MP2 results: CN, H_2O, HF, CH_4, NH_3, N_2, and H_2 and then NO was not seen to adsorb. Recall the trend expected from the SIESTA results listed in the previous section again in order of strongest to weakest PSE is CN, NO, CO, N_2, H_2O, NH_3, HF, CH_4, and H_2. A similar pattern is seen between the B3LYP-D and MP2 results, perhaps the most interesting of which is the second highest PSE of H_2O. This appears to be due to the hydrogen atoms in the H_2O structure interacting with the PAH, as with the third highest PSE with HF see Figure 2.12. In both of these structures, the average C-C framework has not significantly been distorted. In the case of CN, the carbon atom of CN is forming a

C-C bond of 1.491 Å with a constituent of the center ring of coronene, causing significant distortion in the PAH as the carbon atom is lifted 0.610 Å from its original position in the once planar coronene resulting in the chemisorption energy of -249 kJ/mol.

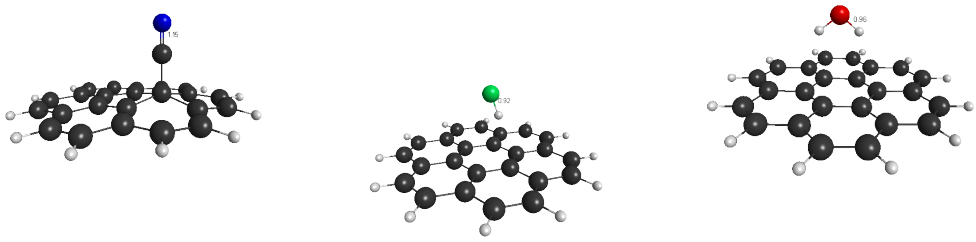

Figure 2.12: NaCN, HF, and H_2 optimized locations atop coronene shown with corresponding MP2/6-311G(2d,p)+ equilibrium bond lengths.

The equilibrium bond lengths of H_2O and HF remained the same before and after adsorption on coronene. CN had a bond length of 1.277Å before adsorption reducing to 1.150Å after adsorption to coronene. This could be due to the fact that CN was not run as a negative ion. The carbon in CN is getting this electron from the carbon in coronene as it makes a covalent C-C bond, in turn shortening the CN bond to that expected in CN^-. This molecule was added on top of a standard set from the literature as CN is known to have halogen like behavior. It may sound intuitive to some that an open-shell molecule such as CN or NO would have a larger interaction with the delocalized π-network of the substrate, but this is not observed in our other open shell candidate, NO. NO is relatively stable as an open shell whereas CN wants to pick up anothe electron and form CN^-. There have, however been convergence issues with these open shell CN and NO calculations. As seen in Table 2.6, both of these molecules optimized on coronene in a restricted, open shell formalism as the unrestricted Hartree Fock calculations lead to spin contaminants and eigenvalues of zero. The RO-MP2 PSE for NO on coronene was a positive value, suggesting further problems with these two cases and justifying their exclusion from Figure 2.11. Also, having a look at the resulting structure in the above figure, shows CN forming a covalent C-C bond with coronene. Moreover CN groups often behave like Halogens, yet HF's PSEs are not nearly as large, although they are greater in magnitude than NO, despite HF being a closed shell. The sheer magnitude of the CN PSEs, although a cause for alarm, are still most likely

indicative of a strong interaction. It is believed that the CN is making a bond of a covalent type with the coronene which is evident in the magnitude of the calculated CN binding energies. It is known that UHF calculations often result in spin contamination. This is because the UHF wavefunction is not an eigenfunction of the total spin operator [32]. The eigenvalues of the total spin operator are given by

$$\hat{S}^2 = s(s+1)\hbar^2 \tag{2.2}$$

Where s is the total spin associated with the unpaired electrons. It turns out that the ROHF (Restricted Open Shell Hartree Fock) wavefunction, like the true wavefunction of the system, is an eigenvalue of Equation 2.2. The reason that UHF is prefered over ROHF is that unrestricted wavefunctions give lower energies than the restricted correspondent. If the approximate energy resultant from the Schrödinger equation is greater than or equal to the exact energy of the system, then of course lower energies are desirable. An interesting result can be derived where in certain situations, where the unrestricted solution is lower in energy than the closed shell restricted solution. Although the UHF wavefunctions may be contaminated with higher spin states, they are still often reliable in terms of the energies they give, especially in DFT calculations [40]. UHF wavefunctions also provide a starting point for higher order correlation methods such as Perturbation Theory or Configuration Interaction.

The easiest way to remove spin contamination from the wavefunction is to restrict all of the paired electrons to share the same spatial orbital, this is the ROHF method. An alternative, and powerful, method to accurately represent open shell system is with a Multi-Configuration SCF (MCSCF). This method allows the wavefunction to be represented as a linear combination of multiple determinants so that each degenerate component can be represented equally [26]. We are not presently concerned with the latter of these methods but we did however address NC-coronene with ROHF to see if it is an artifact of spin contamination in the wavefunction. Our UHF B3LYP-D/6-311G(2d,p)+ NC-coronene binding energy gave a binding energy of -251.7 kJ/mol with an $\hat{S}^2 = 0.8$ compared to the expected 0.75 from one unpaired electron corresponding to s=0.5 in Equation 2.2. As this is a minimal amount of spin contamination, it is no surprise that when this was run as ROHF, our binding energy decreased slightly to -247.7 kJ/mol.

The minimal amount of spin contamination and supporting ROHF calculation suggests that the large NC-coronene binding energy is accurate. Furthermore the optimized NC-coronene structure shows the relaxation of coronene molecule until where the interacting carbon atom has moved from it's initial position in the XY plane to a height of 0.61 Å. We conclude that the CN chemically adsorbs to coronene forming a C-C bond of length 1.49 Å. This large adsorption energy makes sense as we would expect a chemisorption to have a corresponding binding energy of 100-200 kJ/mol, suggesting this is a strong chemical adsorption of a covalent type bond. Just as the atomic hydrogen chemisorption discussed in section 2.1, we are not concerned with these processes in detail here.

2.4.4 A Comparison of Cluster and SLAB calculations

From the above charts, some general trends can be observed common to both the cluster and SLAB results. The observation that CN chemisorbs to graphene is concluded among all methods. Within the weaker interacting species however, there are some discrepancies. For instance, SIESTA results suggest that CN, N_2 and NH_3 adsorb on graphene the strongest whereas GAMESS suggests this is true for CN, HF, and H_2O. This is some cause for concern. We were hoping to at least observe the same general trends among cluster and SLAB calculations. Besides the obvious case of CN, the SIESTA results may not be the most reliable. This makes sense as the whole nature of this investigation deals with weak interactions primarily due to van der Waals forces that are difficult to model theoretically.

One of the reliable qualities of the SIESTA program, and perhaps SLAB calculations in general, is it's ability to fix the spin of the system in open shell systems with unpaired electrons in spin polarized calculations. This is likely why the adsorption energies of CN from SIESTA are actually less than those from GAMESS, all the other interactions are overestimates. Pantha and Belbase in their modeling of this system have used a DFT-D_2 DFT method with ultrasoft pseudopotentials [36]. Perhaps a reason for the discrepancies in the SLAB results we have reported could be due our pseudopotentials being too hard. The pseudopotentials we have used here are from the SIESTA distribution and have all been tested for transferability before they were used. When pseudopotentials are too hard, that

means the cutoff radius was too small, and many of the contributions from the core states are still prevalent. This makes computations less efficient as a bigger basis set is also needed. If pseudopotentials are too soft because the initial cutoff radius is too large, many of the core states are negated and this can cause convergence issues and poor transferability. It would make sense that the pseudopotentials from the SIESTA database be too hard for the present investigation, which is also why they all passed the transferability tests performed, and how none of the present SLAB calculations have yet had convergence issues. By redefining our pseudopotentials and correcting for BSSE, it is believed that these SLAB calculations could be updated to agree with the cluster calculations and literature values. Also possible but less likely, we could update the dispersion correction term to further fine tune the SLAB results.

2.5 Trends and Conclusions

The results of this section may be lengthy but they provide useful insight to the use of our methods on a wide range of adsorbates. Despite some overestimated PSEs we have seen, some general trends can still be observed. The most notable is, CN. Even though we are not presently interested in chemisorptive processes, as long as it is not hydrogen that is chemisorbed to our substrate, we still seek to increase the PSE of hydrogen on graphene so these stronger interacting species could still be of interest to us. Continuing on in the next phase of this goal, we move onto investigate compounds on graphene related to light metal atoms we can adsorb to the surface, and possibly halogenated compounds if they do not chemically bind to our substrate. The reason for this is we wish to keep the graphene intact and to maintain it's aromaticity. It has been seen that after the chemisorption of one hydrogen atom, subsequent adsoption process become increasingly favorable and can result in a reduced substrate [19].

Chapter 3

Effect of Coadsorbates on H_2 Physisorption on Graphene

In Chapter 2, a reliable computational method to explore lightweight adsorbants atop graphene was developed. Once the method was established, it was tested on a standard selection of molecules. The adsorption energies of these small molecules were reported. Careful analysis of these results revealed limitations to the defined computational methods. We use the approach described in Chapter 2 as a calibration step which facilitates investigating more interesting systems. This chapter begins by considering the sequential adsorption of multiple hydrogen molecules atop graphene. After this we investigate physically adsorbed atoms (adatoms) and then physically adsorbed diatomic molecules on graphene and calculate their corresponding effect on the H_2 physisorption. Each adsorption process is investigated thoroughly with GAMESS using the cluster approach and then compared against the results of the SLAB calculations obtained by SIESTA.

3.1 Introduction

Adsorption of hydrogen in different porous materials and carbon nanotubes has been extensively studied recently in attempts to increase storage capacities. It has been shown that an appreciable amount of hydrogen can be stored in these types of materials at low temperatures [12]. The majority of ongoing research on this topic is aimed towards generating the storage capacity needed for standard operating conditions in practical applications. One way to do this is to increase H_2's affinity for the carbon substrate by the decorative addition of coadsorbates to the surface of the substrate prior to H_2 adsorption. Transition metals such as Pd or Pt have been shown to increase H_2 binding energies by up to -87 kJ/mol [12]. The high energy required to rearrange the carbon atoms maintains aromaticity and prevents reduction of graphene to graphane to occur in these systems[44]. A binding energy between that of physisorption and chemisorption is optimal for storage applications[28]. Results nearing -100 kJ/mol make Pd or Pt possible solutions. Problems with using Pd or Pt, include their high atomic weight which reduces the overall gravimetric capacity in terms of hydrogen storage, and these metals are rare and costly.

The present investigation aims to find metal adatoms and/or simple small molecules that will increase H_2's PSE. To increase H_2 PSE to a value somewhere between chemisorption and physisorption without the need for heavy or precious metals would clearly be a valuable result. Starting with the simplest of solutions, lightweight Alkali metals such as Li and Na are of interest. Such adatoms have been shown to increase H_2 PSE on graphene of up to -34 kJ/mol and -19 kJ/mol respectively [11, 36]. In Chapter 2, we explored halogenated compounds interacting with graphene. The lightest halogen, fluorine, is the most electronegative and most reactive element. This is in part why the C-F bond is one of the strongest chemical bonds we know of and compounds of carbon and fluorine have many practical industrial applications for this reason. We saw in Chapter 2 that CN, which can behave as a pseudohalogen, chemisorbs readily to the surface of graphene, yet HF only physisorbs and we have a computational method that will accurately describe both interactions. It is assumed these same methods will also accuratly depict an adsorption energy between that of a chemi- and physisorbed state. Pd and Pt adatoms give such H_2 PSEs, nearing -100 kJ/mol [12]. Na and Li produce PSEs that are close to these but not as strong as in the

Pd and Pt systems. With the idea that a physisorbed adatom or small molecule is ideal for the purpose of increasing H_2 PSE's and improving the gravimetric content of H_2, we now focus light metal adatoms Li and Na before adding to them light Halogens F and Cl. All resulting systems are used to observe their effects on hydrogen storage capacity.

3.2 Multiple H_2 Physisorption using Cluster Calculations

Before investigating coadsorbate systems, we must first make a brief return to only carbon and hydrogen systems yet again. This time we move beyond one molecule of hydrogen to explore multiple H_2 adsorption on the graphene surface. This is done so that upon the addition of adatoms, it can be seen both how many molecules the system can adsorb, but also to confirm that in the case of a single H_2 molecule, it is adsorbed at the optimal location. The idea is simple, if we flood the system with several adsorbed H_2 molecules, one at a time, then eventually a saturation limit will be reached where the H_2 binding energy becomes small. Analysis of the resulting structure increases the chances significantly one of the adsorbates will be in a location that gives a maximum binding energy. Averaged H_2 PSEs are reported, as some molecules are adsorbed with a stronger PSE than others.

Using the methods from section 2.2.1, which consists of the 6-311G(2d,p)+ basis set combined with B3LYP-D and MP2 energy calculations, the H_2 PSEs on coronene are extended to contain 2, 3, 4, and 5 H_2 molecules. With the addition of each subsequent H_2, the resulting clusters were all fully optimized to the same computational specifications. From the fully optimized structures, the average H_2 PSEs are calculated using

$$B_E = \frac{1}{n}(E_B - E_S - E_{nH_2}) \tag{3.1}$$

Where E_B is the energy of the entire optimized cluster and E_S is the energy of the coronene substrate. E_{nH_2} is the energy of the subcluster of the n H_2 molecules after the geometry optimization. Equation 3.1 gives an H_2 PSE averaged over all n of the H_2 molecules in the cluster.

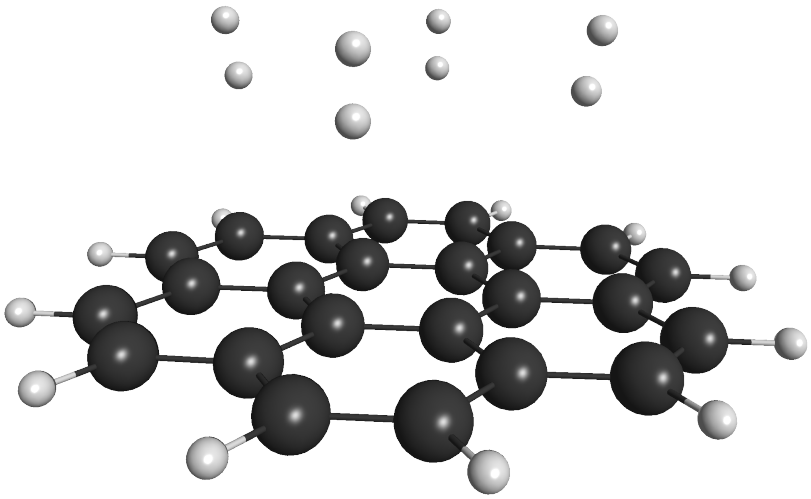

Figure 3.1: Optimized $C_{24}H_{12}{\cdot}4H_2$: The structure of coronene with a maximum number of H_2 adsorbed in their prefered locations calcualted with MP2/6-311G(2d,p)+. The four adsorbates are prependicular within 1° to the plane of the coronene with an average center of mass distance of 3.08Å . The four H_2 molecules are coordinated with the centers of four of the six equivalent outer rings of the substrate.

Table 3.1: Multiple H_2 Molecules Adsorbed on coronene
The energy method used, number of adsorbed hydrogen molecules and adsorption energies averaged over the n molecules are summarized. The corresponding adsorption heights are defined by d in Figure 2.5b. The number of imaginary frequencies are indicated by $\nu_e < 0$.

GAMESS Results: $C_{24}H_{12} \cdot nH_2$				
Method	n	Height $\mathring{A}$	PS Energy	$\nu_e < 0$
B3LYPD	1	3.02	-6.1	0
	2	2.98	-6.4	0
	3	2.92	-6.2	0
	4	3.04	-6.1	0
	5	3.02	-5.7	1
MP2	1	3.04	-6.1	0
	2	3.04	-6.0	0
	3	3.05	-6.1	0
	4	3.08	-5.8	0
	5	3.12	-5.4	1

Table 3.1 shows the 6-311G(2d,p)+ PSEs for 1-5 H_2 molecules on coronene, averaged over the n adsorbed molecules. Figure 3.1 shows the MP2/6-311G(2d,p)+ optimized structure for 4 H_2 on coronene. The perspective drawing is used for visual clarity, but if one were to look down the Z-axis towards the XY plane where the PAH lies, the 4 H_2 adsorbates are oriented perpendicularly above the center sites of the outer C_6 rings of the substrate with 3.12 Å average distance to the respective H_2 center of mass. The same structure from the B3LYP-D optimization had an average adsorbate height of 3.02 Å . The average H-H bond lengths are 0.74 Å in both methods and changes in the geometry of the coronene substrate are negligible.

Similar DFT calculations have been performed to show up to five H_2's adsorbed to coronene with an average PSE per H_2 of -6.6 kJ/mol [36] in good agreement with our present results. Figure 3.1 only shows $4H_2$'s adsorbed on coronene for the following reason. For every additional molecule, a full geometry optimization and frequency calculation was performed. These calculations we used to show that the optimized structure is a proper minimum and obtain the ZPE correction. The calculated frequencies from the B3LYP calculations containing 4 and $5H_2$'s are shown in Figures 3.2 and 3.3 below.

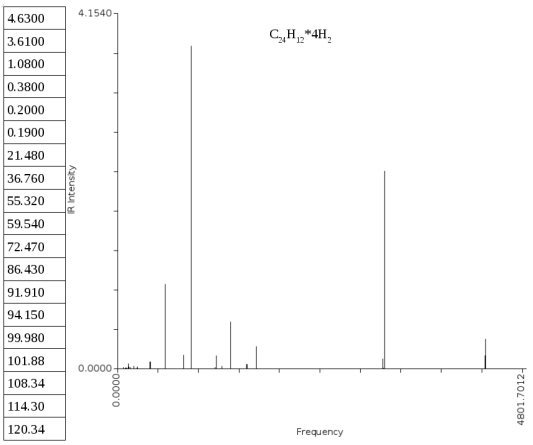

Figure 3.2: $C_{24}H_{12}{\cdot}4H_2$:
The vibrational frequencies of coronene with four adsorbed H_2 molecules are shown with their corresponding IR intensities. The lowest few of the vibrational frequencies are listed on the left, none of which are negative.

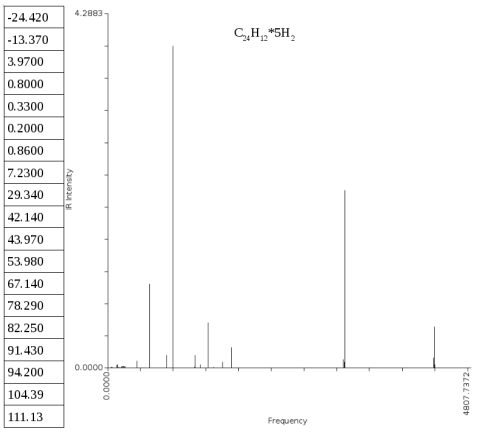

Figure 3.3: $C_{24}H_{12}{\cdot}5H_2$:
The vibrational frequencies of coronene with five adsorbed H_2 molecules are shown with their corresponding IR intensities. The lowest few of the vibrational frequencies are listed on the left, two of which are negative.

Imaginary frequencies are observed as the first two entries on the left of Figure 3.3, labeled as negative frequencies. No imaginary frequencies are observed in Figure 3.2. The frequencies in Figure 3.3 suggest $C_{24}H_{12}{\cdot}5H_2$ is a transition state. This can be checked with a PES scan of the internal reaction coordinates, IRCs, which would most likely indicate that one of the H_2 molecules wants to leave the cluster due to H_2 saturation. With these IRC's, we can move on the PES away from this transition or saddle point to remove these negative frequencies. This in turn changes the final energy slightly. As opposed to this method, for the purposes of this investigation, we just take the last H_2 addition as a saturation limit of our cluster. This is justified by the corresponding decrease in PSE seen in Table 3.1 upon addition of the 5th H_2 molecule to Figure 3.1. Removal of one of the H_2 adsorbates owing to the imaginary vibrational frequencies is also supported simply by looking at the structures. As the H_2 adsobing distance becomes significantly larger than the opimal 3 Å, these imaginary frequencies tend to appear. In Figure 3.1, we see 4 molecules adsorbed perpendicular above the C_6 hollow sites of coronene, the corrseponding structure with 5 H_2 shows a fifth H_2 adsorbing towards the edge of the coronene molecule, suggesting it may want to leave the cluster. The lower corresponding PSEs in Table 3.1 show this fifth H_2 has a significantly low PSE to bring the average down to -5.4 kJ/mol.

From these results it is concluded that we can adsorb up to four H_2 molecules atop coronene with an average PSE of -5.8 kJ/mol at an average height of 3.08 Å. Addition of subsequent H_2 appear to want to desorb from the cluster and result in imaaginary vibrational frequencies. These results are in good agreement with literature values that showed up to five H_2 molecules adsorbed on graphene represented by a periodic approach [36]. We are now in a position to investigate the effect of coadsorbates on this system using GAMESS but first compare some SIESTA results.

3.3 Multiple H_2 Physisorption using SLAB Calculations

The SLAB calulations from Chapter 2 left some accuracy to be desired. The calculated H_2 LYP/TZ2P PSE of -17.7 kJ/mol being substantially different than the accepted -5.0 kJ/mol and our cluster results of -6.1 kJ/mol. In this section we mimic the above process of

sequential adsorption of H_2 on coronene using our SLAB methods defined in Section 2.2.2 to sequentially adsorb 1-5 H_2 molecules to graphene. For each additional H_2 adsorption to the unit cell a full geometry optimiztion of the unit cell and all coordinates was performed. We present here the final results of this process. Shown below is 5 H_2 molecules adsorbed onto graphene using LYP and PBE functionals, both with and without dispersion. The average adsorbate height d, H_2 bond lengths, and corresponding PSE in kJ/mol averaged over the 5 adsorbate molecules are shown below.

Table 3.2: Adsorption energies and heights of 5 adsorbed H_2 molecules on graphene. Four DFT functionals are compared. The structure in Figure 3.4 corresponds to the second row of this table. Average adsorbate bond lengths are also reported.

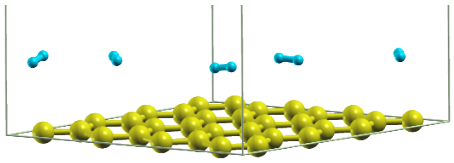

SIESTA Results: graphene·5H_2			
Method	d	H-H	PSE(/H_2)
LYP	2.967	0.766	-16.3
LYP-D	2.792	0.764	-33.5
PBE	2.928	0.771	-18.4
PBE-D	2.663	0.770	-37.1

Figure 3.4:
graphene·5H_2: LYP-D/TZ2P
This figure shows 5 H_2 molecules adsorbed on graphene in a 32-carbon unit cell with $\alpha = \beta = 90°$ and $\gamma = 120°$. The same systems calculated with the other functionals in Table 3.2 have very similar sturctures. The H_2 molecules prefer to adsorb above the center of the C_6 rings of graphene at a height of just under 3 Å.

Figure 3.4 shows the structure of the floor of the hexagonal 32-carbon unit cell with 5 adsorbed H_2 molecules. This structure was calculated using LYP-D/TZ2P. The structures of the same system using the other three functionals are very similar so only one is shown. The differences between these methods is shown in Table 3.2. Comparing these adsorption energies from the single adsorbate values shown in Table 2.2, it can be seen that increasing the number of adsorbates does not significantly change the corresponding PSE. The single H-H equilibrium bond length in the same 32-carbon unit cell with the carbon atoms removed was calculated at the TZ2P basis set with the LYP functional to be 0.764 Å and with PBE to be 0.769 Å. The average H-H bond lengths shown in Table 3.2 do not significantly change from these initial values. With 5 adsorbed H_2 molecules, each functional investigated does show a change in a few kJ/mol, which in comparison to the cluster results is about the same observed change. Also consistent with the cluster calculations, the H_2 molecules preferentially adsorb to the center sites of the graphene sheet. However, in Figure 3.4, it can be seen the H_2 molecules are adsorbing parallel to the graphene sheet, unlike the cluster

calculations where they adsorbed perpendicular to the center sites of the substrate. In the cluster calculations, we are limited by the size of the PAH and in the SLAB calculations by the size of the unit cell. Due to the periodicity of the SLAB calculations, we expect to be able to adsorb more H_2's per unit cell, as there are no terminal hydrogens in the substrate to interact with. The H_2 molecules are able to spread out more in the 32-carbon unit cell than on the 24-carbon coronene molecule. This is due to there being more carbons in the unit cell substrate, but moreover because of the periodicity and absence of terminal hydrogen atoms. With extra diffuse functions to represent the hydrogens in GAMESS, it is found sometimes during geometry optimizations that the hydrogen atoms will become close to each other in the final structures. In our present SLAB results, although overestimates the PSE, the LYP functional gives the best result for H_2 on graphene and LYP/TZ2P SIESTA results will continue to be compared in subsequent sections for this reason.

3.4 Influence of Alkali Metal Coadsorbates: Clusters

Before investigating a series of Alkali Halides, we begin by considering Li and Na atoms as coadsorbates on coronene.

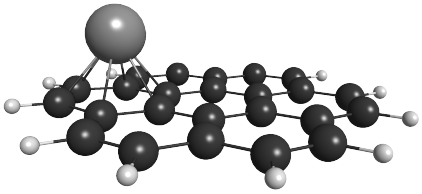

Figure 3.5: $C_{24}H_{12}$·Li:
The structure of coronene with Li adsorbed is shown, optimized with B3LYP-D functional and 6-311G(2d,p)+ basis set. Li is adsorbed atop the center of an outer ring of coronene at a height of 1.621 Å above the carbon plane.

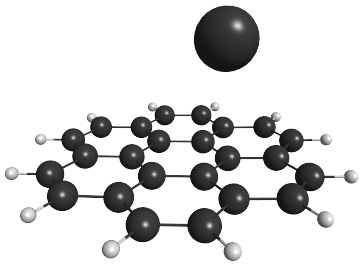

Figure 3.6: $C_{24}H_{12}$·Na:
The structure of coronene with Na adsorbed, optimized with the B3LYP-D functional and 6-311G(2d,p)+ basis set. Na is adsorbed atop a carbon atom of the central ring of coronene at a height of 2.95 Å.

Figure's 3.4 and 3.5 show the B3LYP-D/6-311G(2d,p)+ optimized structures of Li and Na as adatoms atop coronene. Both structures were first calculated as unrestricted open shells with zero net charge and a spin multiplicity of 2 associated with the unpaired electron. A full geometry optimization was performed using starting structures with Li or Na at the center of the center ring of planar coronene at a height of 2.0 Å. In UB3LYP-D calculations the Li atom adsorbs to the center of an outer ring of coronene at a height of 1.621 Å above the carbon plane with a corresponding attraction of -62.4 kJ/mol whereas the ROMP2 calculations give a vertical height of 1.600 Å and an adsorption energy of -53.5 kJ/mol. Both methods show the optimal location for the Li is atop the center of the same outer ring of coronene. Na is shown adsorbed directly above a carbon atom of the central ring of coronene in the UB3LYP-D calculations at a height of 2.95 Å with a PSE of -40.2 kJ/mol compared to RO-MP2 results of 2.80 Å and -16.6 kJ/mol. Other methods show the optimal location for the Na is atop the center of the central ring of coronene. The same calculations on both Li-coronene and Na-coronene ran as UMP2 ran into convergence issues and gave positive binding energies. In the structures above, the average C-C bond lengths are 1.417 Å and 1.412 Å respectively which are slightly relaxed compared to the calculated 1.410 Å average prior to addition of the adatoms.

The UB3LYP-D Na-coronene PSE of -40.2 kJ/mol matches well with the reference value of -43.4 kJ/mol [36]. Our calculated UB3LYP-D Li-coronene PSE however, does not match well with the reference value of -147.6 kJ/mol [11]. This reference does not give the heights of the adsorbed Li and it is likely that their structure was that of a chemisorbed minimum based on the magnitude of the binding energy Kim et al. reported [11]. The ROHF calculation on this system shows Li adsorbed at a height of 3 Å above the center of the central ring in coronene, which is expected for Li atom physisorption. The unrestricted case for Li gives a stronger physisorption attraction on the outer ring, correlating better with the literature values, so this structure is kept and used for H_2 adsorption in the next section. The structure shown in Figure 3.5 had a lowest vibrational frequency of 15.29 cm^{-1}, indicating it is a local minimum on its PES. As we have seen with atomic hydrogen, it is possible that atoms have the potential to either physisorb or chemisorb to coronene, depending on the height, with the shorter adsorbate to substrate distance corresponding to a chemisorbed state. We have shown that both Li and Na physisorb to coronene. It is

possible then that we have found a local potential well corresponding to a physisorbed state and Kim et al. found a minimum corresponding to a chemisorbed state [11]. Based on our agreement with other literature values in the other results up to this point, we still retain confidence in our method and treat the Kim et al. reference values with caution, especially as they did not report Li-graphene distances. This is a good reason for including adsorbate heights with binding energies, to fully understand the nature of the system being studied. We now move onto H_2 adsorption on the structures in Figures 3.4 and 3.5 and calculate the corresponding H_2 binding energies.

3.4.1 Effect of Li and Na Coadsorbates on H_2 Storage

Similar to the procedures used in Section 3.2, we now use the optimized Li-coronene and Na-coronene structures from Figures 3.5 and 3.6 as new substrates for H_2 adsorption. To these Alkali metal decorated PAH's, n=1-5 H_2 molecules are sequentially adsorbed, and the resulting clusters are optimized upon each H_2 addition. From each optimized structure, the PSE of the n adsorbed H_2 molecules is given by Equation 3.1 where E_S is the energy of the substrate, either Li-coronene or Na-coronene. The resulting B_E is then represents the H_2 PSE averaged over the n adsorbed molecules. Also of interest is the adsorption energy of coronene on the $nH_2{\cdot}A$ subcluster, where A is either Li or Na. That is to say

$$B_{E_2} = \frac{1}{n}(E_B - E_C - E_{nH_2 \cdot A}) \tag{3.2}$$

Where E_B is the total energy of the entire cluster, E_C is the energy of the coronene portion of the cluster and $E_{nH_2 \cdot A}$ is the rest of the cluster. $E_{nH_2 \cdot A}$ is therefore energy of the subcluster of either Na or Li and the adsorbed hydrogens. B_{E_2} shows the binding energy of coronene on the rest of the cluster. This coronene-subcluster binding energy is called B_{E_2} to avoid confusion with B_E from Equation 3.1. Equation 3.2 is often reserved for some of the more interesting systems where it is advantageous to see the effect of the H_2 adsorption has on the adatom's affinity for the PAH.

During each n=1-5 H_2 adsorption, the geometry of the cluster is optimized and the vibrational frequencies are calculated at each n. The same saturation limit as in Section 3.2 is observed where eventually one of the H_2 molecules starts to have an imaginary frequency and wants to leave the cluster. For plain coronene this limit is 4, and the addition of a

fifth H_2 results in negative frequencies. This process is now repeated for Li-coronene and Na-coronene, adding nH_2 molecules until one or more imaginary frequencies are found. In the following we list the optimized structures containing the maximum number of adsorbed H_2 molecules which have all real vibrational frequencies. Beginning with the lighter case of Li we find that the maximum n=2.

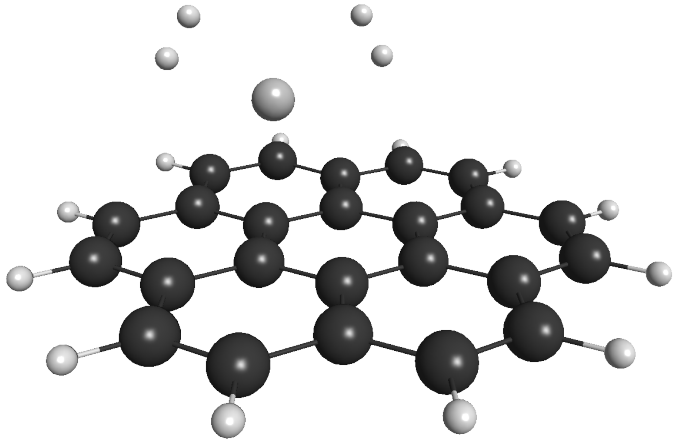

Figure 3.7: Optimized C_{24} H_{12} · Li · $2H_2$:
The final Li coadsorbed coronene cluster with maximum adsorbed H_2 molecules calculated with B3LYP-D/6-311G(2d,p)+ is shown. The same structure optimized with MP2 gives a similar geometry. The B3LYP-D and MP2 optimized geometries and binding energies are summarized in Table 3.3.

Table 3.3: Results of optimized Li-coronene with 2 adsorbed H_2 molecules. Under each computational method, average distances and adsorbing heights are reported in Å. The binding energy averaged over the two H_2 molecules,PSE /H_2, is reported in kJ/mol. The energy with the Li·$2H_2$ sublcluster's adsorption given by B_{E_2} is also reported in kJ/mol.

GAMESS Results: $C_{24}H_{12}$·Li·$2H_2$				
Method	D	Å	PSE	kJ/mol
U-B3LYPD	C-C	1.417	/H_2	-15.3
	C-Li	1.54	Li·$2H_2$	-122.4
	C-H	2.86		
	Li-H	2.16		
U-MP2	C-C	1.421	/H_2	-17.8
	C-Li	1.57	Li·$2H_2$	-128.4
	C-H	2.88		
	Li-H	2.12		

Figure 3.7 shows the final structure that corresponds to the data in the first row of Table 3.3. The MP2 structure was optimized separately, yielding a similar structure whose parameters are summarized in Table 3.2. These results show a significant increase in H_2 PSE after coadsorption of Li. Kim et al. [11] showed Li decorated graphene can increase H_2 PSE up to -34 kJ/mol in a periodic DFT approach. Although the present findings of -16 to -17 kJ/mol do not correlate that well with these expected results, it is a significant increase from the previous value of -6 kJ/mol on pure graphene. The difference in these results could be due to the initial Li-coronene structure used. Kim et al. reports a Li PSE of -148 kJ/mol which seems a bit large especially compared to our result of -62 kJ/mol. This could likely be due to the position of Li atop coronene from Figure 3.5. If Li was adsorbed in the center of the coronene as opposed to the center of one of six equivalent outer rings, we would expect both PSE values to match better with the literature values. Initial attempts were made to do this. During these calculations Li continually adsorbed in the true center of coronene but at a height greater than 3 Å and with a PSE of around -20 kJ/mol. The tighter bound state in Figure 3.7 was the lowest energy structure formed by performing geometry optimizations on many different $C_{24}H_{12}$·Li·$2H_2$ starting structures.

The same type of calculations were repeated for the Na coadsorbate and resulted in a maximum of $3H_2$ molecules being adsorbed to the cluster.

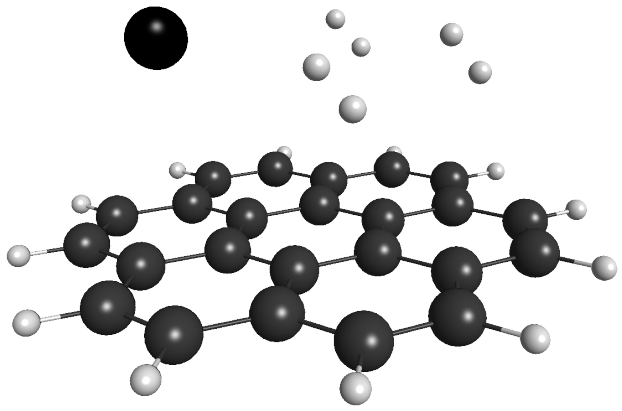

Figure 3.8: Optimized $C_{24}H_{12} \cdot Na \cdot 3H_2$:
The optimized Na coadsorbed coronene cluster with 3 H_2 molecules maximally adsorbed calculated with B3LYP-D/6-311G(2d,p)+ is shown. The same structure optimized with MP2 gives a similar geometry. The B3LYP-D and MP2 parameters can be seen in the Table 3.4.

Table 3.4: Results of optimized Na-coronene with 3 adsorbed H_2 molecules. Under each computational method, average distances and adsorbing heights are reported in Angtroms. The binding energy averaged over the three H_2 molecules,PSE $/H_2$, is reported in kJ/mol. The and associated with the $Na{\cdot}3H_2$ sublcuters adsorption,PSE B, is also reported in kJ/mol.

GAMESS Results: $C_{24}H_{12}$ ·Na· $3H_2$				
Method	D	Å	PSE	kJ/mol
U-B3LYPD	C-C	1.410	$/H_2$	-6.9
	C-Na	2.82	$Na{\cdot}3H_2$	-57.5
	C-H	3.21		
	Na-H	4.22		
U-MP2	C-C	1.398	$/H_2$	-3.3
	C-Na	2.34	$Na{\cdot}3H_2$	-23.6
	C-H	3.70		
	Na-H	6.08		

Figure 3.8 shows the final structure that corresponds to the data in the first row of Table 3.4. Again, the MP2 structure was optimized separately, yielding a similar structure whose parameters are shown in the rest Table 3.3. Contrary to what was expected, these results do not show a significant increase in H_2 PSE after coadsorption of Na, likely because the H_2 molecules do not surround the adatom. Pantha and Belbase [36] showed in periodic DFT calculations using an 18-carbon unit cell, an initial Na adsorbing height of 2.32 Å with a PSE of -43.4 kJ/mol. The reported Na-coronene PSE from Section 3.4 of -40.2 kJ/mol agrees well with this reference value which is why it is surprising that we do not see

the same increase in H_2 PSE to -19 kJ/mol at 2.48 Å [36]. The present increase reported of around -1 kJ/mol to -7 kJ/mol could be due to initial geometry of the adatom. The adsorbed height of the Na atom used of 2.95 Å is a bit larger than the reference value which would correspond to a lower binding energy. The average Na-H distance as well as the average C-H distances, are directly related to PSE. We have seen previously, a closer adsorbing height has a stronger PSE. This is seen when comparing Figures 3.8 and 3.7 also. To get the final geometries in both figures 3.7 and 3.8 careful geometry optimizations over hundreds of cycles were carried out followed by frequency calculations to correct final energies and insure local minima. It is expected that tighter structures would have higher H_2 PSEs. This can be seen in Table 3.4, as the Na-H distances are larger than 3 Å, the optimal distance for physisorption. This is why an increase of H_2 affinity for coronene is not observed, as the H_2 molecules in the cluster are primarily interacting with the coronene and not the Na. We will return to this issue momentarily, but for now we compare the above cluster results from GAMESS with our SLAB methods using SIESTA.

3.5 Influence of Alkali Metal Coadsorbates: SLABS

To prepare Li and Na decorated graphene, the adatom was first placed at 2 Å atop the center cite of the 32-carbon hexagonal unit cell from Figure 2.6b. All calculations were spin polarized with fixed spin set to one in units of electron spin. The resulting structures were optimized as described in Section 2.2.2 to produce Li-graphene and Na-graphene seen below.

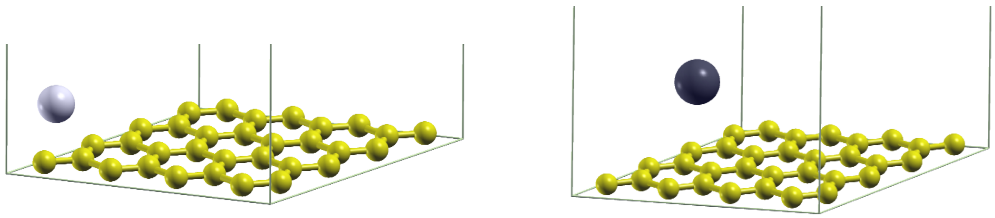

(a) $Li{\cdot}graphene$ $d{=}2.003\mathring{A}$ $PSE{=}{-}79.4kJ/mol$

(b) $Na{\cdot}graphene$ $d{=}2.636\mathring{A}$ $PSE{=}{-}35.7kJ/mol$

Figure 3.9: a)Optimized graphene·Li: The 32-carbon unit cell with $\alpha = \beta = 90°$ and $\gamma = 120°$ shown with Li adsorbed from an LYP calculation with TZ2P basis set.
b) graphene·Na: The same unit cell and calculation as Figure 3.9 is shown with Na adsorbed.

Both Na and Li adsorb over center sites of the C_6 rings in graphene. The adsorbing height, d, as defined in Figure 2.5b is reported in Angstroms. Figure 3.9a shows Li adsorption

on graphene and compares better with Kim's reference adsorbed energy of -147 kJ/mol on graphene than do our cluster results, but both still differs significantly. Our cluster results where Li adsorbs at a height of 1.621 Å with PSE= -62.4 kJ/mol agree with the corresponding SLAB results of 2.003 Å and PSE= -79.4 kJ/mol. Figure 3.9b shows the optimized SLAB of Na adsorbed on graphene. The calculated Na adsorbing heght of 2.636 Å and PSE = -35.7 kJ/mol, are comparable with reference height and PSE of 2.32 Å and -43.4 kJ/mol respectively [36].

With decorated SLABS as substrates, we are now ready to investigate their effect on H_2 adsorption. Initial calculations varying the size of the unit cell were performed starting with the unit cells from Figure 2.6 with 8, 18 and 32 carbon atoms. LYP/TZ2P Na-graphene optimizations in these cells led to corresponding PSEs of -36.3, -36.5, and -36.5 kJ/mol respectively. These three PSE values show the Na-Na interactions are small even in the 8-carbon unit cell. These results are in agreement with the reference values [36] and our cluster results. As the energy converges with the 18-carbon unit cell, these preliminary calculations were performed over a grid of 5x5x5 K-points instead of the standard 10x10x5 as in the rest of our calculations, and the unit cells were not allowed to relax to improve computational efficiency. Sufficient convergence in the energy with respect to unit cell size provide evidence to proceed, especially with the larger unit cell. These preliminary calculations were only performed on Na and not Li. The reason is if Na is not interacting with neighboring Na atoms, it is assumed that Li won't either, as it is smaller than Na. We proceed to use the larger unit cell to make room for multiple H_2 molecules to replicate a local cluster-like approximation to compare with our GAMESS results.

3.5.1 Effect of Li and Na Coadsorbates on H_2 Storage

Similar to the cluster calculations described in Section 3.4.1, the Li-graphene and Na-graphene from Figure 3.9 are SLABS used here as substrates for H_2 adsorption. To these Alkali decorated graphenes, nH_2 molecules were sequentially adsorbed from $n = 1 - 5$, optimizing the resulting SLAB upon each addition. From the optimized structures, the PSE of the n adsorbed H_2 molecules are calculated by Equation 3.1.

Figures 3.10a and 3.10b show the final optimized structures of Li-graphene and Na-graphene

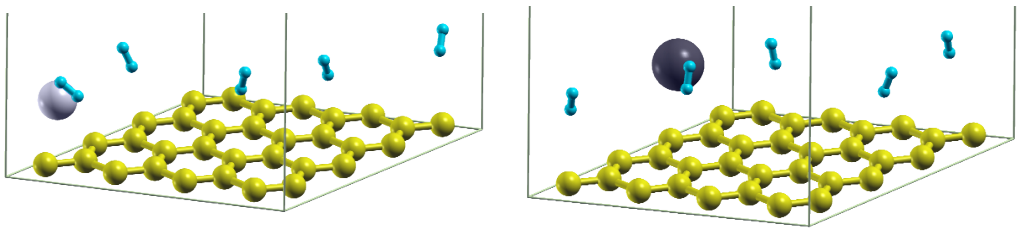

(a) $graphene \cdot Li \cdot 5H_2$ (b) $graphene \cdot Na \cdot 5H_2$

Figure 3.10: a)graphene ·Li · $5H_2$: This figure shows 5 H_2 molecules adsorbed on graphene with coadsorbed Li in a 32-carbon unit cell with $\alpha = \beta = 90°$ and $\gamma = 120°$. The entire SLAB was optimized with the LYP functional and TZ2P basis set. Resulting distances and energies are summarized in Table 3.5.
b)graphene · Na· $5H_2$: This figure shows 5 H_2 molecules adsorbed on graphene with coadsorbed Na using the same unit cell and method as in Figure 3.11. Resulting distances and energies are summarized in Table 3.5.

with 5 H_2 molecules adsorbed on each. The final structures with $5H_2$ adsorbed are only shown for the following reasons. First, the same saturation limit of H_2 adsorption is not seen in our periodic calculations because we have more carbon atoms per H_2 in our cluster calculations which also have no terminal hydrogen atoms on the substrate edge. Also, previous calculations on these systems report H_2 PSEs in terms of $5H_2$ molecules per unit cell [36, 11]. Only the lower 5 Å the 20 Å unit cell in the Z-direction is shown. Optimized adsorption heights and PSEs are summarized in the following table.

Table 3.5: Adsorption Heights and Energies for Li and Na decorated graphene calculated with SIESTA

LYP/TZ2P SIESTA Results					
Adatom	C-A	C-H	H-H	PSE(/H_2)	PSE(A·$5H_2$)
Li	2.075	3.293	0.755	-17.1	-186.7
Na	2.459	3.274	0.756	-16.1	-148.2

The first column of Table 3.5 shows the adsorption height of the adatom where A is Li·$5H_2$ or Na·$5H_2$. After the addition of $5H_2$ molecules, the C-Li height increased whereas the C-Na height decreased slightly. These values, although on the order of hundredths to thousandths of an angstrom, are interestingly not as correlated as one may expect. It is then noticed in the second and third column very similar H_2 adsorption heights and H_2 bond lengths which is consistent with the similar H_2 PSEs observed in both systems. Before decoration of the adatoms, the H_2 PSE of this system was -16.3 kJ/mol. This is seen to increase slightly with the addition of Li and not change significantly upon addition of Na.

3.6 Adatoms:Trends and Conclusions

Previous calculations suggest H_2 PSEs on Li coadsorbed graphene of -34 kJ/mol [11] and -19 kJ/mol for Na decorated graphene [36]. The cluster results of this section show H_2 PSEs of -15.3 kJ/mol on Li decorated coronene and -6.9 kJ/mol on Na decorated coronene. It is surprising that these results do not correlate better with the reference values. In particular, the calculated Na PSE on coronene of -40.2 kJ/mol matches well with the literature value of -43.4 kJ/mol [36] and for Li PSE on coronene we get -62.4 kJ/mol compared to the literature value of -147.6 kJ/mol. The present SLAB and cluster calculations do not predict a significant increase in H_2 PSE due to the coadsorption of Sodium. Both methods predict a slight to moderate increase in H_2 PSE due to the coadsorption of Lithium. In general it is observed that between Li and Na as adatoms on graphene surfaces, Li could be a better candidate for hydrogen storage applications based on it's predicted ability to increase H_2 PSE without the destruction of the substrate or need for catalysis. In addition, Lithium's lightweight provides better gravimetric capacities in a potential solid state hydrogen storage device. Continuing to compare diatomic adsorbates, the lightest combination of Alkali metals and halogens are investigated in the next section. The open shell substrates, Li-graphene and Na-graphene often lead to convergence issues and spin contamination in the wavefunction. This causes these calculations to be difficult and costly. This suggests it is likely these systems would be difficult to reproduce experimentally. A solution to this is proposed in the next section to use light halogens, F and Cl, to investigate a selection of closed shell coadsorbates.

3.7 Alkali Halide Coadosorption: Clusters

The previous section began with preliminary MP2/6-31G* geometry optimizations with first Na and then Li coadsorbed on coronene after an extensive literature review on physisorption based hydrogen storage materials. Open shell calculations to adsorb H_2 on these systems became computationally expensive, even at smaller basis sets and often ran into convergence issues. These convergence issues may be due to the single Li and Na atoms are likely to be reactive due to their unpaired electrons. This also contributes to why these systems are difficult to reproduce experimentally. The simplest solution; make the systems closed shell. The exploration with nH_2 molecules on an NaCl-coronene substrate similar to Figure 3.14d

ensued. The results were: one H_2 adsorbed with a PSE of -6.0 kJ/mol to 10 H_2 molecules with an average -3.9 kJ/mol (see Figure 3.13). Recall from Table 2.1 MP2/6-31G* PSEs range from-1 to -4 kJ/mol depending on the orientation for a single H_2 molecule on coronene. The aforementioned PSE of -6.0 kJ/mol is still a significant increase upon addition of NaCl. Also, this cluster can adsorb up to 10 H_2's while still maintaining an average H_2 PSE similar to a single H_2 on coronene. These preliminary results suggest this system could be useful for hydrogen storage and that similar coadsorbates should be investigated further.

This investigation is aimed to find the lightest possible combination of adatoms in diatomic form, that might give an increase in H_2 PSE. This section is particularly interested in LiF, LiCl, NaF, and NaCl whose structures and equilibrium bond lengths are shown below.

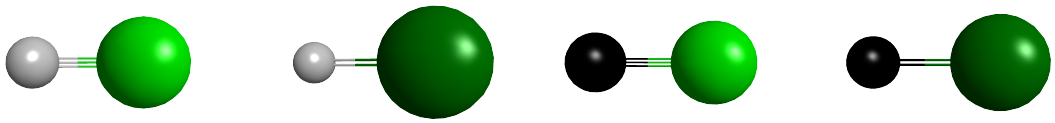

LiF LiCl NaF NaCl

(a) $\begin{matrix}1.556\\1.496\\1.564\end{matrix}$ (b) $\begin{matrix}2.058\\2.016\\2.021\end{matrix}$ (c) $\begin{matrix}1.919\\1.883\\1.926\end{matrix}$ (d) $\begin{matrix}2.376\\2.297\\2.361\end{matrix}$

Figure 3.11: The selection of diatomic molecules with corresponding equilibrium bond lengths in Å. The upper value is from a GAMESS B3LYP/6-311G(2d,p)+ optimization the middle value from a SIESTA LYP/TZ2P optimization in the same hexagonal unit cell that contained 32-carbon atoms previously. The lowest bond length listed is the accepted experimental bond length[15]. The Alkali metal is on the left of each structure.

This equilibrium bond lengths shown above in Figure 3.11 show good agreement between our cluster and SLAB calculations and with experimental values [15]. These diatomics are first adsorbed on coronene to produce a new substrate for H_2 adsorption. To these new substrates $n = 1 - 5$ H_2 molecules will be sequentially adsorbed and the PSE values and adsorption heights at each step are calculated. The selection of lightweight Alkali Halides are all closed shell molecules, as is the coronene substrate they are being adsorbed to. This makes these calculations easier to do than the Li/Na open shell calculations. To our knowledge, this series of calculations has not been previously performed and could provide novel ideas for a solid state hydrogen storage device. To begin, the optimized structures of

the Alkali Halide coadsorbates on coronene are shown below with the corresponding heights, distances and adsorption energies in Table 3.6.

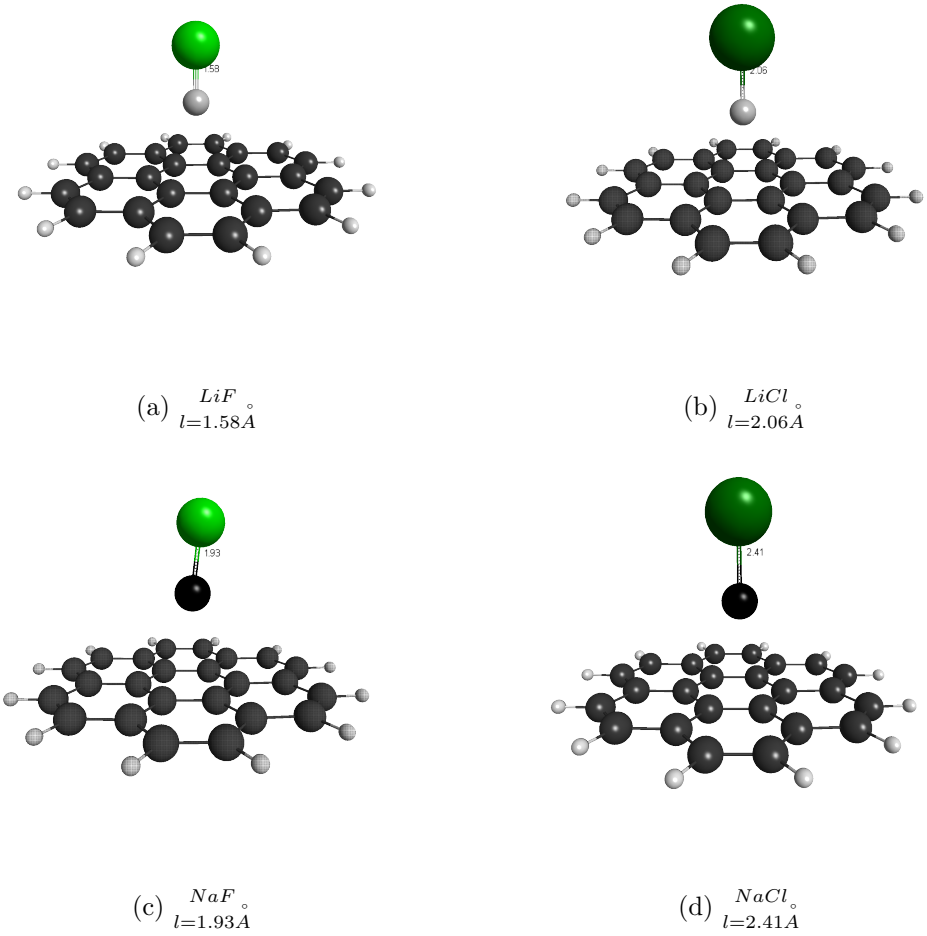

(a) $\underset{l=1.58\mathring{A}}{LiF}$ (b) $\underset{l=2.06\mathring{A}}{LiCl}$

(c) $\underset{l=1.93\mathring{A}}{NaF}$ (d) $\underset{l=2.41\mathring{A}}{NaCl}$

Figure 3.12: The selection of alkali halide molecules adsorbed on coronene. Al structures are fully optimized with the B3LYP-D functional and 6-311G(2d,p)+ basis set. adsorption energies and bond distances are seen in Table 3.6 for both the B3LYP-D and MP2 optimizations. Alkali Halide bond lengths, l, in the final structures are shown in the figures a-c in units of Angstroms.

Table 3.6: Alkali Halide Distances and Adsorption Energies

6-311G(2d,p)+ GAMESS Results on coronene					
Method	Adsorbate	C-C AVG	C-C STDEV	Height Å	PSE kJ/mol
B3LYP	none	1.410	0.022	0	0
MP2	none	1.411	0.019	0	0
B3LYP-D	LiF	1.410	0.022	2.345	-55.1
MP2	LiF	1.412	0.019	2.201	-71.2
B3LYP-D	LiCl	1.410	0.022	2.251	-64.8
MP2	LiCl	1.412	0.019	2.105	-73.9
B3LYP-D	NaF	1.413	0.022	2.503	-62.9
MP2	NaF	1.416	0.019	2.415	-56.8
B3LYP-D	NaCl	1.410	0.022	2.494	-65.2
MP2	NaCl	1.410	0.020	2.440	-56.7

The last column of Table 3.6 shows the adsorption energy of the selected diatomic on coronene. The second to last column shows the adsorbing height to the Alkali metal of the Alkali Halide. The B3LYP-D optimized bond length of the coadsorbed Alkali Halides are shown in Figures 3.11 and 3.12 in units of Angstroms. All of the coadsorbants adsorb with the Alkali metal closest to center site of coronene in a perpendicular configuration. An interesting result right away is the difference between the B3LYP-D and MP2 results. First, the percentage of dispersion to the total energy in LiF and NaF is small at 0.004% and smaller for LiCl and NaCl at 0.003% in the DFT calculations. This small contribution important as its inclusion can still change H_2 PSEs from positive to negative values when a dispersion term is included in the final energies. For LiF and LiCl the MP2 PSEs increase in magnitude by roughly 10 kJ/mol. For NaF and NaCl, the opposite trend is observed and the MP2 PSEs decrease in magnitude by 5-10 kJ/mol. This is a surprising result. Also inconsistent with previous results is the adsorption height as seen in the penultimate column. This height is to the atom lowest to the coronene plane, which is Li or Na. Typically, as we have seen, a shorter distance is associated with a higher PSE. This is observed in LiF and LiCl but not in NaF and NaCl. In Figure 2.11, we used the same MP2 and B3LYP-D methods to calculate the adsorption energies of a range of small molecules of various polarity and the results showed good agreement among the two methods in all cases. The present change in results with the same methodology may be a result of these diatomic molecules being of a different chemical nature than the selection of small molecules investigated in Chapter 2. This issue will be returned to later and for now we continue to use both methods side by side.

Included along with the average C-C distances of the substrate with standard deviations are shown to 0.001 Å. The reason for this is to try and see and subtle changes in the carbon framework of the substrate over time. In pure coronene, our average B3LYP C-C distance is 1.410 Å . The average C-C in the central ring of this structure is 1.424 Å and in the outer ring structures ranges from 1.367-1.420 Å . We know that the ring in the center of coronene is that of graphene, 1.420 Å and gets shorter on the edges due to the terminal hydrogen atoms breaking aromaticity. Depending on the adsorbate added, the carbon framework relaxes slightly and can become corrugated. The average bond lengths and standard deviations are therefore included to 0.001 Å to see if any minute changes to the substrate are changed during adsorption. Note for the B3LYP-D calculations all of the average C-C distances remain the same except for with NaF. This change is very small and would go unnoticed if not for the precision these values are reported. Recall from Chapter 2, when a hydrogen atom was chemisorbed atop a carbon atom in pyrene, the average C-C distance of the pyrene substrate did not significantly change. The carbon atom involved in chemisorption in this case did relax to 0.41 Å from its original position which was reflected as the standard deviation of the C-C distance increased from 0.022 to 0.038 Å . In Table 3.6, we can see the C-C standard deviation does not change upon adsorption of any of the Alkali Halides. B3LYP-D results show that upon adsorption to the coronene substrate, the internuclear distance of LiCl does not change but the remaining three Alkali Halides all showed a slight increase in bond length on the order of hundredths of an Angstrom after the adsorption process. MP2 calculations appear to be more sensitive to the adsorbed substrate and also associates the largest change in the carbon framework as a result of NaF adsorption. In the next section we will keep an eye on these bond lengths and see if they change after H_2 adsorption.

3.7.1 Effect of Alkali Halide Coadsorption on H_2 Storage: Clusters

The preliminary MP2/6-31G* calculations investigating multiple H_2 adsorption on our selection of diatomic molecules adsorbed on coronene typically allowed n to range from 1 to 5 on the clusters before the entire system was optimized. With NaCl as a coadsorbant, n was increased to 10, as shown below.

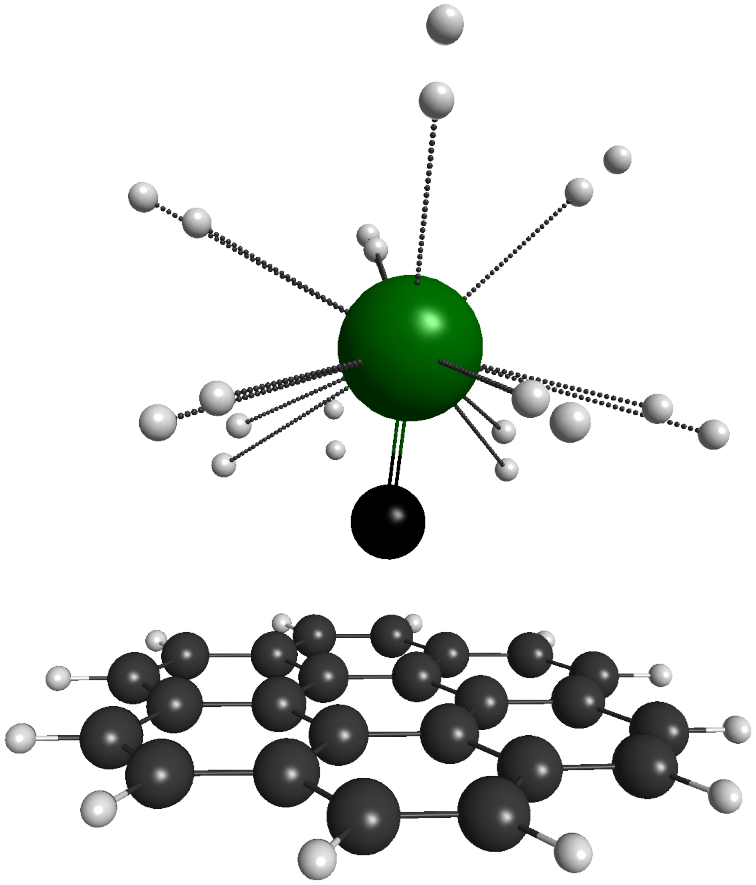

Figure 3.13: $C_{24}H_{12}$·NaCl·10H_2: The MP2 optimized structure using the 6-31G* basis set of coronene coadsorbed with NaCl and 10 H_2 is shown. The 10 H_2 molecules are arranged in a specific geometric arrangement with multiple C_6 axes about the Cl atom. The Na is sitting atop the center site of coronene at a height of 1.653 Å with a bond to Cl of 2.447 Å and an angle of 17° from the vector normal to the plane of the carbon atoms.

Figure 3.13 shows 10 H_2 molecules adsorbed to the NaCl substrate. The PSE averaged over these 10 H_2 molecules is -3.9 kJ/mol. Calculated with the MP2 method and 6-31G* basis set, this is an increase from the PSE of a single H_2 adsorbed to plain coronene as calculated with the same method and basis set. Although this is not a significant increase, NaCl is observed to adsorb a high number of H_2 moecules per NaCl coadsorbant which increases the gravimetric capacity of the system. More importantly, these allowed a clear picture of the optimal adsorption location for a single H_2 molecule on each cluster. This can be seen by analysis of the structures, as the highest PSE typically corresponds to the closest distance to both the coronene plane and the coadsorbant. The summary of these preliminary results showed MP2/6-31G* PSEs of H_2 on coronene decorated with LiF, LiCl,

NaF and NaCl to be -8.6,-6.2,-18.0, and -6.3 kJ/mol respectively. These structures were then taken as starting geometries for B3LYP-D/6-311G(2d,p)+ and MP2/6-311G(2d,p)+ optimizations. The resulting optimized structures are shown in Figures 3.14 to 3.20 below with their corresponding H_2 binding energies.

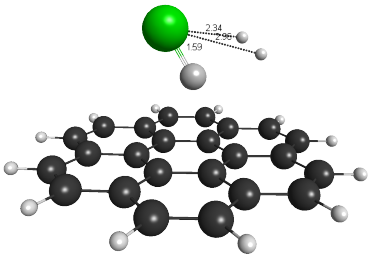

LiF

(a) $\begin{matrix}-15.2\\-14.4\end{matrix}$

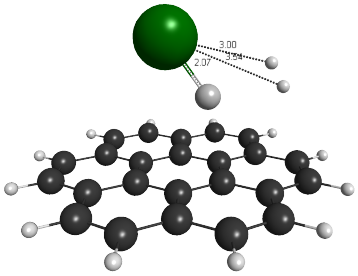

LiCl

(b) $\begin{matrix}-14.6\\-16.1\end{matrix}$

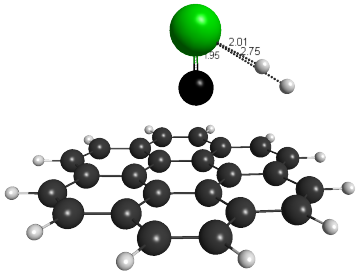

NaF

(c) $\begin{matrix}-21.6\\-16.7\end{matrix}$

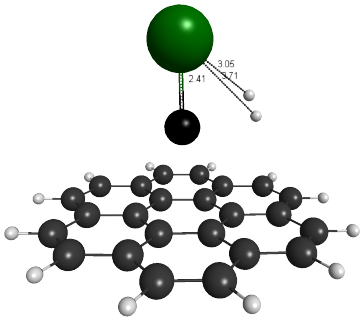

NaCl

(d) $\begin{matrix}-12.4\\-11.7\end{matrix}$

Figure 3.14: LiF, LiCl, NaF, and NaCl with adsorbed H_2. The upper value is the B3LYP-D PSE and the lower MP2 PSE both in kJ/mol calculated with 6-311G(2d,p)+ basis set. Associated distances are shown on the structures in units of Angstroms. The Alkali Halide bond lengths and H-Halide distances are also shown.

The single H_2 PSEs given in Figure 3.14 show reasonable agreement between B3LYP-D (upper value) and MP2 methods (lower value) at the 6-311G(2d,p)+ basis set level. Upon adsorption on graphene the Alkali Halide, the equilibrium bond length of LiF increased by 0.03 Å, of LiCl increased by 0.01 Å, of NaF increased by 0.03 Å, and of NaCl by 0.03 Å. Not shown in the figures is the distance between the carbon plane and the Alkali metal. For LiF, LiCl, NaF, and NaCl these heights are 2.092, 2.282, 2.229, and 2.551 Å respectively. After the adsorption of a single H_2 molecule, the heights of the coadsorbed Alkali Halides decreased for both LiF and NaF by 0.25 and 0.27 Å respectively (see Table 3.6). The adsorbing height of LiCl and NaCl after the addition of a singe H_2 increased slightly by 0.03 Å and 0.06 Å respectively. This suggests part of the reason for increased H_2 PSE in the fluorinated compounds is by an increased interaction of the diatomic coadsorbate with the substrate.

The reason that 6-31G* results are mentioned is to show how the PSEs change as the basis set size is increased. We find increased PSEs seen in the LiF, LiCl, and NaCl cases to be quite large but may be expected as we typically see larger binding energies with larger basis sets. The weak nature of H_2's interaction with the substrate and the need for diffuse functions to accurately obtain PSEs lead us to use relatively large basis sets. Of particular interest is the initial NaF result. With the 6-31G* basis set, the use of NaF as a coadsorbant increased H_2 PSE to -18.0 kJ/mol. When the basis set was increased to 6-311G(2d,p)+, which we know more accurately depicts H_2 physisorption, the resulting H_2 PSE is increased even further to -21.6 kJ/mol. This is a significant increase but not as large in comparison to the LiF coadsorbant whose 6-31G* H_2 PSE of -8.6 kJ/mol increased to -15.2 kJ/mol when the basis set was increased from 6-31G* to 6-311G(2d,p)+. At both basis sets and in both methods, this suggests that both LiF and NaF are good candidates for H_2 storage via a physisorption mechanism. To further see the effect of these coadsorbates on H_2 physisorption, we now take each of the structures from Figure 3.15 and sequentially add H_2 molecules and optimize the new structures until negative frequencies are observed or the structures suggest a reduction in the H_2 PSE. The final structures presented include the maximum number of adsorbed H_2 before any negative frequencies are observed. Beginning with the lightest case of LiF the largest number of adsorbed hydrogens without any negative frequencies occurs to n=2.

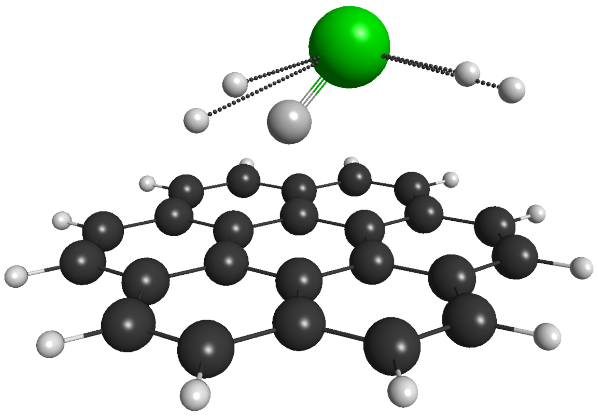

Figure 3.15: $C_{24}H_{12} \cdot LiF \cdot 2H_2$:
B3LYP-D/6-311G(2d,p)+:This figure shows LiF coadsorbed with the maximum number of H_2 molecules on coronene. The calculated vibrational frequencies are all positive, the lowest occurs at 23.5 cm^{-1}.

Table 3.7: LiF decorated coronene with 2 adsorbed H_2:
Adsorption energies and distances for LiF coadsorbed with $2H_2$ molecules on coronene are presented. The first row of this table corresponds to the accompanying figure.

GAMESS Results:$C_{24}H_{12} \cdot LiF \cdot 2H_2$				
Method	D	Å	PSE	kJ/mol
B3LYP	C-C	1.410	/H_2	-15.3
-D	C-Li	2.081	LiF· $2H_2$	-59.9
	C-H	3.116		
	Li-H	2.589		
	F-H	2.617		
	H-H	0.752		
MP2	C-C	1.412	/H_2	-14.9
	C-Li	2.025	LiF· $2H_2$	-65.8
	C-H	2.866		
	Li-H	2.229		
	F-H	2.904		
	H-H	0.745		

Figure 3.15 shows the final optimized H_2 adsorption on LiF-coronene. LiF is shown adsorbed to the center site of coronene. The distance from the carbon sheet to the Li atom is 2.081 Å with an LiF bond length of 1.599 Å pointing 36° off the normal vector to the plane of the carbon atoms. In the final optimized structure, the LiCl distance is 0.01 Å larger that

in the singly adsorbed structure of Figure 3.14a and 0.02 Å larger than with no adsorbed H_2 molecules in Figure 3.12a.

LiF is shown to increase the magnitude of the H_2 PSE to -15.3 kJ/mol as a result of 2 adsorbed H_2 molecules. This is a slight increase from the PSE of a single H_2 molecule, a result shared by both methods. Looking at the above structure shows one H_2 molecule closer to the Li atom, at 2.068 Å, lowering the average distance to 2.589 Å, seen in Table 3.7. It is usually the case that the closer molecules physisorb with a higher energy. The overall H_2 PSE is due to weak interactions between the H_2 molecule and the carbon framework. The overall interaction energy between the Li·$2H_2$ and coronene is relatively weak at -59.9 kJ/mol. It is an expected result then that the average C-C distance in the carbon framework of the substrate remains unchanged at 1.410 Å from the fully planar coronene structure. The same analysis of the MP2 bond lengths shows a slight increase, although not significant, in average C-C distance due to the -65.8 kJ/mol interaction. The low energies associated with the overall interaction energy show that the carbon framework is stable throughout this interaction.

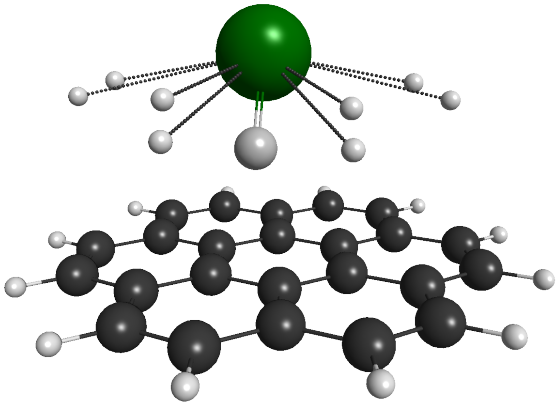

Figure 3.16: Optimized $C_{24}H_{12}$·LiCl·$4H_2$:B3LYP-D/6-311G(2d,p)+ This figure shows LiCl coadsorbed with the maximum number of H_2 molecules on coronene. The lowest calculated vibrational frequency is 14.6 cm^{-1}.

Table 3.8: LiCl decorated coronene with 4 adsorbed H_2:
Adsorption energies and average distances for LiCl with $2H_2$ molecules on coronene are summarized here. The first row of this table corresponds to the accompanying figure.

GAMESS Results: $C_{24}H_{12}$ · LiCl · $4H_2$				
Method	D	Å	PSE	kJ/mol
B3LYP	C-C	1.410	/H_2	-11.7
-D	C-Li	2.309	LiCl·$4H_2$	-74.6
	C-H	3.113		
	Li-H	2.782		
	Cl-H	3.254		
	H-H	0.749		
MP2	C-C	1.412	/H_2	-11.6
	C-Li	3.429	LiCl·$4H_2$	-87.3
	C-H	2.963		
	Li-H	3.027		
	Cl-H	3.411		
	H-H	0.744		

Figure 3.16 shows the final LiCl-coronene optimized structure containing 4 H_2 molecules. LiCl is shown adsorbed to the center site of coronene. The H_2 molecules adsorb to center sites of the outer rings of coronene and the Alkali side of the LiCl. The distance from the carbon sheet to the Li atom is 2.309Å with an LiCl bond length of 2.085 Å pointing 44° off the normal vector to the plane of the carbon atoms. In the final optimized structure, the LiCl distance is is 0.015 Å larger that in the singly adsorbed structure of Figure 3.14b and 0.025 Å larger than with no adsorbed H_2 molecules in Figure 3.12b.

Figure 3.16 and Table 3.8 show the final H_2 adsorption on LiCl-coronene. LiCl is shown to increase the magnitude of the H_2 PSE to -11.7 kJ/mol as a result of 4 adsorbed H_2 molecules. Consistent with the LiF results, the carbon framework is stable throughout this process, shown to increase only slightly after adsorption of the coadsorbate and H_2's in the MP2 calculations. The H_2 PSE is shown to increase in magnitude to -11.7 kJ/mol as a result of 4 H_2 molecules cointeracting with the adsorbed LiCl. This is a decrease however from a single H_2 on LiCl-coronene as seen in Figure 3.15b. When viewed from a top-down perspective, the individual H_2 molecules can be seen approaching the center cites of the outer rings of coronene, close the optimal adsorption distance of around 3 Å from the both Li and Cl atoms, and coronene.

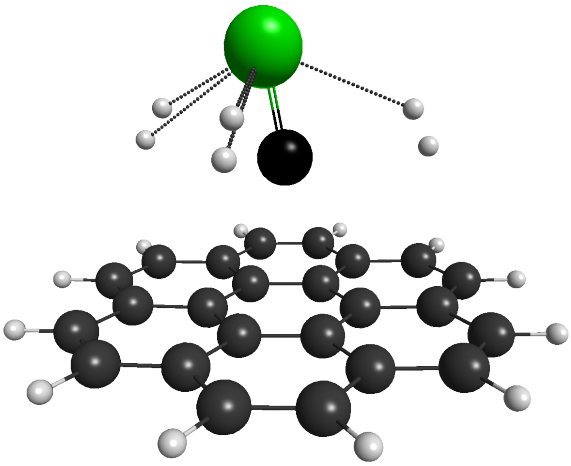

Figure 3.17: $C_{24}H_{12}$* · NaF · $3H_2$:
This figure shows NaF coadsorbed with the optimized with B3LYP/6-311G(2d,p)+ with maximum number of H_2 molecules on coronene. The calculated vibrational frequencies are all positive, the lowest occurs at 24.8 cm^{-1}.

Table 3.9: NaF decorated coronene with 3 adsorbed H_2:
This table summarizes adsorption energies and average distances for NaF with $3H_2$ molecules on coronene. The first row of this table corresponds to the accompanying figure.

GAMESS Results: $C_{24}H_{12}$ · NaF · $3H_2$				
Method	D	Å	PSE	kJ/mol
B3LYP	C-C	1.413	/H_2	-17.8
-D	C-Na	2.069	NaF·$3H_2$	-71.3
	C-H	2.934		
	Na-H	2.580		
	F-H	2.710		
	H-H	0.753		
MP2	C-C	1.412	/H_2	-15.3
	C-Na	2.261	NaF·$3H_2$	-65.3
	C-H	2.764		
	Na-H	2.556		
	F-H	2.840		
	H-H	0.746		

Figure 3.17 shows the final NaF-coronene optimized structure containing 3 H_2 molecules. Looking down the Z-axis towards the plane of the carbon atoms, two of the three adsorbed hydrogen molecules are atop center sites of the outer rings of coronene. NaF is adsorbed to the center site of coronene. The distance from the carbon sheet to the Na atom is 2.069 Å with an NaF bond length of 1.966 Å pointing 13° off the normal vector to the plane of the carbon atoms. The bond length of the coadsorbate in this case has stretched 0.04Å from its original length as seen in Figure 3.12c after the addition of the three hydrogen molecules.

NaF is shown to increase the magnitude of the H_2 PSE to -17.8 kJ/mol as a result of 3 adsorbed H_2 molecules. Two of these three H_2 molecules are closer to the Na atom than the carbon framework, which could be contributing the large observed H_2 PSEs observed with the NaF decorated systems we have observed. Even with the relatively low interaction energy of the NaF·3H_2 subcluster, there is a slightly larger increase in the average C-C distance here than with the other clusters investigated. There is a small amount of discrepancy here however. The B3LYP-D results show an average C-C of 1.413 Å both before and after H_2 adsorption. The same MP2 results, which have been shown to be more sensitive to geometry changes in these systems, relaxed from 1.416 to 1.412 Å after addition of H_2's. Both of these methods still show the largest change in C-C bonding before H_2 adsorption, and NaF should likely be further investigated for this reason. Still, the low PSEs of coronene and the remaining subcluster combined with the increased H_2 PSEs show that NaF could be a logical candidate for a solid state hydrogen storage system based on physisorption principles.

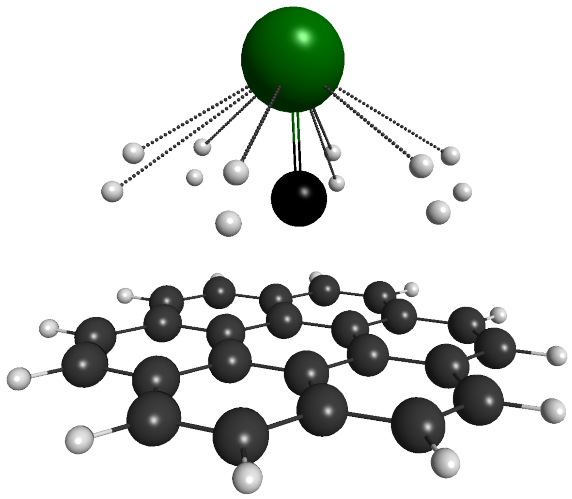

Figure 3.18: $C_{24}H_{12} \cdot NaCl \cdot 6H_2$:
This figure shows the final B3LYP-D/6-311G(2d,p)+ optimized structure of NaCl coadsorbed with the maximum number of H_2 molecules on coronene. The calculated vibrational frequencies are all positive, the lowest occurs at 24.9 cm^{-1}.

Table 3.10: NaCl decorated coronene with 6 adsorbed H_2:
Adsorption energies and average distances for LiCl with $2H_2$ molecules on coronene are summarized here. The first row of this table corresponds to the accompanying figure.

GAMESS Results: $C_{24}H_{12} \cdot NaCl \cdot 6H_2$				
Method	D	Å	PSE	kJ/mol
B3LYP	C-C	1.413	$/H_2$	-10.3
-D	C-Na	2.617	$NaCl{\cdot}6H_2$	-90.5
	C-H	3.024		
	Na-H	2.989		
	Cl-H	3.568		
	H-H	0.745		
MP2	C-C	1.417	$/H_2$	-8.1
	C-Na	2.543	$NaCl{\cdot}6H_2$	-86.4
	C-H	3.062		
	Na-H	3.011		
	Cl-H	3.516		
	H-H	0.740		

Figure 3.18 shows the final optimized Alkali Halide coadsorption structure of 6 H_2 molecules

on NaCl-coronene. Looking down the Z-axis towards the plane of the carbon atoms, all six of the adsorbed hydrogen molecules are adsorbed above the center sites of the outer rings of coronene. NaCl is adsorbed to the center site of coronene. The distance from the carbon sheet to the Na atom is 2.617 Å with an NaCl bond length of 2.429 Å pointing 6° off the normal vector to the plane of the carbon atoms. The bond length of the coadsorbate in this case has stretched 0.02 Å after the addition of the six hydrogen molecules from its initial structure in 3.12d.

NaCl is shown to increase the magnitude of the H_2 PSE to -10.3 kJ/mol as a result of 6 adsorbed H_2 molecules. Looking at this structure from the top-down view shows each H_2 adsorbing atop a center site of an equivalent outer ring of coronene. These adsorbed molecules are at near optimal heights and positions with respect to the carbon framework at almost precisely 3 Å and even closer to the Na atom, both interactions contributing to the calculated PSEs. The interacting energy of the B subcluster on coronene in this system is approaching -100 kJ/mol which is when chemisorption begins to take place, so changes in the carbon framework should be monitored. Before the addition of any H_2 molecules, both methods gave average C-C bond lengths of 1.410 Å which both increased after the addition of $6H_2$. Particularly to the MP2 results, there was the smallest detectable decrease from 1.411 to 1.410 Å during the process of NaCl adsorption. After H_2 adsorption this value increased to 1.417 Å , one of the largest observed changes in this section.

Alkali Halide Coadsorbates for use in hydrogen Storage Systems

Our calculations suggest that alkali halides should be further investigated experimentally for hydrogen storage applications. Both LiF and NaF, despite their lightweight, could be potential candidates to increase hydrogen storage capacities with their large H_2's PSEs without altering the carbon substrate. All clusters held multiple H_2 molecules distributed evenly around each adsorbed diatomic molecule. In both LiCl and NaCl, the ability to adsorb multiple H_2 molecules was greater than in the former two candidates despite their lower in comparison predicted H_2 PSE when compared to LiF and NaF. The overall disruption in the carbon framework in all four clusters investigated is minimal, and bond lengths in all adsorbed H_2 molecules are not indicative of dissociation. These results show that these systems could be used to increase H_2 PSEs. To further confirm this, the preceding

investigation of coadsorbates effect on H_2 physisorption was replicated in a SLAB approach using SIESTA, the results of which are briefly presented in the proceeding section.

3.8 Alkali Halide Coadsorption: SLABS

IN this section we apply SLAB calculations to examine how diatomic alkali halide molecules influence H_2 adsorption in graphene usin the same procedures as described in Sections 2.4 and 3.5. We first calculate the adsorption energies of the four selected Alkali Halide diatomics on graphene.

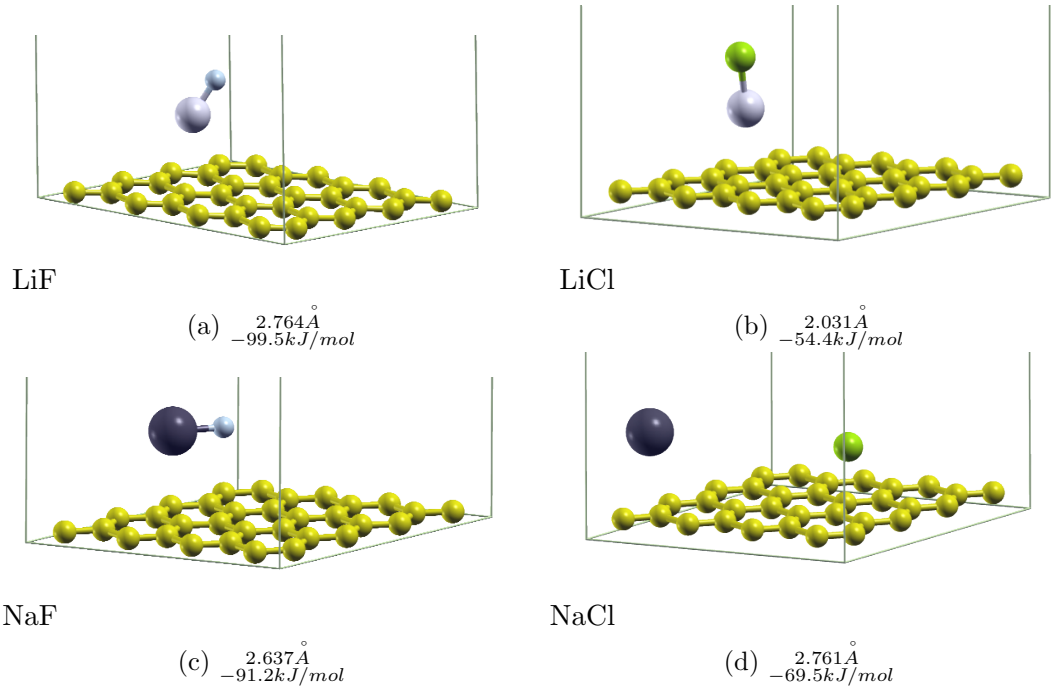

(a) $\underset{-99.5kJ/mol}{2.764\mathring{A}}$ (b) $\underset{-54.4kJ/mol}{2.031\mathring{A}}$

(c) $\underset{-91.2kJ/mol}{2.637\mathring{A}}$ (d) $\underset{-69.5kJ/mol}{2.761\mathring{A}}$

Figure 3.19: The selection of diatomic molecules optimized on graphene with the LYP functional and TZ2P basis set. The corresponding adsorbing heights are shown in Angstroms and the corresponding binding energy is reported in kJ/mol.

The four alkali halide adsorption structures on graphene are shown in Figure 3.19. The corresponding adsorption heights in the above substrates give mediocre agreement with our cluster results, yet the PSEs from the SLAB calculations do not give good agreement. The SLAB calculations suggest LiCl and NaCl adsorb with greater energy than LiF and NaF. The cluster calculations give the opposite PSE trend prior to H_2 adsorption. The general

range of PSEs in the cluster results of -55 to -74 kJ/mol are roughly in the same range as the -54 to -100 kJ/mol of the SLAB results with the fluorine compounds being significantly lower than expected. It is likely the same issue causing this overestimated H_2-graphene interactions in the present SIESTA results.

3.8.1 Effect of Alkali Halide Coadsorbates on H_2 Storage: SLABS

Following Sections 3.3 and 3.5.1 we now proceed to test the effects adsorbing LiF, LiCl, NaF, and NaCl on H_2 PSEs calculated sequentially from $n = 1 - 5$ and calculating the adsorption per H_2 molecule for each of th final structures.

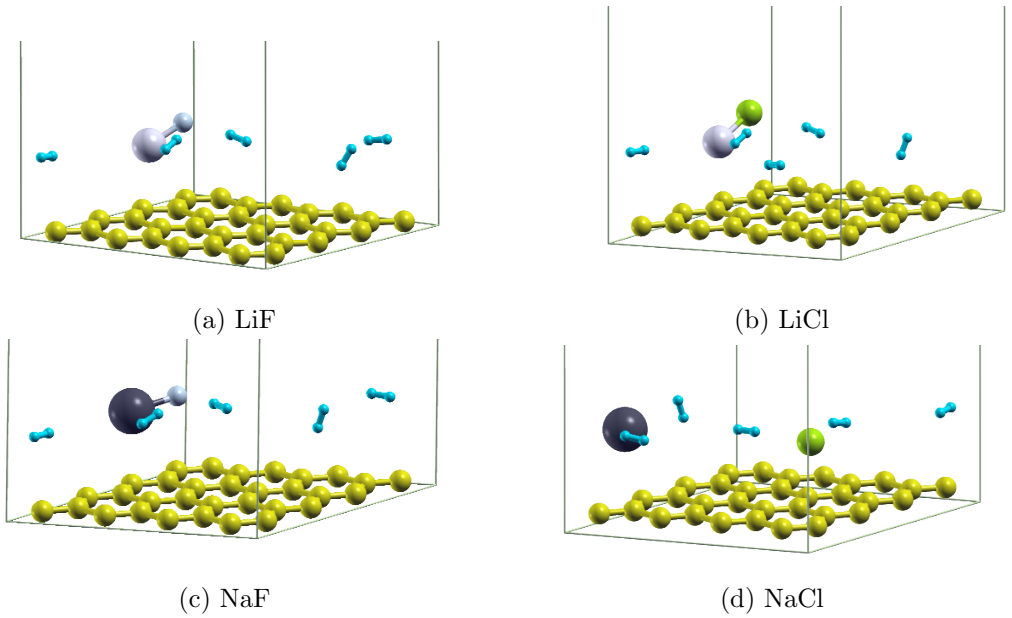

(a) LiF (b) LiCl

(c) NaF (d) NaCl

Figure 3.20: The selection of diatomic molecules and their final optimized structures with 5 adsorbed H_2 molecules optimized with LYP/TZ2P.

Table 3.11: Physisorption energies of diatomically decorated graphene with $5H_2$ molecules adsorbed.

LYP/TZ2P SIESTA Results: graphene·$5H_2$					
coadsorbate	C-A	C-H	H-H	PSE(/H_2)	PSE(A)
LiF	2.489	3.685	0.759	-33.5	-101.8
LiCl	2.949	3.840	0.757	-30.0	-107.5
NaF	2.697	3.284	0.762	-42.8	-107.7
NaCl	2.870	3.916	0.759	-32.2	-105.2

In the above table A represents the coadsorbate and $5H_2$ molecules. The interaction energy of this subcluster does not vary much from the different systems studied, especially considering the variation observed before and after H_2 adsorption. A general trend can be read from these results suggesting coadsorption of NaF increases H_2 PSE the most followed by LiF then NaCl and LiCl. The trends of the fluorine containing compounds follow those of the cluster results. In the cluster results, LiCl increases H_2 PSE in magnitude by -1.1 kJ/mol when compared to that of NaCl at the limit when $6H_2$ molecules are adsorbed. The same trend is observed in the clusters with one H_2 adsorbed with LiCl having a PSE -2.2 kJ/mol greater in magnitude than NaCl. We find that SIESTA calculations are incorrectly showing this trend with the Cl containing compounds. It is thought that the pseodopotentials may need to be revisited. Nonetheless, the SLAB calculations suggest that diatomic alkali halides might improve H_2 storage on graphene by means of increasing physical adsorption energies.

Coadsorbates use in hydrogen Storage Systems: Revisited

In all four of the investigated coadsorbates in this section, similar to our cluster calculations, the SLAB calculations suggest there is reason for further investigation of these systems for hydrogen storage applications. Of particular interest the SLAB calculations indicate the H_2 PSE increases when LiF and NaF are coadsorbed to a graphene surface.

3.9 Discussion

In this Chapter it was found that 4 H_2 molecules can physically adsorb to center sites of the outer ring of coronene maintaining an average physisorbed energy of -6.1 kJ/mol in good agreement with Pantha and Belbase' result of -6.6 kJ/mol who used periodic DFT calculations with 5 H_2's in a hexagonal unit cell of 18-carbon atoms as in Figure 2.6b [36]. Na was then adsorbed to coronene with an associated energy of -40.2 kJ/mol which also compares well with the literature value of -43.4 kJ/mol [36]. Li was then adsorbed to coronene with a corresponding binding energy of -62.4 kJ/mol which is significantly less than the literature value of -147.6 kJ/mol calculated by Kim et al. who used periodic DFT calculations an a 32-carbon unit cell as in Figure 2.6c and the one in the present

SLAB calculations[11]. Binding energies of H_2 on Na and Li decorated coronene were not predicted to significantly increase from those on their pure coronene counterpart. This is likely due to the weak nature of these dispersion based interactions to have multiple local minima on their corresponding potential energy surfaces. For instance Figure 1.1 shows the existence of a metastable chemisorbed state around 1.5 Å that is a local minima but has a positive binding energy depending on the corrugation in the carbon framework of the coronene. During many geometry cycles during the course of this research, positive binding energies were encountered, Most often these were UHF calculations for the physisorption energy of the subcluster of coadsorbed atom or diatomic and H_2 molecules. This is a result of either this portion of the cluster wanting to move away from the coronene substrate, or a result of one of these metastable chemisorbed states [31] or due to the shallow nature of the physisorption energy wells around 3 Å that can give rise to low diffusion barriers.

In the second part of this chapter, simple Alkali Halide combinations were coadsorbed on coronene and their geometries and effect on H_2 physisorption were analyzed. To our knowledge these calculations have not been performed before. The results, true to both cluster and SLAB methods, suggest the use of LiF, LiCl, NaF, and NaCl as coadsorbed coadsorbates all increase H_2's interacting energy compared to on pure coronene. In the case of LiF and NaF the binding energies increased to nearly -20 kJ/mol which is not at a desired value of -100 kJ/mol but is a step towards bridging the gap between using rare and heavy transition metals to abundant, light coadsorbates that could potentially provide a clean solution for storing hydrogen in a solid state device designed on physisorption principles. As hydrogen approaches graphene, there is an induced dipole moment in the hydrogen molecule causing an attraction due to overlap in the σ-orbitals of the hydrogen and the π system of graphene [44]. To further investigate the cause of increased H_2 PSE in our Alkali Halide coadsorbant systems, we look to the dipole and quadrupole moments of the selected Alkali Halides.

3.9.1 Multipole Analysis

In general electrostatics, multipoles describe a distribution of point charges. In chemistry, we are familiar with dipoles, as a way to describe the polarity of a molecule. The electrostatic analogy of this is a positive and negative charge. A quadrupole mass analyzers provide a simple visual of a quadrupole, a square with alternating positive and negative charges at the corners with no net dipole moment. In general, the 2^n-pole moment of any arbitrary charge distribution can be defined by an nth rank symmetric tensor [29].

$$M^n = \sum_i e_i r_i^n Y^n(r_i) \tag{3.3}$$

With the nth rank tensor operator Y^n is defined as

$$Y^n(r_i) = \frac{-1^n}{n!} r_i^{n+1} \nabla^n \frac{1}{r_i} \tag{3.4}$$

Where e_i is the ith electric charge with radius vector r_i. The multipole potential energy is given by the expansion

$$U(E) = -\sum_{n=0}^{\infty} \frac{2^n n!}{(2n)!} M^n[n] E^n \tag{3.5}$$

Where [n] represents an n-fold contraction of the product of the two nth rank tensors M^n and E^n [29]. When n=0 you have a dimensionless monopole, when n=1 you have a dipole, n=2 a quadrupole etc. The dipole moment $\mu = q \cdot d$ has units of Debyes, where a Debye is about 3 x 10^{-30} Coulomb meters. Quadrupoles therefore have units of Debye·Å also called Buckinghams.

After a Hartree Fock self consistent field procedure converges, the result is a ground state estimate to the total electron density given by Equation 1.34. In particular, the Coulomb matrix elements J, involve a continuous charge distribution defined by the basis functions. From the density matrix, one can calculate post SCF values such as Mulliken and Löwdin population analysis. Also from the converged density matrix a multipole expansion analysis can be carried out to calculate monopole, dipole, quadrupole, etc. moments. These quantities converge readily after a typical energy calculation [32, 18]. To our selection of diatomics from the last section, we present the following multipole expansion results, all calculated using MP2/6-31G*.

Table 3.12: H_2 Physisorption energies and multipole moments of isolated diatomics

GAMESS Multipole Moments: MP2/6-31G*			
Coadsorbate	Dipole (Debye)	Quadrupole (Debye·Å)	PSE /H_2 kJ/mol
LiF	5.86	6.57	-8.61
LiCl	7.31	14.84	-6.24
NaF	7.82	0.146	-18.0
NaCl	9.64	8.76	-6.28

Table 3.12 shows the double zeta level perturbation theory results of LiF, LiCl, NaF, and NaCl. Included is the physisorption energy of H_2 as a result of the corresponding diatomic coadsorbed to coronene. From these results the reason for NaF's predicted ability to increase H_2 adsorption energies could be due to its significantly low quadrupole moment of 0.146 Debye·Å as seen above. This does not explain however, similar observations in LiF-coronene as the same calculated quadrupole momoent in LiF is 6.57 Debye·Å . The same multipole moments are calculated with the 6-311G(2d,p)+ basis set.

Table 3.13: H_2 Physisorption energies and Multipole moments of isolated diatomics

GAMESS Multipole Moments: MP2/6-311G(2d,p)+			
Coadsorbate	Dipole (Debye)	Quadrupole (Debye·Å)	PSE /H_2 (kJ/mol)
LiF	6.38	7.66	-14.4
LiCl	7.23	17.11	-16.1
NaF	7.76	0.20	-16.7
NaCl	9.20	8.76	-11.7
H_2	0.00	0.72	-6.1

The above table shows the quadrupole moments all of our closed shell coadsorbates including H_2. The calculated moments are of the isolated molecules, the corresponding H_2 PSEs when the coadsorbates are present are included. For further analysis, the quadrupole moments of these adsorbing species, as well as coronene and H_2 are all looked at before and after each is adsorbed to coronene. The reported PSE is of the corresponding adsorbate on coronene.

Table 3.14: Multipole moments of selected coronene with various coadsorbates

GAMESS Multipole Moments: MP2/6-311G(2d,p)+			
Coadsorbate	Dipole (Debye)	Quadrupole (Debye*Å)	PSE (kJ/mol)
coronene	0.00	38.31	n/a
LiF	6.83	84.74	-71.2
LiCl	7.14	80.99	-73.9
NaF	9.40	110.84	-56.8
NaCl	11.30	126.75	-56.7
H_2	0.06	38.43	-6.1

Table 3.14 shows the quadrupole moments of the final MP2 optimized structures of coronene by itself and with the coadsorbates before the addition of H_2. The multipole moments are also included for H_2 adsorbed on plain coronene for comparison. All of the Alkali Halides induce a quadrupole moment in the final cluster. Planar coronene, with no adsorbates, has no dipole moment and a quadrupole moment of 38.31 Debye·Å. When H_2 physisorbes to coronene, the quadrupole moment of the resulting cluster is 38.43 Debye·Å. Less than the sum of H_2 and coronene's individual quadrupole moments. In the case of NaF, the initial sum of the quadrupole moments is 38.51 Debye·Åwhich increases to 110.84 Debye·Å after adsortption. It seems likely this large induced quadrupole moment is in turn responsible for the large increase in H_2 PSE when NaF is used as a coadsorbant. As H_2 physisorbs to graphene a dipole moment is induced in the hydrogen molecule and interacts with coronene through a dipole-quadrupole interaction. It was mentioned previously that high hydrogen adsorption results from ion-molecular electrostatic interactions [25]. In a study on Na decorated C_{60} by Chandrakumar and Ghosh describe these ion-molecular forces driving H_2 physisortion. The physisorption is driven by the interaction of the induced dipole and quadrupolar interaction with the field generated from charge transfer between the cation and the C_{60} [23]. The result of this is a large number of H_2 molecules surrounding the metal ions, a characteristic that separates this process from the spillover mechanism which involves transition metals and H_2 dissociation. Ion-molecular electrostatic interactions are observed in the structures presented in Figures 3.14 to 3.18, and explains the large number of H_2 molecules we were able to adsorb to NaCl-coronene. The use of Alkali Halide coadsorbates, show the ability to adsorb multiple H_2 molecules with an increased average PSE due to ion-molecule interactions between the hydrogen molecules and both ions in the

Alkali Halide coadsorbates.

The NaF-coronene systems provide promising results in terms of possible hydrogen storage capacities. All four of the Alkali Halide coadsorbants studied have shown an increase in H_2 PSEs when used as a coadsorbant and all four also showed a significant increase in the quadrupole moment of the resulting optimized cluster. The LiCl case is interesting for the opposite reason as NaF; the initial quadrupole for LiCl is quite large at 17.11 Debye·Å before adsorption to coronene whereas for NaF it is 0.20 Debye·Å. After adsorption, the resulting clusters have quadrupole moments of 80.99 and 110.84 Debye·Å respectively and give very similar increases in H_2 PSEs, if a large enough basis set is used in the calculations. NaCl induces the largest quadrupole moment in the coadsorbed cluster yet gives the smallest predicted H_2 PSE. Despite this, NaCl as a coadsorbant produced the most number of H_2 molecules adsorbed symmetrically around a single cluster. This could be due in part to its larger mass compared to the other Alkali Halides studied. LiF had a moderate quadrupole before and after adsorption to coronene increasing from 7.66 to 84.74 Debye·Å giving a predicted H_2 PSE of -14.4 kJ/mol. The results of these calculations suggest all four of these systems would be worth further investigating experimentally.

3.9.2 Trends and Conclusions

The H_2-coronene PSE is calculated to be -6.1 kJ/mol, in good agreement with previous calculations [9]. LiF is shown to increase the magnitude of the H_2 PSE to -15.3 kJ/mol as a result of 2 adsorbed H_2 molecules, NaF is shown to increase the magnitude of the H_2 PSE to -17.8 kJ/mol as a result of 3 adsorbed H_2 molecules, LiCl is shown to increase the magnitude of the H_2 PSE to -11.7 kJ/mol as a result of 4 adsorbed H_2 molecules, and NaCl is shown to increase the magnitude of the H_2 PSE to -10.3 kJ/mol as a result of 6 adsorbed H_2 molecules. The magnitude of the increased H_2 PSE is due to a large induced quadrupole moment in the coadsorbed cluster which increases the ion-molecular electrostatic interactions between the coadsorbed Alkali Halides and the H_2 molecules.

Despite the multipole contribution, another reason for H_2's affinity for the substrate is due to the increased distortion in the coronene upon adsorption of NaF. The average C-C distance was the largest for NaF with a single adsorbed H_2. This increased average C-C

distance in NaF-coronene accounts at least partially for the observed increase in H_2 PSEs. Similar studies investigating Stone-Wales defects in graphene have shown increased H_2 physisorption energy by disrupting the π network of the carbon substrate. In these results it is concluded that a simple increase in average C-C distances has a similar effect[11]. From analysis of the equilibrium bond lengths of the Alkali Halides, it can be seen that in all cases, the bond lengths are increased after adsorption events. Neither the carbon substrate, nor the coadsorbates show significant distortion during adsorption processes. The energy barrier for H_2 dissociation to form a chemisorbed state ranges from -48 to -164 kJ/mol depending on the orientation [44]. The H_2 PSE's for our coadsorbed systems studied in this chapter are all below this range, showing stable physisorption based systems. These results further support the use of coadsorbed Alkali Halides for reversible H_2 storage in a solid state device.

In order to better our understanding of this system, and further provide evidence for use of LiF and NaF as novel coadsorbents in physisorption processes pertaining to hydrogen storage in a solid state graphene based system, a few things can still be done. Primarily, the SIESTA results need to be improved to match our GAMESS calculations and reference values. It is believed at this point that this could be due to the pseudopotentials presently being used in the SIESTA calculations. Although all the pseudopotentials used in this research have passed transferability tests as provided in the Atom program in the Siesta-3.2 distribution. If the cutoff radius used in the preparation of these standard pseudopotentials is chosen to be too small, many of the core states used to represent each atom are retained. These pseudopotentials are said to be hard as many of the core states have not been smoothed out. During which process, a curve is drawn from a region near the outermost node, r_c, to the origin removing all of the nodes in the core state wavefunctions that otherwise cause orthonormality issues in the plane wave atomic orbital basis set used. It is known that pseudopotentials that are too hard cause overestimates in binding energies, which could be the issue here. The discrepancies observed among similar groups of atoms further support this as the source of error. For instance, the trend observed among NaF and NaCl in SIESTA is backwards of that formed by GAMESS. The likely issue in this case, the Cl pseudopotential file being used to generate the basis set. Once the SIESTA calculations are better calibrated, we can then use this program to generate meaningful band structure diagrams and density of states plots from our converged structures. This, a better geometry

analysis of the corrugation in the carbon substrate, in addition to a more detailed basis set superposition error treatment, both before and after each adsorption event, would all help to further improve our understanding of the fundamental interactions taking place in these systems.

Appendix A

GAMESS Molecular Coordinates

Cartesian coordinates in Å of select molecular structures optimized at the 6-311G(2d,p)+ basis set level are found here.

coronene: $C_{24}H_{12}$: B3LYP-D

C	6	1.42349102	−0.02793563	0.00000000
C	6	0.68755993	−1.24648620	0.00000000
C	6	−0.73612292	−1.21861049	0.00000000
C	6	−1.42349087	0.02793545	0.00000000
C	6	−0.68755978	1.24648578	0.00000000
C	6	0.73612266	1.21861018	0.00000000
C	6	1.37159124	−2.48714858	0.00000000
C	6	0.61100941	−3.68696131	0.00000000
C	6	−0.75576317	−3.66010264	0.00000000
C	6	−1.46841370	−2.43146975	0.00000000
H	1	1.13669724	−4.63591147	0.00000000
H	1	−1.31882276	−4.58738707	0.00000000
C	6	2.79241437	−2.48427853	0.00000000
C	6	3.49898962	−1.31418055	0.00000000
C	6	2.84046166	−0.05568193	0.00000000
H	1	3.31383351	−3.43550949	0.00000000
H	1	4.58370598	−1.33288248	0.00000000
C	6	−2.88774101	−2.37297028	0.00000000
C	6	−3.54779158	−1.17601984	0.00000000
C	6	−2.84046139	0.05568219	0.00000000
H	1	−3.44698258	−3.30255978	0.00000000
H	1	−4.63244860	−1.15344894	0.00000000
C	6	−1.37159076	2.48714845	0.00000000
C	6	−2.79241377	2.48427803	0.00000000
C	6	−3.49898986	1.31418059	0.00000000
H	1	−4.58370627	1.33288297	0.00000000
H	1	−3.31383327	3.43550886	0.00000000
C	6	1.46841348	2.43146955	0.00000000
C	6	0.75576317	3.66010261	0.00000000
C	6	−0.61100940	3.68696135	0.00000000
H	1	1.31882164	4.58738777	0.00000000
H	1	−1.13669769	4.63591139	0.00000000
C	6	2.88774100	2.37297055	0.00000000
C	6	3.54779171	1.17602018	0.00000000
H	1	3.44698293	3.30256000	0.00000000
H	1	4.63244878	1.15344905	0.00000000

coronene: $C_{24}H_{12}$: MP2

C	6	1.420645153	−0.027908595	0.000000000
C	6	0.686151866	−1.244255759	0.000000000
C	6	−0.734473989	−1.216334570	0.000000000
C	6	−1.420645103	0.027908590	0.000000000
C	6	−0.686151857	1.244255774	0.000000000
C	6	0.734474002	1.216334560	0.000000000
C	6	1.373434237	−2.490562951	0.000000000
C	6	0.615648264	−3.690256227	0.000000000
C	6	−0.760165866	−3.663269540	0.000000000
C	6	−1.470165123	−2.434679220	0.000000000
H	1	1.142538321	−4.641655009	0.000000000
H	1	−1.324008193	−4.593231293	0.000000000
C	6	2.792417156	−2.489951448	0.000000000
C	6	3.503692761	−1.311964621	0.000000000
C	6	2.843624860	−0.055858856	0.000000000
H	1	3.315815424	−3.443261906	0.000000000
H	1	4.591074047	−1.331288584	0.000000000
C	6	−2.888037425	−2.378407009	0.000000000
C	6	−3.552476022	−1.173372191	0.000000000
C	6	−2.843624780	0.055858913	0.000000000
H	1	−3.448503422	−3.310402133	0.000000000
H	1	−4.639785396	−1.150011988	0.000000000
C	6	−1.373434174	2.490563011	0.000000000
C	6	−2.792417052	2.489951226	0.000000000
C	6	−3.503692965	1.311964575	0.000000000
H	1	−4.591074211	1.331288526	0.000000000
H	1	−3.315815413	3.443261682	0.000000000
C	6	1.470165137	2.434679188	0.000000000
C	6	0.760165974	3.663269565	0.000000000
C	6	−0.615648159	3.690256243	0.000000000
H	1	1.324008127	4.593231418	0.000000000
H	1	−1.142538409	4.641654921	0.000000000
C	6	2.888037460	2.378407186	0.000000000
C	6	3.552475940	1.173372311	0.000000000
H	1	3.448503506	3.310402258	0.000000000
H	1	4.639785327	1.150011950	0.000000000

coronene·LiF·$2H_2$: B3LYP-D

C	6	1.456275544	0.076506940	−0.329095542
C	6	0.760488120	−1.163776342	−0.232730884
C	6	−0.660459850	−1.177602206	−0.134606119
C	6	−1.387271888	0.049097169	−0.130975531
C	6	−0.693094859	1.290974412	−0.238442039
C	6	0.730002645	1.304593384	−0.336092419
C	6	1.485351968	−2.379744871	−0.196939774
C	6	0.767156440	−3.596975119	−0.066478800
C	6	−0.595891893	−3.609411226	0.032372712
C	6	−1.347958812	−2.406847238	0.005358751
H	1	1.323765392	−4.526721025	−0.028968413
H	1	−1.124183244	−4.548604528	0.151413379
C	6	2.902094636	−2.332548038	−0.276767935

C	6	3.569730025	−1.143809292	−0.376518746
C	6	2.872137886	0.092279361	−0.402223094
H	1	3.454812839	−3.264915065	−0.245699113
H	1	4.652797752	−1.130843421	−0.428946873
C	6	−2.760738428	−2.386273997	0.136962551
C	6	−3.458957749	−1.211670561	0.135194392
C	6	−2.798637638	0.037223983	0.003000706
H	1	−3.284249689	−3.327934086	0.258281900
H	1	−4.537364041	−1.219782626	0.248200740
C	6	−1.414718855	2.512355799	−0.225823971
C	6	−2.828763592	2.465632654	−0.101463256
C	6	−3.492589842	1.275136929	0.010392162
H	1	−4.571804344	1.264037247	0.116093503
H	1	−3.380286846	3.399132355	−0.087417560
C	6	1.422209911	2.539738526	−0.425092636
C	6	0.670191083	3.744348035	−0.423498196
C	6	−0.694109057	3.731360246	−0.327920297
H	1	1.201113072	4.687230536	−0.494900454
H	1	−1.248093573	4.663571489	−0.321953042
C	6	2.839829249	2.521119173	−0.509113750
C	6	3.535740356	1.344117870	−0.496027358
H	1	3.368806310	3.465097961	−0.579870376
H	1	4.618657534	1.353433467	−0.554074380
LI	3	0.041354294	0.310360453	2.080544404
H	1	−1.773401083	1.608450051	2.642989402
H	1	−1.563841996	1.079482656	3.133011408
F	9	0.064912230	−0.623155438	3.377999136
H	1	−1.391252426	−2.249593985	3.377985689
H	1	−1.933566551	−2.765799700	3.310953988

coronene·LiF·2H_2 : MP2

C	6	1.375815845	0.026843785	−0.266924889
C	6	0.659504922	−1.199148558	−0.175871350
C	6	−0.763354365	−1.190426120	−0.118038491
C	6	−1.468297628	0.046422314	−0.146316491
C	6	−0.749692556	1.272919770	−0.232270791
C	6	0.671674838	1.262318003	−0.295011987
C	6	1.365938587	−2.434101699	−0.112437387
C	6	0.625676153	−3.638967582	−0.004643868
C	6	−0.750195640	−3.631253254	0.047200585
C	6	−1.480261947	−2.416133014	−0.002990618
H	1	1.166429361	−4.581016017	0.044670917
H	1	−1.297542233	−4.566558117	0.135952969
C	6	2.783245896	−2.412627210	−0.152271076
C	6	3.475031669	−1.226182820	−0.239131451
C	6	2.798376775	0.018623653	−0.291989607
H	1	3.321800543	−3.355696369	−0.101872140
H	1	4.562045966	−1.230082096	−0.255012371
C	6	−2.896595590	−2.375084519	0.068232947
C	6	−3.578033958	−1.179434878	0.040907329
C	6	−2.890249634	0.057358906	−0.059447370
H	1	−3.442628743	−3.311503419	0.153296052
H	1	−4.663515369	−1.169545791	0.104128393
C	6	−1.453250377	2.511104209	−0.225291062
C	6	−2.869028118	2.491125251	−0.144927758
C	6	−3.564357959	1.305357426	−0.065861690
H	1	−4.649618030	1.313397264	0.001012419

H	1	−3.404945024	3.437185678	−0.138856169
C	6	1.390095050	2.489295853	−0.348139842
C	6	0.663086040	3.706546731	−0.350987961
C	6	−0.711757682	3.718068002	−0.291827327
H	1	1.214008929	4.643063473	−0.387716808
H	1	−1.249579542	4.662876682	−0.284381206
C	6	2.806444055	2.450385590	−0.385463180
C	6	3.487544267	1.255432727	−0.358360102
H	1	3.353862021	3.388880758	−0.420554056
H	1	4.574469225	1.247374260	−0.371994094
LI	3	0.112975205	0.171570591	2.011259905
H	1	−1.986071867	0.963353675	2.583372599
H	1	−1.464096664	1.143499727	3.084041839
F	9	1.087535038	0.747665008	3.155550235
H	1	0.114132778	−1.645275521	3.145864113
H	1	−0.303130835	−2.015600092	2.651631755

coronene·LiCl·4H_2 : B3LYP-D

C	6	1.466943038	0.015003378	−0.162900151
C	6	0.836116748	−1.256200274	−0.260986320
C	6	−0.582144874	−1.355676484	−0.184623339
C	6	−1.373751249	−0.179086960	−0.013679634
C	6	−0.738342779	1.098800759	0.070361335
C	6	0.683145020	1.190735125	0.001143889
C	6	1.619264717	−2.426272916	−0.405854479
C	6	0.961580427	−3.681740060	−0.485935692
C	6	−0.400115689	−3.778219065	−0.414709214
C	6	−1.211444856	−2.623149354	−0.259286131
H	1	1.564115907	−4.576975444	−0.592287847
H	1	−0.880331983	−4.748848307	−0.467341585
C	6	3.032306214	−2.300376928	−0.450055448
C	6	3.638415115	−1.079136195	−0.351284300
C	6	2.877966233	0.110596033	−0.203044165
H	1	3.631511406	−3.198094057	−0.553758590
H	1	4.719905080	−1.005469937	−0.373338129
C	6	−2.627244291	−2.688520752	−0.171789368
C	6	−3.387706257	−1.561581366	−0.015891337
C	6	−2.788186049	−0.276292930	0.068128652
H	1	−3.103937046	−3.660976259	−0.225725703
H	1	−4.467190125	−1.637021601	0.049912282
C	6	−1.523761565	2.269965493	0.234743879
C	6	−2.935980214	2.138401389	0.309138890
C	6	−3.544873692	0.915266820	0.232632955
H	1	−4.624493313	0.840168002	0.297934298
H	1	−3.533464569	3.034078896	0.437916456
C	6	1.309360272	2.455857192	0.112742527
C	6	0.497767805	3.609445806	0.273063494
C	6	−0.865299555	3.523385830	0.328621221
H	1	0.982656291	4.575035108	0.362705072
H	1	−1.464123769	4.417895516	0.457808034
C	6	2.726206018	2.520495843	0.067845441
C	6	3.480696501	1.390933147	−0.083287994
H	1	3.205520001	3.488125320	0.164292281
H	1	4.562611377	1.458301586	−0.102736608
LI	3	−0.589319361	0.012196796	2.309000460
H	1	−2.229881608	1.244838370	2.963436511
H	1	−1.717853842	1.234225798	3.510619358

CL	17	0.904480839	−0.189090563	3.749230277
H	1	−1.632466773	−1.653585566	3.054501953
H	1	−2.168700041	−1.611175856	2.533522327
H	1	0.727857460	2.668887867	3.561051026
H	1	0.504132588	3.356667850	3.371208852
H	1	0.647851407	−3.550239161	2.544928405
H	1	0.816904204	−2.919318114	2.909006066

coronene·LiCl·4H_2 : MP2

C	6	1.337459876	0.095477373	−0.076819639
C	6	0.692428920	−1.167457411	−0.163637521
C	6	−0.728438186	−1.243728963	−0.171546849
C	6	−1.505467709	−0.052448265	−0.069613835
C	6	−0.855963138	1.214660600	0.010319806
C	6	0.565664675	1.285830284	0.003919512
C	6	1.465670403	−2.360939184	−0.211312753
C	6	0.794734241	−3.607328356	−0.289208892
C	6	−0.579674738	−3.681549152	−0.308255158
C	6	−1.376691557	−2.511136623	−0.240671252
H	1	1.388511560	−4.517457663	−0.319073805
H	1	−1.073611722	−4.648703887	−0.359081339
C	6	2.878425329	−2.261307343	−0.164161612
C	6	3.502462319	−1.038563273	−0.074673680
C	6	2.756529629	0.165545930	−0.029109064
H	1	3.467496929	−3.174549720	−0.185399297
H	1	4.586893208	−0.983348873	−0.023357817
C	6	−2.794114593	−2.554795601	−0.215731421
C	6	−3.544989873	−1.405044526	−0.107894915
C	6	−2.928756804	−0.129258674	−0.029511051
H	1	−3.287377699	−3.522410218	−0.269365615
H	1	−4.630406813	−1.463728881	−0.079158151
C	6	−1.631377085	2.405453115	0.119785787
C	6	−3.045619296	2.297927040	0.153895518
C	6	−3.672986553	1.073523913	0.085105977
H	1	−4.758366983	1.015244227	0.116795363
H	1	−3.636286855	3.206787802	0.240790836
C	6	1.212025619	2.550718754	0.099932208
C	6	0.415449596	3.720781737	0.181049731
C	6	−0.959646033	3.652217150	0.194717060
H	1	0.911787972	4.685859733	0.249859885
H	1	−1.550947667	4.561473412	0.270644214
C	6	2.628458471	2.591949622	0.128190967
C	6	3.374746231	1.437071040	0.071364194
H	1	3.121947690	3.557142069	0.210433808
H	1	4.459774748	1.487726377	0.114860983
LI	3	−0.374155715	−0.221629312	2.130474138
H	1	−2.111815656	1.037151006	2.681714447
H	1	−1.701714415	0.992588416	3.302206900
CL	17	1.236033614	−0.573485832	3.428989696
H	1	−1.496689835	−1.868202494	3.006330117
H	1	−2.022056715	−1.771248873	2.486189710
H	1	0.748939886	2.392846778	3.362265625
H	1	0.402391015	2.991656711	3.093672923
H	1	2.082697813	−4.213283745	2.838528088
H	1	1.979495768	−3.485614275	2.935552006

coronene·NaF·3H_2 : B3LYP-D

C	6	3.079615398	0.774185124	0.985013154
C	6	3.140835213	−0.648628696	0.944400841
C	6	2.205501688	−1.381987066	0.155865757
C	6	1.209363815	−0.686787248	−0.594127105
C	6	1.155497476	0.738420986	−0.559493746
C	6	2.089513065	1.467980893	0.231679929
C	6	4.103812511	−1.339411968	1.720069246
C	6	4.121638165	−2.758898853	1.681949357
C	6	3.225078481	−3.461888259	0.926228598
C	6	2.239340133	−2.799766691	0.147875232
H	1	4.856039063	−3.285147314	2.281175724
H	1	3.246830226	−4.545863706	0.923964326
C	6	5.002550927	−0.586930583	2.521510897
C	6	4.944665954	0.777973309	2.559925016
C	6	3.983801521	1.497091748	1.800554308
H	1	5.736867758	−1.118462631	3.116171441
H	1	5.632305893	1.334530678	3.186685089
C	6	1.271979772	−3.500978814	−0.620604067
C	6	0.313492509	−2.835821807	−1.333322885
C	6	0.249407737	−1.416644481	−1.341153549
H	1	1.296913049	−4.584912655	−0.622973535
H	1	−0.422730028	−3.390997287	−1.903883943
C	6	0.151760264	1.425636250	−1.286749906
C	6	−0.789048251	0.668038102	−2.033942937
C	6	−0.745122476	−0.698443644	−2.057027850
H	1	−1.481559744	−1.256081029	−2.624875718
H	1	−1.562066547	1.195070942	−2.582163898
C	6	2.013382940	2.880923624	0.292554173
C	6	1.004446540	3.542617616	−0.456651406
C	6	0.109562242	2.843506582	−1.217617580
H	1	0.947968724	4.624424686	−0.408558145
H	1	−0.659415212	3.368376127	−1.773345824
C	6	2.939607396	3.579598404	1.111308784
C	6	3.886425255	2.913279318	1.838259657
H	1	2.876937490	4.660901405	1.161138213
H	1	4.575732414	3.464706098	2.467751216
NA	11	0.226712540	−0.586165784	2.069377799
H	1	−1.657123184	0.681858137	0.880986854
H	1	−1.803215012	0.608754198	1.611766034
F	9	−0.616159260	−0.533860495	3.845171749
H	1	1.147634635	−1.912538947	3.843316352
H	1	1.728726650	−2.264117086	3.516109585
H	1	0.862282967	0.961904606	3.962877095
H	1	1.427291695	1.434829846	3.791103184

coronene·NaF·3H_2 : MP2

C	6	3.062040154	0.745274004	1.026973799
C	6	3.112879189	−0.675957170	0.973169562
C	6	2.173642621	−1.392294640	0.179032298
C	6	1.184724213	−0.686938331	−0.563791045
C	6	1.134104187	0.735247301	−0.510225648
C	6	2.071563282	1.450865180	0.287280756

C	6	4.090345113	−1.382267196	1.729488817
C	6	4.107746512	−2.799355315	1.669217008
C	6	3.198695346	−3.492479353	0.902501452
C	6	2.210755307	−2.815181945	0.142351514
H	1	4.850642803	−3.337904367	2.252253237
H	1	3.222980947	−4.579080366	0.878355426
C	6	5.004110568	−0.643634170	2.524354475
C	6	4.954597297	0.730598252	2.576819922
C	6	3.988064684	1.460170975	1.837954471
H	1	5.746542354	−1.184558032	3.105675762
H	1	5.657740920	1.277546349	3.199862204
C	6	1.254449081	−3.503415603	−0.648430059
C	6	0.300266867	−2.821653818	−1.368862454
C	6	0.235802546	−1.404330442	−1.346662846
H	1	1.282340089	−4.589960505	−0.673544264
H	1	−0.426348220	−3.368390777	−1.964786063
C	6	0.134486536	1.440334504	−1.239386065
C	6	−0.792834775	0.699903703	−2.017509108
C	6	−0.743817434	−0.675174764	−2.069272278
H	1	−1.468718079	−1.223546118	−2.665889778
H	1	−1.556561990	1.238550961	−2.573115047
C	6	2.007133217	2.871450033	0.358386905
C	6	1.002530160	3.547645197	−0.381179033
C	6	0.097770112	2.856260611	−1.154265744
H	1	0.952800824	4.632162301	−0.323835487
H	1	−0.667252672	3.393517781	−1.709285605
C	6	2.945704232	3.557912069	1.171041476
C	6	3.903772860	2.875334059	1.885732841
H	1	2.892110144	4.642143790	1.229605764
H	1	4.607542969	3.419701192	2.510402251
NA	11	0.494922830	−0.112542889	2.260581245
H	1	−1.612168435	−0.106415222	0.749897344
H	1	−1.840048118	−0.138482699	1.456741503
F	9	−0.322620719	−0.212399282	4.085408327
H	1	1.037121450	−1.991483770	3.709708302
H	1	1.520055217	−2.388165843	3.298998886
H	1	0.902484730	1.667834498	3.869210141
H	1	1.354983473	2.133433487	3.497332354

coronene·NaCl·6H_2 : B3LYP-D

C	6	1.431036118	−0.193063954	−0.087538980
C	6	0.662603888	−1.388505241	−0.246620857
C	6	−0.764316634	−1.322764217	−0.284878125
C	6	−1.424964897	−0.062849577	−0.151803152
C	6	−0.657105574	1.132932397	−0.002800827
C	6	0.769873415	1.068433560	0.031705216
C	6	1.317876556	−2.643658755	−0.357822583
C	6	0.526864963	−3.816080686	−0.510413059
C	6	−0.841535110	−3.752234983	−0.543153040
C	6	−1.527281901	−2.511626457	−0.428388241
H	1	1.027478556	−4.776191468	−0.590201242
H	1	−1.424866717	−4.661807703	−0.650198495
C	6	2.738846082	−2.678933415	−0.301565547
C	6	3.474441500	−1.533295734	−0.146081888
C	6	2.848367137	−0.260586617	−0.037281324
H	1	3.238616632	−3.639834048	−0.376818376
H	1	4.558018408	−1.585350744	−0.100120374

C	6	−2.946263865	−2.415121674	−0.441795714
C	6	−3.579406736	−1.206377138	−0.318059468
C	6	−2.843076789	0.001536011	−0.171169975
H	1	−3.529790843	−3.324922433	−0.545928655
H	1	−4.664111837	−1.159151716	−0.322327991
C	6	−1.312999373	2.384364158	0.134758297
C	6	−2.734797504	2.416406262	0.113516832
C	6	−3.471161497	1.270516215	−0.035160464
H	1	−4.555861053	1.317741542	−0.039561411
H	1	−3.235809386	3.373260134	0.224508269
C	6	1.532181468	2.255123582	0.195290831
C	6	0.846307719	3.494186626	0.324206923
C	6	−0.522280514	3.556020903	0.295830292
H	1	1.428634335	4.401106991	0.455970852
H	1	−1.024660503	4.512316728	0.405669063
C	6	2.950936854	2.156390681	0.233632649
C	6	3.584194317	0.946239299	0.122833867
H	1	3.533113439	3.063684903	0.363984440
H	1	4.667992989	0.895171450	0.163935820
NA	11	−0.009599314	−0.504975864	2.617100014
H	1	−0.165444304	1.998748142	3.543045617
H	1	−0.114238010	2.362370904	2.894813879
CL	17	−0.229951248	−0.797171510	5.017817365
H	1	2.424071635	0.964429038	3.620660441
H	1	2.689597516	1.185665047	2.961825078
H	1	−2.598246281	0.721139495	3.427132752
H	1	−2.855529766	0.986033870	2.780622883
H	1	−0.052005075	−3.310710298	3.028538599
H	1	−0.009490735	−3.540323556	2.321161747
H	1	2.318439468	−1.846414737	3.343676640
H	1	2.644895459	−1.907660456	2.676784729
H	1	−2.808032342	−2.130290075	2.509222514
H	1	−2.510870936	−2.028969919	3.184624741

coronene·NaCl·6H_2 : MP2

C	6	1.428797511	−0.197239815	−0.069247682
C	6	0.675487828	−1.404980670	−0.195343032
C	6	−0.750824366	−1.351632788	−0.266431274
C	6	−1.426782986	−0.103055729	−0.103813177
C	6	−0.673112006	1.104591237	0.021442072
C	6	0.753028216	1.051149268	0.093575859
C	6	1.351075067	−2.650117841	−0.374821196
C	6	0.575469139	−3.833940547	−0.522037067
C	6	−0.803186127	−3.785297283	−0.568888006
C	6	−1.503591066	−2.557099984	−0.407084008
H	1	1.088616165	−4.787127811	−0.639942011
H	1	−1.374701181	−4.704835974	−0.685444790
C	6	2.772890909	−2.670440428	−0.322654012
C	6	3.500365624	−1.506230791	−0.178776969
C	6	2.854801239	−0.248982405	−0.012474947
H	1	3.289508924	−3.621762310	−0.440165403
H	1	4.588010402	−1.547190792	−0.144506223
C	6	−2.922548184	−2.473069217	−0.474381416
C	6	−3.574640940	−1.264124671	−0.338215660
C	6	−2.850986706	−0.047834891	−0.191178144
H	1	−3.498412606	−3.390024765	−0.589444845
H	1	−4.661892829	−1.226381288	−0.385224237

C	6	−1.348215061	2.354351376	0.168211007
C	6	−2.768986135	2.376912251	0.091808167
C	6	−3.496358917	1.212455248	−0.050364253
H	1	−4.583427808	1.254390422	−0.097428228
H	1	−3.285734592	3.329897963	0.194408237
C	6	1.506119157	2.259268268	0.204043975
C	6	0.806754004	3.490829551	0.340899408
C	6	−0.571774488	3.540476452	0.291841445
H	1	1.379064086	4.411278827	0.445793296
H	1	−1.084216196	4.495572637	0.396257388
C	6	2.925901638	2.178072964	0.251261438
C	6	3.578639414	0.969584459	0.114568651
H	1	3.501639110	3.096465435	0.355409408
H	1	4.666348170	0.933411195	0.150868456
NA	11	−0.102594717	−0.482590437	2.543046793
H	1	0.006125791	2.194763218	3.701788793
H	1	0.030817820	2.561983189	3.059696833
CL	17	−0.142799518	−0.724748614	4.956931838
H	1	2.440474811	0.801771345	3.683138427
H	1	2.731636759	1.020871568	3.039493007
H	1	−2.464506025	0.892775588	3.476425462
H	1	−2.682965483	1.116986415	2.805827766
H	1	−0.195499343	−3.278833061	3.043389040
H	1	−0.183295286	−3.470541545	2.328636621
H	1	2.265126065	−1.965241027	3.274400687
H	1	2.523014435	−2.038231485	2.584515418
H	1	−2.863562043	−1.959903574	2.523216536
H	1	−2.624407965	−1.891454166	3.220151109

Appendix B

SIESTA Fractional Coordinates

Unit cell vectors and fractional coordinates in Å of select LYP/TZ2P optimized stuctures from the text are listed.

Unit Cell Vectors: graphene

9.932762	-0.000102	0.000049
4.966293	8.602099	0.000011
0.000114	-0.000035	23.01645

Fractional Coordinates: graphene

C	1	0.33331350	0.33332329	0.000000000
C	1	0.66665070	0.66666394	0.000000000
C	1	0.16665235	0.16666532	0.000000000
C	1	0.83331487	0.83332663	0.000000000
C	1	0.16665166	0.66666599	0.000000000
C	1	0.08331397	0.83332682	0.000000000
C	1	0.08331267	0.58332699	0.000000000
C	1	0.33331306	0.58332336	0.000000000
C	1	0.58331169	0.33332416	0.000000000
C	1	0.33331280	0.83332655	0.000000000
C	1	0.83331247	0.33332528	0.000000000
C	1	0.66665369	0.16666208	0.000000000
C	1	0.58331701	0.08332340	0.000000000
C	1	0.83331485	0.08332607	0.000000000
C	1	0.08331434	0.08332636	0.000000000
C	1	0.08331117	0.33332762	0.000000000
C	1	0.33331551	0.08332419	0.000000000
C	1	0.41665403	0.16666202	0.000000000
C	1	0.16665220	0.41666484	0.000000000
C	1	0.91665253	0.91666499	0.000000000
C	1	0.58331121	0.58332454	0.000000000
C	1	0.41665043	0.41666276	0.000000000
C	1	0.66665070	0.41666323	0.000000000
C	1	0.41664880	0.66666466	0.000000000
C	1	0.91665284	0.16666519	0.000000000
C	1	0.91664935	0.41666643	0.000000000
C	1	0.83331205	0.58332634	0.000000000
C	1	0.91665159	0.66666561	0.000000000
C	1	0.16665266	0.91666498	0.000000000

C	1	0.41665259	0.91666269	0.000000000
C	1	0.58331377	0.83332486	0.000000000
C	1	0.66665328	0.91666232	0.000000000

Unit Cell Vectors: $LiF{\cdot}5H_2{\cdot}$graphene

9.863768	-0.003015	0.244522
4.928462	8.538793	0.442684
0.555058	0.854946	27.481711

Fractional Coordinates:$LiF{\cdot}5H_2{\cdot}$graphene

C	6	0.33360804	0.33303088	0.00834813
C	6	0.66646886	0.66674566	0.00794689
C	6	0.16684817	0.16613784	0.00773920
C	6	0.83331560	0.83333898	0.00802827
C	6	0.16682885	0.66648301	0.00832534
C	6	0.08343669	0.83317634	0.00772656
C	6	0.08343630	0.58320466	0.00844736
C	6	0.33346674	0.58308707	0.00819438
C	6	0.58343698	0.33320559	0.00729729
C	6	0.33340471	0.83309614	0.00800578
C	6	0.83312028	0.33312681	0.00691099
C	6	0.66680635	0.16653739	0.00727571
C	6	0.58348514	0.08314230	0.00794429
C	6	0.83338110	0.08326275	0.00687193
C	6	0.08331981	0.08307776	0.00703557
C	6	0.08358796	0.33290605	0.00825531
C	6	0.33355844	0.08299504	0.00809848
C	6	0.41684520	0.16636825	0.00828745
C	6	0.16699083	0.41650963	0.00848194
C	6	0.91675472	0.91660534	0.00745571
C	6	0.58330802	0.58320104	0.00765336
C	6	0.41682506	0.41650728	0.00798797
C	6	0.66644410	0.41671898	0.00709160
C	6	0.41670342	0.66648000	0.00806150
C	6	0.91666394	0.16645574	0.00660089
C	6	0.91637880	0.41664462	0.00788714
C	6	0.83305605	0.58365464	0.00808409
C	6	0.91661037	0.66672601	0.00833564
C	6	0.16680272	0.91638239	0.00754661
C	6	0.41672628	0.91645444	0.00815427
C	6	0.58331665	0.83325400	0.00828989
C	6	0.66670658	0.91653402	0.00812167
Li	3	0.97103769	0.30052976	0.09529041
F	9	−0.08753244	0.18779109	0.12494454
H	1	0.94149232	0.96569964	0.12255590
H	1	0.95324133	0.88514988	0.11866595
H	1	0.67420894	0.24935608	0.12162290
H	1	0.58769056	0.28054369	0.11752142
H	1	0.16582118	0.06507221	0.12629243
H	1	0.06590424	0.41137472	0.13926977
H	1	0.24611246	0.05580158	0.12045781
H	1	0.08800441	0.43771387	0.11507662
H	1	0.73751066	0.47176409	0.12614123
H	1	0.72715381	0.55060907	0.11669451

Unit Cell Vectors: $LiCl{\cdot}5H_2{\cdot}$graphene

9.86731	-0.000702	-0.037814
4.934256	8.544877	0.082929
-0.119298	1.466742	23.094227

Fractional Coordinates:$LiCl{\cdot}5H_2{\cdot}$graphene

C	6	0.33346310	0.33333621	0.01510996
C	6	0.66616977	0.66707871	0.01501418
C	6	0.16658175	0.16651777	0.01443098
C	6	0.83307258	0.83385101	0.01508240
C	6	0.16678708	0.66692390	0.01506489
C	6	0.08321773	0.83358739	0.01473466
C	6	0.08335819	0.58366292	0.01509061
C	6	0.33341335	0.58337408	0.01510085
C	6	0.58325823	0.33338229	0.01455951
C	6	0.33310386	0.83354773	0.01484512
C	6	0.83286571	0.33335147	0.01411362
C	6	0.66660796	0.16680396	0.01461054
C	6	0.58317423	0.08354949	0.01505049
C	6	0.83314401	0.08361566	0.01429245
C	6	0.08300753	0.08354622	0.01413107
C	6	0.08352950	0.33320602	0.01479777
C	6	0.33315371	0.08350377	0.01475814
C	6	0.41655706	0.16676898	0.01504943
C	6	0.16684011	0.41682795	0.01506509
C	6	0.91656083	0.91701714	0.01464783
C	6	0.58312279	0.58348023	0.01483357
C	6	0.41675975	0.41672955	0.01497537
C	6	0.66637550	0.41685231	0.01439748
C	6	0.41655149	0.66683773	0.01504543
C	6	0.91638493	0.16682404	0.01392068
C	6	0.91632228	0.41679951	0.01471735
C	6	0.83298956	0.58389902	0.01508898
C	6	0.91651942	0.66719254	0.01515066
C	6	0.16643388	0.91696884	0.01455773
C	6	0.41640315	0.91689229	0.01485390
C	6	0.58304236	0.83371107	0.01514435
C	6	0.66642707	0.91696674	0.01520164
Li	3	0.95655783	0.38638289	0.07275692
Cl	17	−0.02933501	0.17972995	0.09167855
H	1	0.95357504	0.93083791	0.08954155
H	1	0.94391731	0.85981708	0.08822005
H	1	0.64502998	0.29382723	0.08831283
H	1	0.55754542	0.33554678	0.08548001
H	1	0.28121996	−0.02803028	0.08950235
H	1	0.07181843	0.49375622	0.09698144
H	1	0.36656170	−0.08001388	0.08595523
H	1	0.07783849	0.52380731	0.0809068
H	1	0.73202202	0.53607776	0.09286766
H	1	0.73211830	0.60745342	0.08571328

Unit Cell Vectors: $NaF{\cdot}5H_2{\cdot}$graphene

9.868801	-0.000718	-0.039541
4.934482	8.54479	-0.161377
-0.118635	-0.384543	28.137868

Fractional Coordinates:NaF·5H_2·graphene

C	6	0.33343615	0.33353926	0.01031604
C	6	0.66621378	0.66720447	0.00974304
C	6	0.16656329	0.16657687	0.01009587
C	6	0.83310962	0.83385912	0.00997847
C	6	0.16658628	0.66719886	0.01023125
C	6	0.08310857	0.83371418	0.01003768
C	6	0.08320247	0.58387131	0.01015725
C	6	0.33317337	0.58367551	0.01020470
C	6	0.58324972	0.33346444	0.00983174
C	6	0.33299703	0.83370783	0.01012077
C	6	0.83286645	0.33336867	0.00953519
C	6	0.66668912	0.16687676	0.00993798
C	6	0.58328739	0.08366258	0.01026959
C	6	0.83311810	0.08352564	0.00977115
C	6	0.08291659	0.08346188	0.00981329
C	6	0.08329425	0.33356265	0.01020227
C	6	0.33331489	0.08352021	0.01026829
C	6	0.41667642	0.16688841	0.01035444
C	6	0.16677453	0.41711320	0.01027009
C	6	0.91651425	0.91708915	0.00985594
C	6	0.58297741	0.58366118	0.00971778
C	6	0.41669567	0.41697271	0.01014622
C	6	0.66627239	0.41697633	0.00957270
C	6	0.41636854	0.66707428	0.01006361
C	6	0.91637560	0.16673812	0.00977248
C	6	0.91611299	0.41706714	0.00986330
C	6	0.83285089	0.58406142	0.00981568
C	6	0.91644243	0.66728947	0.01000884
C	6	0.16641755	0.91695192	0.01002380
C	6	0.41643005	0.91697548	0.01021334
C	6	0.58302373	0.83386218	0.01011841
C	6	0.66650944	0.91708035	0.01019695
Na	11	0.97840907	0.33428216	0.10517091
F	9	−0.08759010	0.17507592	0.11592605
H	1	0.90974655	0.97644514	0.11896943
H	1	0.90739372	0.90015886	0.11842846
H	1	0.67455091	0.30150142	0.12058028
H	1	0.58581909	0.35512736	0.11971352
H	1	0.14055377	0.06671106	0.12512149
H	1	0.12582025	0.45857300	0.13703076
H	1	0.22576673	0.04909379	0.12640912
H	1	0.14624208	0.46101808	0.11135513
H	1	0.71174704	0.56333374	0.12471875
H	1	0.73469654	0.61910894	0.11456578

Unit Cell Vectors: NaCl·5H_2·graphene

9.862556	0.002158	-0.251072
4.93867	8.539961	0.227861
-0.092344	0.589039	21.955526

Fractional Coordinates:NaCl·5H_2·graphene

C	6	0.33412141	0.33272434	0.01690822
C	6	0.66680108	0.66644587	0.01633273
C	6	0.16713844	0.16587553	0.01627776

C	6	0.83366225	0.83319371	0.01663425
C	6	0.16730905	0.66633382	0.01690907
C	6	0.08377744	0.83299938	0.01652705
C	6	0.08380671	0.58306791	0.01682538
C	6	0.33395136	0.58277512	0.01692218
C	6	0.58380393	0.33287604	0.01636500
C	6	0.33373717	0.83282243	0.01672533
C	6	0.83305050	0.33314262	0.01542757
C	6	0.66719477	0.16628348	0.01646067
C	6	0.58392083	0.08281751	0.01686880
C	6	0.83356090	0.08312465	0.01593893
C	6	0.08321663	0.08315896	0.01579927
C	6	0.08383515	0.33272046	0.01648608
C	6	0.33398891	0.08262334	0.01672538
C	6	0.41730501	0.16605839	0.01693161
C	6	0.16732449	0.41625211	0.01685925
C	6	0.91695244	0.91653465	0.01631639
C	6	0.58356935	0.58299987	0.01631057
C	6	0.41733001	0.41614919	0.01677311
C	6	0.66666163	0.41654414	0.01593967
C	6	0.41710314	0.66624029	0.01678230
C	6	0.91656818	0.16658099	0.01541548
C	6	0.91652622	0.41646525	0.01597592
C	6	0.83344030	0.58327511	0.01632403
C	6	0.91691938	0.66658976	0.01665290
C	6	0.16693439	0.91637395	0.01638203
C	6	0.41718922	0.91602603	0.01678236
C	6	0.58378020	0.83292339	0.01672943
C	6	0.66706886	0.91631620	0.01680795
Na	11	1.00397946	0.34528729	0.08274389
Cl	17	−0.13513999	0.20644638	0.09428075
H	1	0.93079780	0.92747180	0.09341957
H	1	0.94609647	0.84427124	0.09246009
H	1	0.58024712	0.28434284	0.09475949
H	1	0.49362215	0.31003830	0.09395054
H	1	0.20282766	0.06528201	0.09416516
H	1	0.12161056	0.48667016	0.10618242
H	1	0.27612345	0.06928839	0.09105279
H	1	0.13234508	0.50278110	0.08893488
H	1	0.72687964	0.53305194	0.09397659
H	1	0.72435331	0.61016684	0.09023445

Bibliography

[1] A.D.Becke. In: *Phys.Rev.A* 38 (1988), p. 3098.

[2] Abd.Khalim Khafidz NZ et al. In: *International Journal of Hydrogen Energy* 10 (2016), pp. 1–21.

[3] B. Tang et al. In: *Applied Spectroscopy Reviews* 45 (2010), pp. 369–407.

[4] Bofanti et al. In: *J.Phys.Chem.C* 111 (2007), pp. 5825–5829.

[5] Cheng et al. In: *Energy Environ.Sci.* 1 (2008), pp. 338–354.

[6] Eduardo Anglada et al. In: *Physical Review B* 64 (2001), p. 235111.

[7] Eduardo Anglada et al. In: *Physical Review B* 66 (2002), p. 205101.

[8] England et al. In: *Adv.QuantumChem.* 11 (1978), p. 93.

[9] Heine et al. In: *Phys.Chem.Chem.Phys.* 6 (2004), pp. 980–984.

[10] J.G. Yu et al. In: *Science of the Total Environment* 502 (2015), pp. 70–79.

[11] Kim et al. In: *International Journal of Hydrogen Energy* 39 (2014), pp. 13189–13194.

[12] Ling Ma et al. In: *PhysicaE* 66 (2015), pp. 40–47.

[13] M Darvish Ganji et al. In: *Phys.Chem.Chem.Phys* 17 (2015), pp. 2504–2511.

[14] Michael W. Schmidt et al. In: *J. Comput. Chem* 14 (1993), p. 1347.

[15] Modisette et al. In: *J.Chem.Phys.* 101 (1994), pp. 8903–8907.

[16] Neto et al. In: *Reviews of Modern Physics* 81 (2009), pp. 109–162.

[17] Petr Lazar et al. In: *J.Am.Chem.Soc.* 135 (2013), pp. 6372–6377.

[18] W.A.Sokalski et al. In: *J.Phys.Chem.B* 110 (2006), pp. 9720–9727.

[19] Xiao Ming Liu et al. In: *Nano Lett.* 13 (2013), pp. 137–141.

[20] Bhatia and Myers. In: *Langmuir* 22 (2006), pp. 1688–1700.

[21] B.M. Bode and M.S. Gordon. In: *J.Mol.Graphics and Modeling* 16 (1999), pp. 133–138.

[22] R. G. Parr C. Lee W. Yang. In: *Phys.Rev.B* 37 (1988), p. 785.

[23] K.R.S. Chandrakumar and Swapan K. Ghosh. In: *Nano Lett.* 8 (2008), pp. 14–21.

[24] Huang Chen and Qu. In: *Phys.Chem.Chem.Phys.* 17 (2015), p. 32077.

[25] C. Malardier-Jugroot D.J. Durbin. In: *International Journal of Hydrogen* 38 (2013), pp. 14595–14617.

[26] James B. Foresman and Frisch. *Exploring Chemistry with Electronic Structure Methods*. 2015.

[27] Stefan Grimme. In: *J Comput Chem* 27 (2006), pp. 1787–1799.

[28] Puru Jena. In: *J.Phys.Chem.Lett.* 2 (2011), pp. 206–211.

[29] S. Kielich and R. Zawodny. In: *Chemical Physics Letters* 12 (1971), pp. 20–25.

[30] Charles Kittel. *Introduction to Solid State Physics*. 2005.

[31] V. Sidisr L. Jeloaica. In: *Chemical Physics Letters* 300 (1999), pp. 157–162.

[32] Ira N. Levine. *Quantum Chemistry*. 2000.

[33] R. Lochan and M. Head-Gordon. In: *Phys.Chem.Chem.Phys* 8 (2006), pp. 1357–1370.

[34] Audiffred Miró and Heine. In: *Chem.Soc.Rev.* 43 (2014), pp. 6537–6554.

[35] Jonas Moellmann and Stefan Grimme. In: *Phys.Chem.Chem.Phys.* 12 (2010), pp. 5800–8504.

[36] N. Prasad Adhikari N.Pantha K.Belbase. In: *Appl Nanoscience* 5 (2015), pp. 393–402.

[37] Burke Perdew and Ernzerhof. In: *Phys.Rev.Lett.* 77 (1996), p. 3865.

[38] J. A. Pople. In: *The Journal of Chemical Physics* 43 (1965), p. 701495.

[39] David S. Sholl and Janice A. Steckel. *Density Functional Theory: A Practical Introduction*. 2009.

[40] Attila Szabo and Neil S. Ostlund. *Modern Quantum Chemistry*. 1996.

[41] Tozzini and Pellegrini. In: *Phys.Chem.Chem.Phys.* 15 (2013), p. 80.

[42] Weber Tran and Wesolowski. In: *J.Phys.Chem.B* 106 (2002), pp. 8689–8696.

[43] Vereecken and Francisco. In: *Chem.Soc.Rev.* 41 (2012), pp. 6259–6293.

[44] Yuan Ping Feng Yunhao Lu. In: *Nanoscale* 3 (2011), p. 2444.